

*Large-Deflection Bimorph Magnetic Actuators with Rotationally
Corrected Motion and Electrostatic Hold*

By

Kwan-yu Lai

A Thesis

Submitted to the Faculty of Graduate Studies

in Partial Fulfillment of the Requirements for the Degree of

Master of Science

Department of Electrical and Computer Engineering

University of Manitoba

Winnipeg, Manitoba, Canada



UNIVERSITY
OF MANITOBA

Copyright© 2006 Kwan-yu Lai

THE UNIVERSITY OF MANITOBA
FACULTY OF GRADUATE STUDIES

COPYRIGHT PERMISSION

**Large-Deflection Bimorph Magnetic Actuators with Rotationally Corrected Motion and
Electrostatic Hold**

BY

Kwan-yu Lai

**A Thesis/Practicum submitted to the Faculty of Graduate Studies of The University of
Manitoba in partial fulfillment of the requirement of the degree**

OF

MASTER OF SCIENCE

Kwan-yu Lai © 2006

Permission has been granted to the Library of the University of Manitoba to lend or sell copies of this thesis/practicum, to the National Library of Canada to microfilm this thesis and to lend or sell copies of the film, and to University Microfilms Inc. to publish an abstract of this thesis/practicum.

This reproduction or copy of this thesis has been made available by authority of the copyright owner solely for the purpose of private study and research, and may only be reproduced and copied as permitted by copyright laws or with express written authorization from the copyright owner.

Abstract

Micromachined actuators have advantages due to their reduced size and improved performance for many applications, such as RF switches and micro-mirrors. Surface microelectromechanical actuators with large deflection have been designed and fabricated using a two mask process. Upon release, these bi-metallic structures utilize stress in the thin films to curl out-of-plane. This provided a large initial deflection of the surface micromachined devices without actuation. Using Lorentz force for actuation, a vertical displacement of $107\mu\text{m}$ was achieved with 20mA . The devices exhibited very linear current-deflection characteristics over the entire range and excellent metal-to-metal contact when implemented as switches. Furthermore, the actuator can also function as a tri-state switch. Finite element modeling (FEM) of the devices agrees with actual measurements. Modeling of an advanced design of the basic structure is also presented. The advanced actuator design allows these structures to have a large overall range of motion with very fine tilt control. Measured results on the advanced device confirm its intended design. Both the basic and advanced devices can also be held in a closed position using electrostatic forces, thus reducing power consumption when the actuators are maintained in the closed position. All experiments and measurements were taken using an external magnetic field of 0.25T measured at the surface.

Acknowledgements

“Thank you” is a very generic phrase when it comes to acknowledgements. It can be used to express appreciation to a great mentor who provides guidance and support through the course of a master’s degree [A1]. Ironically, sometimes the lack of guidance can also help one realize his/her lack of direction in research and life. “Thank you” can also be used when a group of peers unite in the absence of their designated guides [A2]. In this case the phrase is used to show appreciation to the inspiring discussions that just keep on going and going and going. “Thank you” can further be used in a situation when individuals from the University of Manitoba’s SPM/MEMS research group contributes to the completion of a master’s research work [A3]. For everyone that has fallen into all of the above categories, I sincerely thank you.

There are also times when “thank you” is insufficient. In my case, it barely captures the gratefulness for the spiritual support from a lifelong loving companion, Jasmine Tu 塗欽夏. She has kept me inspired and determined in the pursuit of this degree. Thank you Jasmine. Last but definitely matters to me the most, I would not have had the chance to study in Canada without the support and guidance of my dear parents, Soon-Chan Lai 賴森泉 and Chu-Lien Hung 洪珠聯. They have also taught me everything I needed to know in becoming the person I am today. Thank you. And I love you.

References*

- [A1] Dr. Cyrus Shafai, personal communications 2003 ~ 2006.
- [A2] In alphabetical order: Kar-Mun Cheng, Jeremy Johnson, Alfred Lip, Joe Yip, *The Weekly LLS/DLS Conferences*, 2003 ~ 2006, room E-III 360.
- [A3] Behraad Bahreyni, Dr. Greg Bridges, Dr. Douglas Buchanan, Jane Cao, Dwayne Chrusch, Dr. Douglas Thomson.

* For the acknowledgement section only.

Table of Contents

| | |
|---|---------------|
| CHAPTER 1: INTRODUCTION..... | - 1 - |
| 1.1 Motivation: Large-Deflection MEMS Actuators | - 1 - |
| 1.2 Thesis Objectives | - 3 - |
| 1.3 Organization of Thesis | - 3 - |
| CHAPTER 2: MEMS AND MICROMACHINING TECHNIQUES..... | - 5 - |
| 2.1 Overview..... | - 5 - |
| 2.2 Thermal Evaporation..... | - 6 - |
| 2.3 Sputter Deposition | - 8 - |
| 2.4 Stress in Thin Films | - 10 - |
| 2.5 Photo-lithography and Photoresist Patterning..... | - 15 - |
| 2.6 Sacrificial Materials | - 17 - |
| 2.6.1 Photoresist Sacrificial..... | - 17 - |
| 2.6.2 Silicon Sacrificial..... | - 22 - |
| 2.7 Isotropic Wet Etching..... | - 23 - |
| 2.8 Isotropic XeF ₂ Silicon Etching..... | - 24 - |
| 2.9 Plasma/Reactive Ion Etching..... | - 25 - |
| 2.10 Chapter Summary | - 26 - |
| CHAPTER 3: LITERATURE REVIEW..... | - 27 - |

| | |
|--|--------|
| 3.1 Overview..... | - 27 - |
| 3.2 Electrostatic Actuation Theory..... | - 27 - |
| 3.3 Cascaded Electrostatic Cantilevers..... | - 29 - |
| 3.3.1 Design and Actuation Principle..... | - 29 - |
| 3.3.2 Fabrication of Cascaded Electrostatic Actuators..... | - 32 - |
| 3.3.3 Test Results..... | - 33 - |
| 3.4 Curved electrostatic cantilever with stopper..... | - 35 - |
| 3.5 Electromagnetic Actuation Theory..... | - 37 - |
| 3.6 Integrated Coil Lorentz Cantilevers..... | - 38 - |
| 3.7 Horseshoe Lorentz Force Actuators..... | - 40 - |
| 3.8 Chapter Summary..... | - 42 - |

CHAPTER 4: LARGE-DEFLECTION LOW VOLTAGE ELECTROMAGNETIC ACTUATOR..... - 43 -

| | |
|--|--------|
| 4.1 Overview..... | - 43 - |
| 4.2 Introduction and Basic Design..... | - 43 - |
| 4.3 Fabrication..... | - 45 - |
| 4.5 Finite Element Modeling..... | - 48 - |
| 4.5.1 Stress Analysis..... | - 48 - |
| 4.5.2 Actuation Analysis..... | - 51 - |
| 4.7 Joule Heating Effects..... | - 55 - |
| 4.8 Chapter Summary..... | - 56 - |

CHAPTER 5: ROTATIONALLY CORRECTED ELECTROMAGNETIC ACTUATOR..... - 58 -

| | | |
|---|---|---------------|
| 5.1 | Overview..... | - 58 - |
| 5.2 | Introduction and Design..... | - 58 - |
| 5.3 | Finite Element Modeling: Rotationally Corrected Devices | - 60 - |
| 5.3.1 | Stress Analysis..... | - 60 - |
| 5.3.2 | Actuation Analysis | - 63 - |
| 5.3.3 | Advanced Actuation Analysis | - 66 - |
| 5.4 | Chapter Summary | - 69 - |
| CHAPTER 6: TESTING AND VERIFICATION..... | | - 71 - |
| 6.1 | Overview..... | - 71 - |
| 6.2 | Experiment Setup | - 71 - |
| 6.3 | Basic U-Shaped Actuator Results | - 72 - |
| 6.3.1 | Static Analysis..... | - 72 - |
| 6.3.2 | Actuation Analysis | - 73 - |
| 6.4 | Rotationally Corrected Devices | - 76 - |
| 6.4.1 | Static Analysis | - 76 - |
| 6.4.2 | Actuation Analysis..... | - 77 - |
| 6.5 | Chapter Summary | - 79 - |
| CHAPTER 7: DISCUSSION OF RESULTS..... | | - 80 - |
| 7.1 | Overview..... | - 80 - |
| 7.2 | Large-Deflection Switch Performance..... | - 80 - |
| 7.3 | Design Parameters Affecting Actuator Performance..... | - 81 - |
| 7.4 | Potential Applications..... | - 82 - |
| 7.5 | Chapter Summary | - 83 - |

CHAPTER 8: FUTURE WORK, SUMMARY AND CONCLUSIONS - 85 -

8.1 Future Work..... - 85 -

8.2 Alternative Materials..... - 86 -

8.3 Summary - 87 -

8.4 Conclusions - 88 -

REFERENCES - 89 -

APPENDICES..... - 91 -

List of Figures

| | |
|---|--------|
| FIG. 1.1: EXAMPLE OF A MICROMACHINED RF SWITCH DEVICE | - 1 - |
| FIG. 2.1: A THERMAL EVAPORATOR SCHEMATIC | - 6 - |
| FIG. 2.2: (A) ILLUSTRATION OF A BASIC SPUTTER SYSTEM. (B) PHOTOGRAPH OF SILICON SPUTTERING IN PROGRESS | - 9 - |
| FIG. 2.3: EFFECTS OF FILM STRESSES ON A WAFER (EXAGGERATED) | - 11 - |
| FIG. 2.4: (A) TOP VIEW OF CURVED CANTILEVERS BEFORE RELEASE. (B) CROSS SECTION VIEW OF CURVED CANTILEVERS BEFORE RELEASE. (C) SIDE VIEW AFTER RELEASE SHOWING RADIUS OF CURVATURE R (NOT TO SCALE) | - 12 - |
| FIG. 2.5: CALCULATED RADIUS OF CURVATURE R VERSUS Ct/Al THICKNESS RATIO n FOR $\sigma_{Cr} = -450\text{MPa}$ AND $\sigma_{Al} = 0\text{Pa}$ (SEE APPENDIX C FOR FULL MATLAB CODE USED FOR THIS CALCULATION)..... | - 14 - |
| FIG. 2.7: OVERVIEW OF A TYPICAL LITHOGRAPHY PROCESS. | - 16 - |
| FIG. 2.8: BUBBLING OF THE STRUCTURAL LAYER CAUSED BY OUT-GASSING OF SOLVENTS IN THE PHOTORESIST SACRIFICIAL | - 19 - |
| FIG. 3.1: TYPICAL STRUCTURE OF AN IN-LINE MEMS ELECTROSTATIC SWITCH | - 28 - |
| FIG. 3.2: (A) TOP VIEW OF THE CASCADED BI-LAYER CANTILEVERS. (B) ISOMETRIC VIEW OF A CASCADED ELECTROSTATIC ACTUATOR AT REST | - 30 - |
| FIG. 3.3: (A) INITIAL POSITION OF CASCADED STRUCTURE. (B) AFTER THE 1 ST BEAM PULLS DOWN. (C) AFTER THE 2 ND BEAM PULLS DOWN. (D) END POSITION AFTER ACTUATION | - 31 - |
| FIG. 3.4: FABRICATION SEQUENCE OF THE CASCADED ELECTROSTATIC CURLED CANTILEVERS (NOT TO SCALE)..... | - 33 - |
| FIG. 3.5: PICTURE OF THREE CURLED CANTILEVER SWITCHES..... | - 34 - |
| FIG. 3.6: (A) SINGLE LARGE-DEFLECTION CURVED CANTILEVER USED AS OPTICAL SWITCH BY CHEN et al. (B) ILLUSTRATION OF ACTUATION PRINCIPLE SHOWING THE POLYSILICON STOPPER PLATE CONCEPT ... | - 36 - |
| FIG. 3.7: ILLUSTRATION OF LORENTZ FORCE ON A PIECE OF SUSPENDED WIRE..... | - 38 - |

| | |
|---|--------|
| FIG. 3.8: ILLUSTRATION OF INTEGRATED COIL CANTILEVER ACTUATOR STUDIED BY CHO. et al. | - 39 - |
| FIG. 3.9: ILLUSTRATION OF SHIMOYAMA'S LORENTZ ACTUATOR | - 40 - |
| FIG. 4.1: A) ILLUSTRATION OF LORENTZ FORCE ACTUATORS, SHOWING ORIENTATION OF FORCE, MAGNETIC FIELD, AND CURRENT B) TOP VIEW SHOWING DEVICE DESIGN DIMENSIONS C) SIDE VIEW SHOWING RELEASED CURVED CANTILEVER AND MEASUREMENTS. | - 44 - |
| FIG. 4.2: FABRICATION SEQUENCE OF THE LORENTZ SWITCHES | - 47 - |
| FIG. 4.3: (A) BASIC MODEL SHOWING DEVICE AT REST OUT-OF-PLANE DUE TO RESIDUE STRESS. (B) MESH STRUCTURE USED FOR FEM ANALYSIS | - 48 - |
| FIG. 4.4: (A) TIP HEIGHT VERSUS STRESS IN SIMULATED RESULTS. (B) PROFILE OF ONE OF THE ARMS ALONG ITS LENGTH FOR DIFFERENT STRESS LEVELS, SHOWING CURVATURE WHERE C_r IS PRESENT (136 μ m LENGTH) AND STRAIGHT SECTIONS EVERYWHERE ELSE (164 μ m) | - 50 - |
| FIG. 4.5: (A) CONNECTOR TIP HEIGHT VERSUS ACTUATION FORCE PER AREA f_L . (B) ARM PROFILES FOR INCREASING ACTUATION FORCES (IN N/m ²), SHOWING THE INCREASING DOMED PROFILE | - 52 - |
| FIG. 4.6: (A) CHANGE IN DOME PROFILE WHEN TIP IS TOUCHED DOWN FOR DIFFERENT C_r LENGTHS. (B) EXAGGERATED (5X) SNAPSHOT OF THE SIMULATED DEVICE AT TOUCHDOWN POSITION, SHOWING BOTH THE CURVATURES OF THE ARM AND CROSSBAR | - 54 - |
| FIG. 4.7: CONNECTOR TIP ANGLE AS A FUNCTION OF APPLIED FORCE..... | - 55 - |
| FIG. 5.1: ROTATIONALLY CORRECTED LORENTZ ACTUATOR SHOWING SIMULATED DIMENSIONS. | - 59 - |
| FIG. 5.2: (A) RC DEVICE MODEL MESH. (B)~(F) SNAPSHOTS FOR STRESS VALUES $\sigma_{C_r} = 1E8, 2E8, 3E8, 4E8, 5E8$ Pa, RESPECTIVELY, TO SHOW INCREASING ARM CURVATURE | - 61 - |
| FIG. 5.3: SIMULATED TIP HEIGHT VERSUS C_r STRESS FOR THE RC DEVICE AND THE BASIC DEVICE | - 63 - |
| FIG. 5.3: PLOT OF SIMULATED TIP HEIGHT VS LORENTZ FORCE FOR FOUR ACTUATION CASES. THE DIRECTION OF THE OUTSIDE ARM IS KEPT THE SAME WHILE THE INSIDE ARM SWITCHES FOR THE CASES WHEN BOTH ARMS ARE ACTUATED SIMULTANEOUSLY. | - 64 - |
| FIG. 5.4: (A) DIMENSIONS OF A SECOND RC DEVICE WITH WIDER OVERALL CROSSBARS. (B) SIMULATED TIP HEIGHT VS FORCE FOR THE TWO ACTUATORS. | - 66 - |
| FIG. 5.5: (A) EXTENDED TIP HEIGHT VERSUS ACTUATION FORCE PLOT FOR THE WIDE RC ACTUATOR SHOWING ACTUATION SYMMETRY ABOUT THE RESTING POSITION. (B) PROFILES OF THE CONNECTOR ALONG ITS | |

| | |
|---|--------|
| LENGTH FOR $f_{L-OUT} = 20\text{N/m}^2$ AND VARIOUS f_{L-IN} | - 69 - |
| FIG. 6.1: EXPERIMENTAL SETUP OF THE LORENTZ ACTUATOR PROBE STATION | - 72 - |
| FIG. 6.2: PICTURE OF A REPRESENTATIVE BASIC U-SHAPED ACTUATOR | - 73 - |
| FIG. 6.3: DEFLECTION VS DRIVE CURRENT FOR BASIC LORENTZ ACTUATOR | - 74 - |
| FIG. 6.4: ACTUATION SNAPSHOTS OF THE BASIC ACTUATOR, SHOWING THE ENTIRE ACTUATION PROCESS AND THE POST-RELEASE HEIGHT ADJUSTMENT PROCESS | - 76 - |
| FIG. 6.5: SIMULATED AND MEASURED DEFLECTION VERSUS CURRENT RESULTS FOR THE WIDER RC DEVICE | - 77 - |
| FIG. 6.6: DEFLECTION CHARACTERISTICS BEFORE AND AFTER LIFETIME TESTING OF 1.2 MILLION CYCLES | - 79 - |
| FIG. 8.1: INTERESTING EXTENSIONS AND ALTERNATIVE IMPLEMENTATIONS OF THE ROTATIONALLY CORRECTED ACTUATOR | - 86 - |

List of Tables

| | |
|--|--------|
| TABLE 2.1: THERMAL EVAPORATION PARAMETERS..... | - 7 - |
| TABLE 2.2: DETAILED PARAMETERS OF THE LITHOGRAPHY PROCESS..... | - 17 - |
| TABLE 2.3: PLASMA ETCHING OF PHOTORESIST PROCESS PARAMETERS..... | - 21 - |
| TABLE 2.4: XEF ₂ ETCHING PROCESS PARAMETERS..... | - 24 - |
| TABLE 2.5: PLASMA ETCH PROCESS PARAMETERS..... | - 26 - |
| TABLE 4.1: BASIC PARAMETERS OF THE FEM MODEL..... | - 49 - |

CHAPTER 1: INTRODUCTION

1.1 Motivation: Large-Deflection MEMS Actuators

Micromachined transducers have an advantage in a variety of applications for their reduced size, improved performance, and/or the ability to often incorporate electronics on the same substrate [7]. Ironically, there are some applications where their reduced sizes can be detrimental to the performance of the system. For instance, in micromachined switch based radio frequency (RF) phase shifters, the isolation between the micromachined switch and the underlying transmission line depends on their separation. An example of a micromachined RF device is shown in Fig. 1.1. When this cantilever switch device is actuated, the tip of the cantilever moves vertically and closes the circuit. A larger separation between the switch and the line would result in better isolation. Micromachined switch devices are commonly actuated using electrostatic force with 20V ~ 80V applied to the pull-down electrode, but consume very little power due to the nature of electrostatic actuation [16].

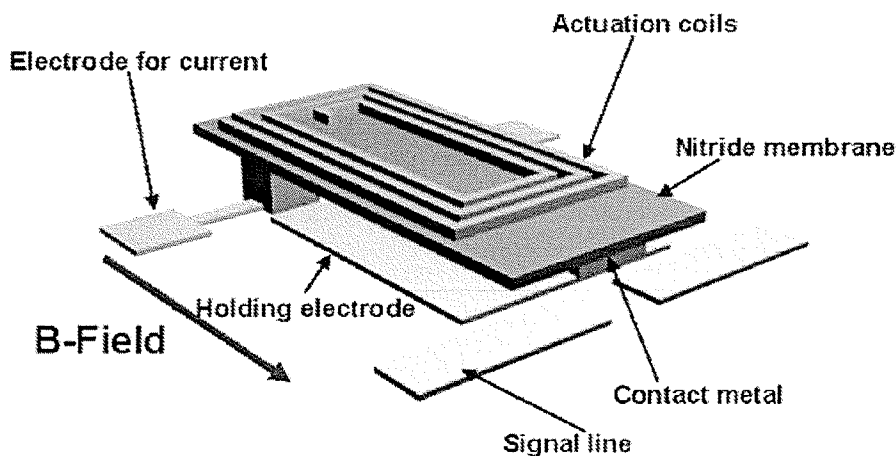


Fig. 1.1: Example of a micromachined RF switch device (image taken from [11]) © 2005 IEEE.

Another example where large-deflection in a micro structure is beneficial is an optical switch (micro-mirror), where a large angular motion is desired for maximum operating flexibility [15]. To date, most of the micro electro-mechanical (MEM) actuators research has focused on making the devices faster and more reliable. These requirements have often been achieved by making devices smaller in dimensions [17]. This thesis aims to address the lack of research in large-deflection MEM actuators (defined here as $> 100\mu\text{m}$ of range).

Another concern that hinders the compatibility of many electrostatic MEM actuators with electronics is the problem of high actuation voltages (tens of volts or higher). These high voltages arise due to the nature of electrostatic attraction force; the required voltage is quadratically related to the separation between the electrode and the device. Hence, in order to maximize the usability of large-deflection MEM actuators, their actuation voltage must be limited to within reasonable levels (defined as $< 10\text{V}$ in this work). This aspect of the actuators is also addressed in this thesis.

Last but not least, fabrication of the proposed actuator should require only conventional semiconductor processes (i.e. processes which have low height to width aspect ratios). This is a highly practical requirement for the device's fabrication compatibility with standard electronics facilities.

The requirements mentioned above will comprise a new species of actuators that has both large deflection and precision that a micromachined system offers. Furthermore, since the actuator does not require non-conventional processes, it can also be more readily integrated with existing technology.

1.2 Thesis Objectives

The main objective of this thesis was to develop a novel MEM actuator capable of $> 100\mu\text{m}$ out-of-plane deflection for applications such as RF phase shifters and micro-mirrors. Another goal was to keep the actuation voltages at a reasonably low level ($< 10\text{V}$) in order to maximize the usability of these actuators. This also required the fabrication of low profile devices, which enabled the use of standard processes, as opposed to high aspect ratio processes.

1.3 Organization of Thesis

Chapter 2 presents the reader with a description of the MEMS fabrication techniques used in this thesis. These techniques, or processes, are largely identical to those used for microelectronics fabrication with the exception of intent. The relevant parameters and methods used in each of the processing steps were also included here for future reference of the work done. Readers familiar with MEMS fabrication may skip this section.

A brief literature review of several existing large-deflection actuators, their designs and fabrication sequences are provided in Chapter 3. The merits and demerits of each device will be discussed, and these designs will serve as a good starting point for this work.

In Chapter 4, we start with the design of the proposed electromagnetic MEM actuator that is capable of large deflection with low voltages. The fabrication sequence of these actuators plays an important role in the success of these devices, and is presented alongside their designs. Detailed Finite Element Modeling (FEM) simulations on the

proposed designs provide good comparison with actual fabricated devices. These simulation results also shed light on the detailed behaviors of these devices under actuation. Furthermore, an advanced extension of this basic design is also proposed and simulated in Chapter 5. These advanced designs have the same large deflection as the basic designs while adding to it the ability to fine-tune their position at a much smaller magnitude throughout their range of travel.

Chapter 6 describes the various test setups used to characterize and verify the behavior of the fabricated actuators. The results gathered here will be discussed and compared in further detail to the simulated results from Chapter 4 and Chapter 5. The pros and cons of the proposed designs with respect to the intended types of applications are elaborated in Chapter 7. Finally, concluding remarks, recommended future work and summary completes this study in Chapter 8.

CHAPTER 2: MEMS AND MICROMACHINING TECHNIQUES

2.1 Overview

Micromachining is the fabrication of micrometer sized electro-mechanical systems using technologies originally used for integrated circuit (IC) fabrication. Since supporting IC circuitry can often be integrated on the same die, micromachined systems can reduce system size, cost and power consumption.

There are two main categories of micromachining techniques, surface micromachining and bulk micromachining. Bulk micromachining refers to the tactical removal of the “bulk” of the substrate on which the system is built. Surface micromachining refers to the deposition and patterning of various thin-films that will form the structure of the final device on the surface of a substrate. Surface micromachined devices are “released” from this substrate with the removal of a sacrificial layer underneath the moving structural layers. In this thesis, only surface micromachining techniques were employed since bulk micromachining is generally not a part of conventional processes.

In this chapter, each of the surface micromachining techniques used to fabricate the MEMS devices are briefly and individually introduced. The parameters and aspects of these techniques relevant to the devices fabricated in this thesis are also discussed. This includes any problems encountered/solved during the fabrication of the devices. While the description of these individual processes themselves may not convey much to the

reader on the overall objective of a large-deflection actuator, the actual fabrication sequence of these techniques as a whole should make more sense in Chapters 3 and 4.

2.2 Thermal Evaporation

Thermal evaporation is a common MEMS technique used to deposit a thin film of a source material onto a substrate. A simple evaporator setup is shown in Fig. 2.1.

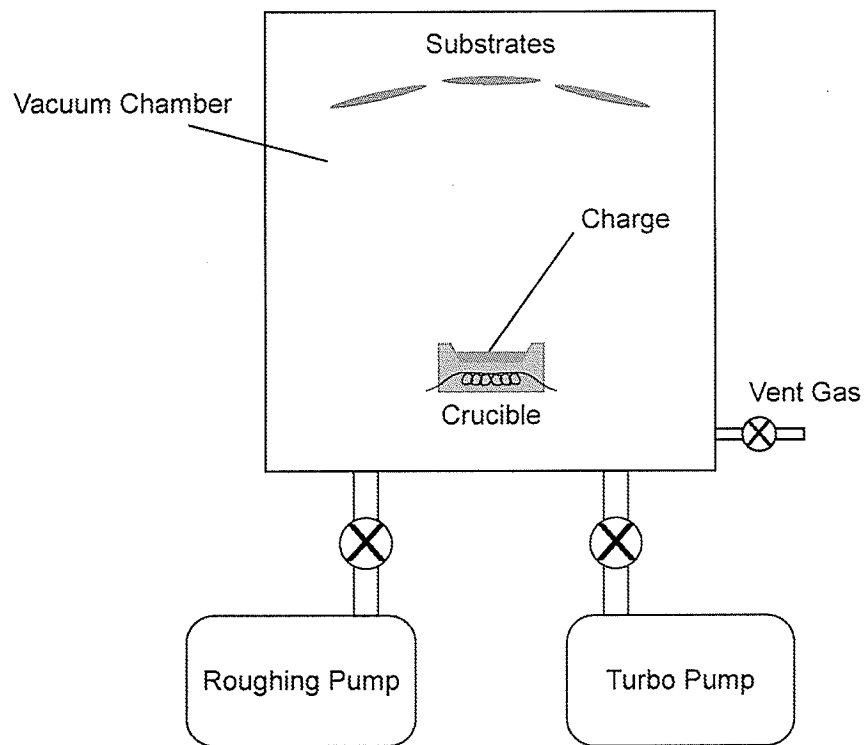


Fig. 2.1: A thermal evaporator schematic.

During the evaporation process, source materials are placed in a crucible or wrapped onto a tungsten rod, and then physically heated beyond its melting point in a vacuum chamber. The material evaporates and condenses when it hits colder surfaces inside the vacuum chamber. Hence, substrates (or wafers) placed above the crucible in Fig. 2.1 will get coated with the evaporated material. The pressure in the chamber is

typically on the order of 10^{-6} Torr in order to minimize ambient contamination during evaporation and to allow for a longer mean free path to the evaporated molecules.

Since the aluminum and chrome films deposited via thermal evaporation in this work are used as structural materials, one of the pertinent properties of the films is the residual film stress. The residual thin film stress depends on several factors, including chamber pressure during evaporation, deposition rate, substrate temperatures, and even the material itself. Deposition rate and substrate temperature usually have more significant effects on the resulting film stress. The detailed parameters are listed in Table 2.1. Consistent residual film stresses can be obtained with careful control of their parameters. It should be noted that the equipment available did not allow control over substrate temperature, and it was kept at room temperature plus the effects of hot atoms that condense at the substrate surface during evaporation. The stress levels in the evaporated films were obtained using the Toho FLX-2320 thin film stress measurement system. A more detailed discussion of thin-film stresses is provided in section 2.4.

TABLE 2.1: THERMAL EVAPORATION PARAMETERS

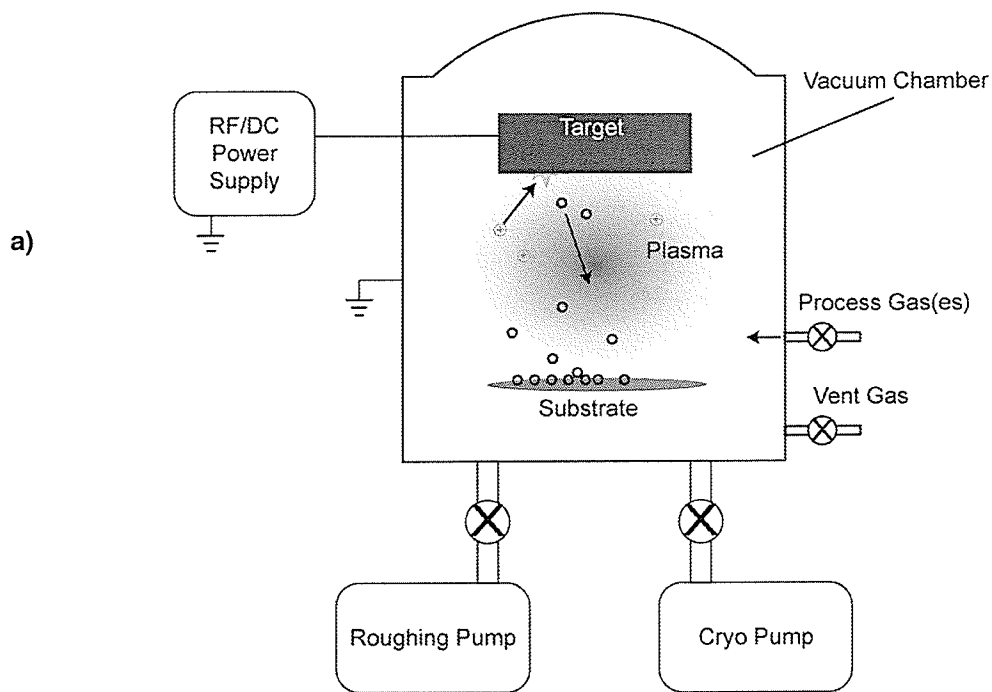
| Material | Deposition Rate ($\text{\AA}/\text{sec}$) | Pressure During Evaporation | Film Stress |
|----------|---|-----------------------------|--------------------------------|
| Aluminum | 15 ~ 17 | Mid 10^{-6} Torr | Very Low Compressive (< 35MPa) |
| Chrome | 3 ~ 5 | Mid 10^{-7} Torr | Tensile (300MPa ~ 700MPa) |

A characteristic of films deposited using evaporation is relatively poor step coverage on existing structures already on the substrate. This is due to the near point-source geometry of the evaporator setup together with a long mean free path of evaporated molecules from the low evaporation pressures. This can potentially cause

structural weak spots at the step edges in the devices fabricated, leading to premature breakages under actuation. A trivial solution to this problem was to have a thinner bottom layer relative to the top layer, or a thicker top layer to ensure proper step coverage.

2.3 Sputter Deposition

Sputter deposition of thin-films is another common technique used to coat substrates. Fig. 2.2a illustrates the basics in a sputter system.



b)

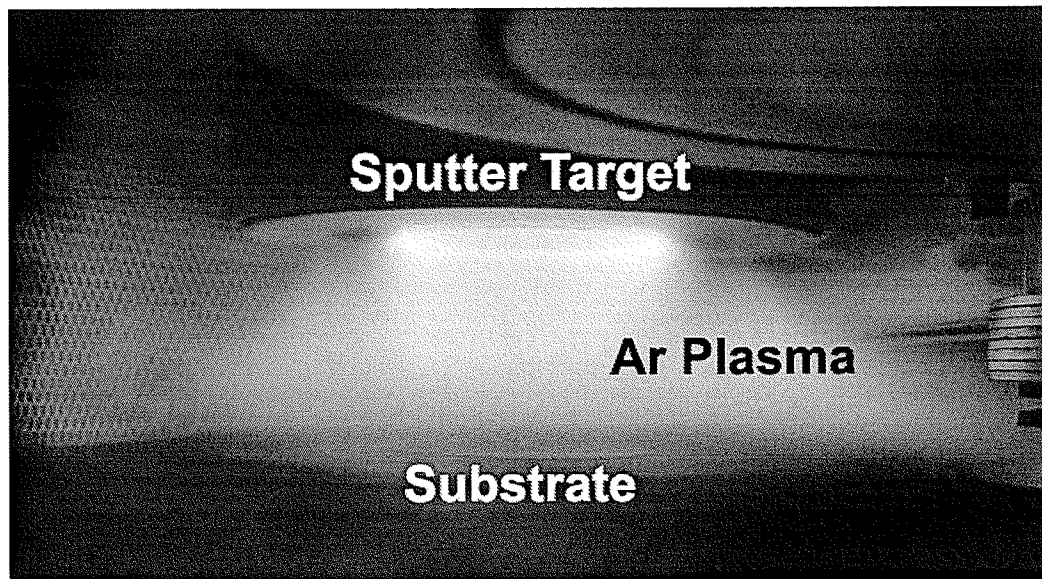


Fig. 2.2: (a) Illustration of a basic sputter system. (b) Photograph of silicon sputtering in progress.

In sputtering, an inert gas plasma is induced between two electrodes using either DC or RF biases. In DC sputtering, the high energy plasma ions (positive) accelerates toward the target (the negatively biased cathode) consisting of the material which we wish to deposit and physically knock atoms off of its surface. The substrate is placed directly

beneath the target, where the target atoms will land on and thus coat the substrate with the desired material. The deposition rate is proportional to the number of ions bombarding the target and the incident ion energies (bias voltages).

Although the plasma can be induced using either DC or RF biases, DC sputtering can only be used when the target is non-insulating due to the fact that insulating surfaces charge up with the bombarding ions, which eventually counters the applied bias and stops the sputtering process.

Silicon and aluminum were the only materials sputtered in this project. The sputtering of silicon, shown in Fig. 2.2b, was done using RF magnetron sputtering in an Argon working gas at 1.6×10^{-2} Torr (corresponding to Ar flow rate of 64.5 sccm). The forward RF bias applied ranged from 350W ~ 400W, resulting in a deposition rate of approximately $30 \text{ \AA}/\text{sec} \sim 35 \text{ \AA}/\text{sec}$. This silicon film was used as a sacrificial layer, which means the only film quality of significance was the step coverage. In general, step coverage in sputtered films tends to be much better compared to evaporated films, mainly due to the higher chamber pressures during deposition, larger target size, and closer target to substrate spacing.

The sputtering of aluminum was done using DC sputtering, also in Ar working gas at 16mTorr, with 100W power. This recipe allowed for a deposition rate of approximately 35nm/min. Sputtered aluminum films were used for contact pads and wiring in this work, and therefore its mechanical properties are not of interest here.

2.4 Stress in Thin Films

Stress in deposited films can either be tensile, where the film tends to contract after

deposition, or compressive, where the film tends to expand. Too much stress will cause the film to peel itself off the surface, or cause a released structure to buckle out of plane.

Fig. 2.3 illustrates how a deposited film with stress would affect a substrate.

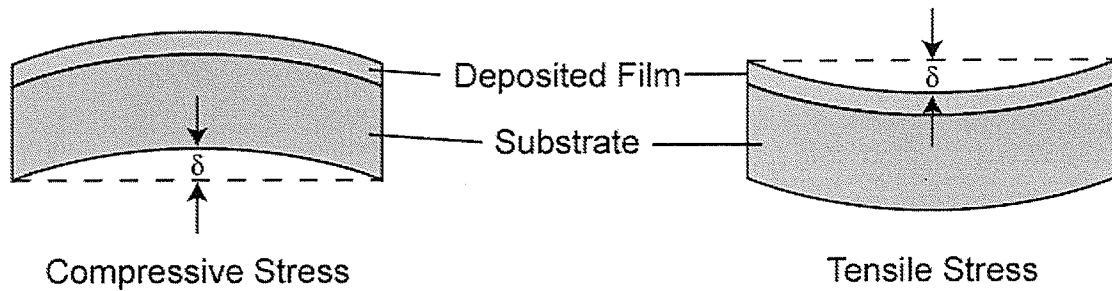


Fig. 2.3: Effects of film stresses on a wafer (exaggerated). The deflection δ in the wafer can be measured using a surface profiler.

There are several factors which affect film stress. These include the deposition technique used, substrate temperature, thermal expansion coefficients between the deposited film and the substrate, deposition rate, Young's modulus of the films, and other factors. These factors altogether make it difficult in aiming for a specific residual stress in the deposited film. In this work, the lack of ultra precise deposition and monitoring equipments has prevented us from characterizing the exact stress levels of films used. However, despite the lack of exact control, a given set of processing parameters usually resulted in consistent film stresses in the same order of magnitude. More specifically, the thermal evaporation of aluminum as described in section 2.2 usually resulted in films with very little stress, where as the evaporated chrome was always significantly tensile relative to the aluminum.

What is important about residual film stress in this work is that manipulation of these stresses has been used in literature to obtain out-of-plane structures in MEMS devices [2]. For example, cantilevers fabricated from low-stress aluminum with a tensile

chrome layer on top will result in an out-of-plane curvature as illustrated in Fig. 2.4c. This film stress mismatch technique was used in this project for several good reasons. The first reason was to improve device release characteristics, where 45 out of 50 bi-layer devices were successfully released, compared to just 3 of 32 for devices without the tensile layer on top. Another reason Al/Cr films were used was to give the out-of-plane cantilevers a predetermined rest height and angle when not under actuation. Finally, the use of Al/Cr films allowed the devices to achieve a large out-of-plane deflection without the use of high aspect ratio processes. These two reasons will make more sense when the actual design of the proposed actuator is presented.

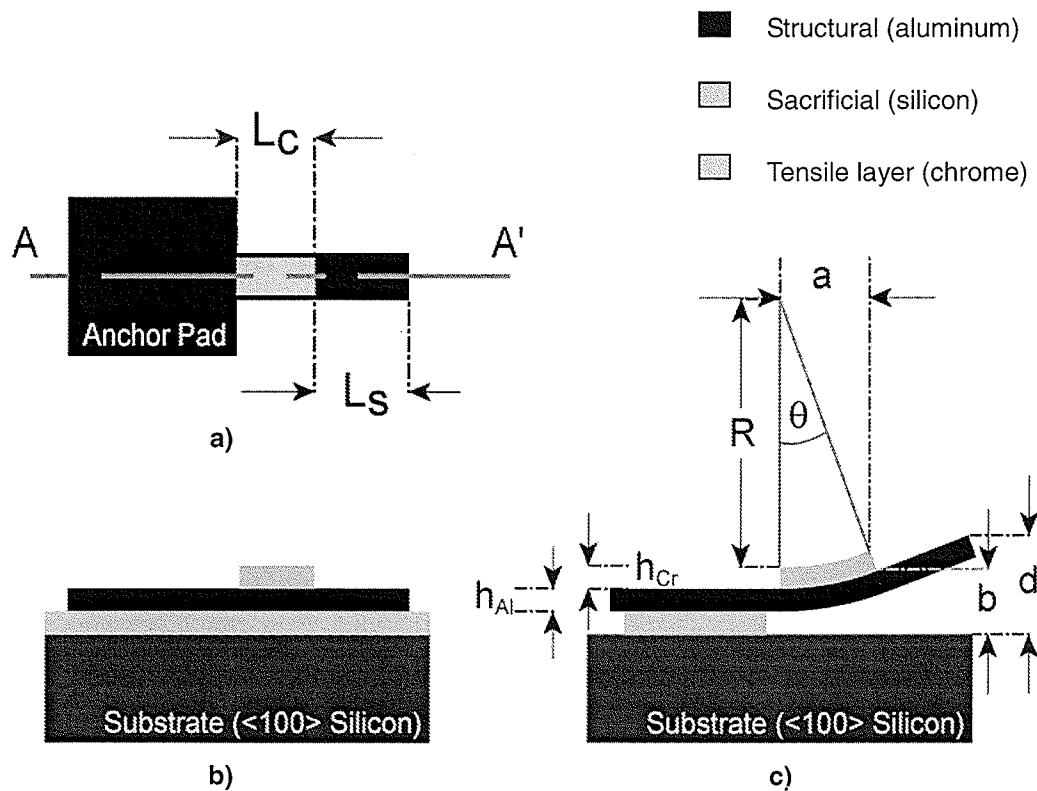


Fig. 2.4: (a) Top view of curved cantilevers before release. (b) Cross section view of curved cantilevers before release. (c) Side view after release showing radius of curvature R (not to scale).

An important parameter of interest with regard to out-of-plane curvature is the

radius of curvature, R in Fig. 2.4c, of the bimetallic cantilevers. This parameter determines the initial rest angle and height of the cantilevers, and can be calculated using the following equations [2]:

$$R = \frac{E_{Al} h_{Al}}{6(m\sigma_{Al} - \sigma_{Cr})} f(m, n) \quad (2.1a)$$

$$f(m, n) = \frac{1 + 7mn + 12mn^2 + 7mn^3 + m^2n^4}{n(1+n)} \quad (2.1b)$$

$$m = \frac{E_{Cr}}{E_{Al}} \quad (2.1c)$$

$$n = \frac{h_{Cr}}{h_{Al}} \quad (2.1d)$$

where h is the film thickness, E is Young's modulus, and σ is film stress. From equation 2.1 we can see that R is affected by both the thickness ratio as well as the stress levels in the two films. One way of controlling R is to fix a stress level and vary the thickness ratio n . Fig. 2.5 plots the calculated R versus n using equation 2.1a for $\sigma_{Cr} = -450\text{MPa}$ and $\sigma_{Al} = 0\text{Pa}$. For small n values (e.g. < 0.01), R varies too rapidly within fabrication tolerances. For larger n values (e.g. > 0.03), R barely changes. Therefore, it was difficult in practice to control the initial rest height of the cantilever tip by controlling n . Instead, the initial rest angle and height of the cantilevers were more readily controlled by keeping the thickness ratio n and stress level constant (hence fixating on a particular value for R), and manipulating the length of the tensile Cr beam L_c relative to the cantilever length instead. This way the resting height of the bimetallic structures was controlled with much more practicality and consistency, because it now depended on the design of the mask rather than the control of the fabrication parameters.

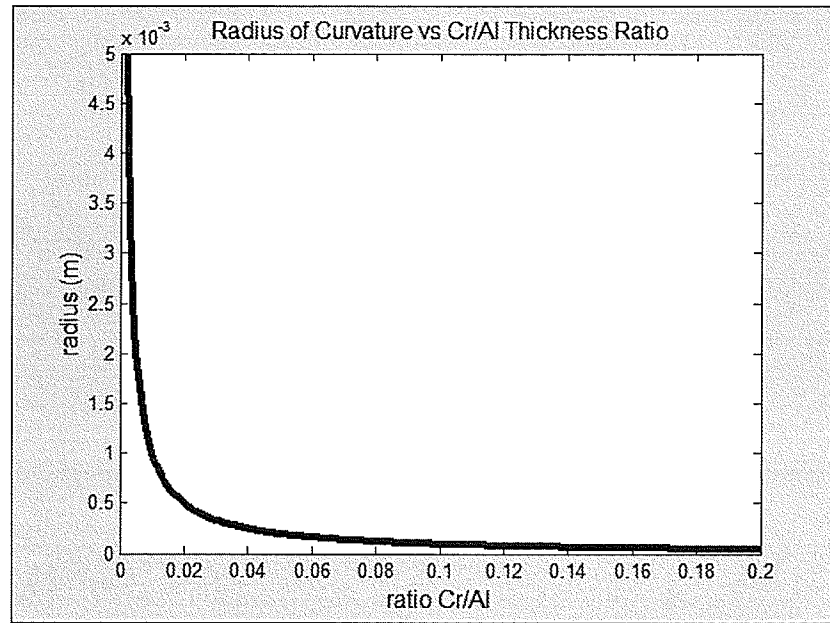


Fig. 2.5: Calculated radius of curvature R versus Cr/Al thickness ratio n for $\sigma_{Cr} = -450\text{MPa}$ and $\sigma_{Al} = 0\text{Pa}$ (see Appendix C for full Matlab code used for this calculation).

Given a fixed radius of curvature, the initial resting angle θ and tip height d of a stressed bimetallic cantilever can be calculated using trigonometry (refer to Fig. 2.4 for the variable names):

$$d = (\sin \theta)L_s + R(1 - \cos \theta) \quad \text{for } \theta < \pi / 2 \quad (2.2)$$

$$\theta = \frac{L_c}{R} \quad (2.3)$$

A practical way of verifying the radius of curvature of actual fabricated devices is to experimentally measure the dimensions a and b as illustrated in Fig. 2.4c. Once again using trigonometry, we obtain an alternative formula for R :

$$R = L_c / 2 \tan^{-1}\left(\frac{b}{a}\right) \quad (2.4)$$

This equation is valid for $b \gg h_1$ and h_2 .

2.5 Photo-lithography and Photoresist Patterning

Photo-lithography, or simply lithography, is a pattern transfer technique widely used in the fabrication of semiconductor devices. In this process, a design was first transcribed onto a set of photomasks, each containing an image of a layer of the fabrication process. During the patterning of each layer in the process, a thin, uniform photosensitive material, photoresist, is first spun-coated onto the substrate. The coated substrate is then exposed to a UV optical source through one of the photomasks, causing the exposed photoresist to undergo a chemical reaction. Positive photoresist was used, and so the exposed regions of photoresist dissolve away in a developer solution to complete the pattern transfer. The substrate is then immersed in an acid that attacks the exposed regions of the substrate, but not the regions protected by the patterned photoresist. When the etching is complete, the photoresist was stripped away. The result is a substrate with patterned top layer identical to the photomask pattern. At various points during the lithography process, the photoresist film has also went through a series of soft and/or hard bakes to ensure proper chemical and mechanical properties (such as solvent content) of the film. An overview of a typical lithography process used for masking in this project is shown in Fig. 2.7.

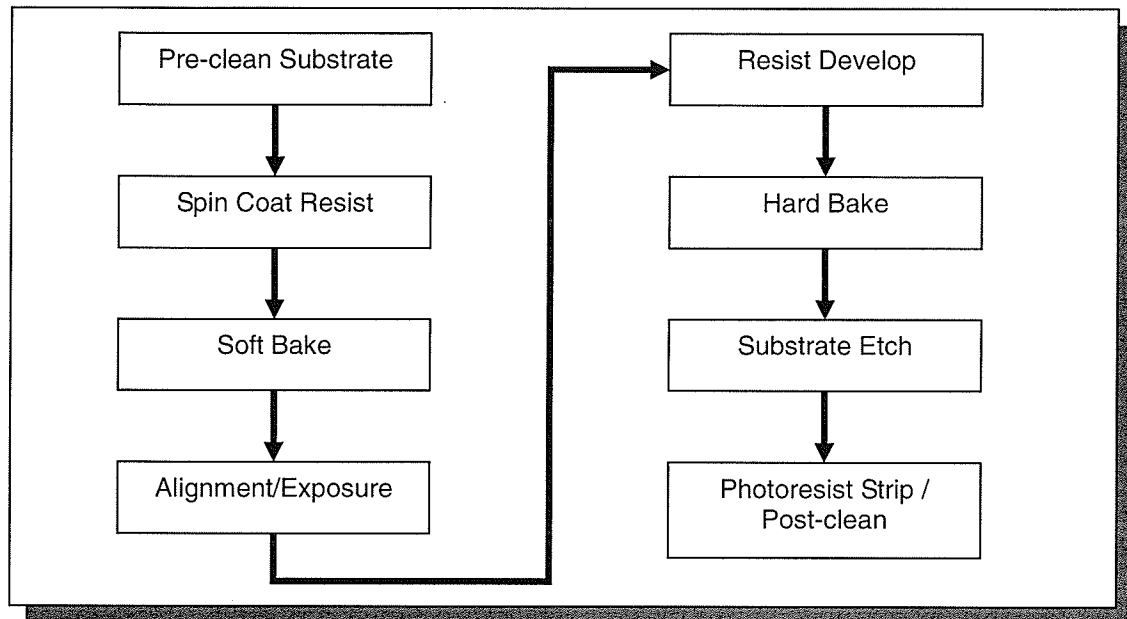


Fig. 2.7: Overview of a typical lithography process.

For microelectronic fabrication, the main factor in a lithography process is the resolution, or smallest reproducible line width. This is dependent on the exposure tool, exposure time, baking durations and temperatures, as well as the species of the photoresist itself. The equipment and photoresist used in this project allowed a minimum feature size of approximately $1\mu\text{m}$, which was mainly limited by the ability to align the photomask to previously defined features on the substrate. This $1\mu\text{m}$ resolution was ample in the design and fabrication of the large deflection devices under consideration. For cost reasons, photomasks with minimum feature size of $7\mu\text{m}$ were actually used. Table 2.2 lists the detailed parameters used in all the lithography processes. The photoresist patterns produced this way were used as masks in all etching processing steps.

TABLE 2.2: DETAILED PARAMETERS OF THE LITHOGRAPHY PROCESS

| | |
|-----------------------------------|-------------------------|
| Mask Aligner Model | Karl Suss MA-3 |
| Exposure Time | 1.5 minutes |
| Photoresist | Olin Hunt HPR 506 |
| Soft bake | 110°C, 60 seconds |
| Hard bake | 120°C, 20 minutes |
| Developer | Olin Hunt HPRD 419 |
| Spin Coat Speed | 3500 rpm |
| Resulting Resist Thickness | Approx. 2 μm |

2.6 Sacrificial Materials

Sacrificial layers are essential in any surface micromachining process. The removal of this layer at the end of a fabrication process allows the structural layer to “release” from the substrate and gain movement. This process is crucial to the reliability of the fabricated batch and should be treated with care to minimize catastrophic stiction (adhering of two surfaces from surface forces, such as surface tension and Van der Waals forces) of the devices. Two different materials have been used as sacrificial materials in this project: photoresist and sputtered silicon. For both materials, a discussion of the problems associated with the release of each material and how they were overcome is given.

2.6.1 Photoresist Sacrificial

Photoresist has been used in MEMS as sacrificial material mainly for the significant reduction of processing steps associated with it [3]. However, the main

drawback was the lowered maximum processing temperature (e.g. $< 200^{\circ}\text{C}$), beyond which photoresist tends to burn. Since no high temperature steps were required in the processing of our proposed devices, photoresist was the first choice of sacrificial material for this work. The photoresist used in this work is the Olin Hunt HPR506.

The requirements for sacrificial photoresist patterning are different than that of regular lithography photoresist. First of all, in order to be used as sacrificial, the solvents within the photoresist needed to be completely removed prior to the deposition of a structural layer on top. Remaining solvents inside the sacrificial photoresist would tend to out-gas when heat is applied in a later processing step. Hence, the structural layer on top of the sacrificial would serve as air-tight seals to these out-gassing solvents, resulting in undesirable trapped air bubbles which cause layer deformation. This problem is shown in Fig. 2.8, where the trapped bubble deformations are clearly visible for areas where underlying sacrificial photoresist is present. This was the case when the photoresist processing parameters as outlined in Table 2.2 was used.

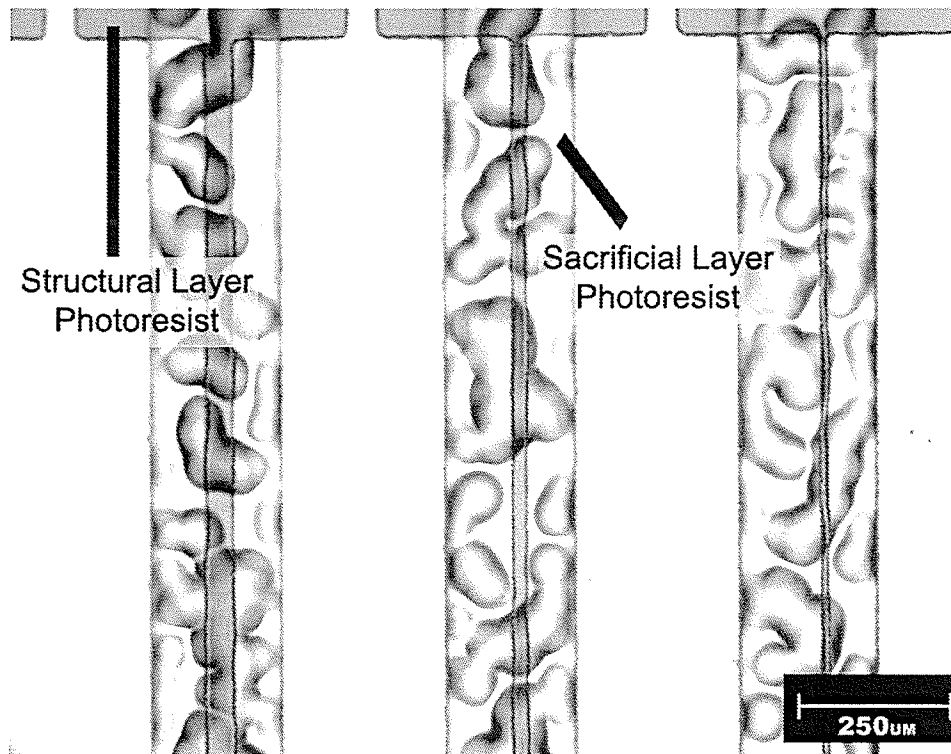


Fig. 2.8: Bubbling of the structural layer caused by out-gassing of solvents in the photoresist sacrificial. Image adapted from [4].

In order to overcome the solvent out-gassing problem, two methods were considered: extended hard or soft bake durations. One set of devices was fabricated with an extended duration of soft baking of 20 minutes at 90°C instead of the one minute at 110°C prescribed in Table 2.2. A second set was fabricated with an extended duration of hard baking of 40 minutes at 120°C instead of 20 minutes at 120°C . With all other lithography parameters held the same, the extended soft bake devices showed no initial signs of solvent out-gassing during the deposition of the overlying structural layer. However, during the heat treatment in the following fabrication step, bubbles underneath the structural layer were observed. This shows that the solvents in the sacrificial photoresist were not completely displaced with the extended soft bake.

On the other hand, the extended hard bake devices showed almost no bubbles throughout the remainder of the fabrication process. From this observation, we have concluded that the bulk of the solvents in the HPR 506 photoresist can be driven off with an extended bake at 120°C. This extended hard bake was used in the lithography of all subsequent photoresist sacrificial layers.

The second requirement of employing photoresist sacrificial was its proper removal at the end of a device fabrication. A “proper” removal of sacrificial involves the minimization of stiction, a common micromachining phenomenon where a released device is stuck onto the substrate, preventing motion of the moveable structures and rendering the devices useless. One of the most common reasons stiction occurs in MEMS devices is due to surface tension of the liquid sacrificial etchant between the structure and the substrate. As the liquid is removed, surface tension pulls the released device into contact with the substrate, and it might stay stuck, possibly due to hydrogen bonding [1].

The first attempt to releasing the devices was done in a simple non-agitated acetone bath that dissolved the photoresist sacrificial completely in approximately three to five minutes. Since the released devices were particularly fragile to running liquids (rinsing with DI water), the devices were either air dried directly for approximately 10 minutes, or alternatively soaked in a still DI water bath for five minutes and then air dried. Stiction was observed on *all* of the devices fabricated that were released in this fashion. An alternative method was clearly needed.

An attempt to minimize stiction was to minimize the surface tension of the releasing liquid. One way to minimize surface tension was to elevate the temperature of

the releasing liquid. Two sets of devices were both released again in room temperature acetone bath, and then treated to two different elevated temperature processes. One set was simply dried directly without rinsing on a hot plate at 50°C. The other set went through a two step process of first soaking in still DI water bath for five minutes, followed by soaking in boiling DI water bath for ten minutes, and finally dried on a hot plate. The results of the first process showed that still none of the devices were free of stiction. This indicated that the elevated acetone drying temperature was ineffective. On the other hand, the devices released using the two-step DI water drying showed a small improvement, with 4 of 27 devices free of stiction. The improvement was attributed to the better removal of photoresist residue at stiction prone areas using the water baths. Despite this improvement, this device survival ratio was still poor.

In order to further improve the device survival ratio, a dry release method was needed. In literature, photoresist has been successfully dry etched typically using an isotropic oxygen plasma asher [3, 5]. In this thesis, a plasma/reactive ion etching (RIE) chamber was used as a close substitute with the following parameters:

TABLE 2.3: PLASMA ETCHING OF PHOTORESIST PROCESS PARAMETERS

| | |
|------------------------------|-------------------------|
| Plasma Etcher Model | Trion ICP Plasma Etcher |
| Chamber Pressure | 800 mTorr |
| ICP Power | 800 W |
| RIE Power | 400 W |
| Etch Duration | 30 minutes |
| Chamber Gas/Flow Rate | 50 sccm O ₂ |

This setting allowed most of the exposed photoresist to be etched away. However, due

to the anisotropic nature (or directionally dependent etch, in this case perpendicular to the substrate) of the RIE etch, removing the sacrificial beneath the structures required a relatively long etch duration of 30 minutes. There was improvement in the device survival ratios compared to the wet release techniques. Unfortunately, upon closer inspection, the devices released this way appeared to have some unetched photoresist residue on the bottom side, which tended to facilitate stiction upon contact with the substrate.

Finally, the sidewall profile of photoresist sacrificial also had an impact on the reliability and survivability of the final devices. Most photoresists commercially available were intended for the smallest line width in microelectronic applications. Hence, they all have a relatively steep sidewall profile. Recall from section 2.2 that films deposited by thermal evaporation had poor sidewall coverage. The combination of poor coverage with a steep profile causes devices to break at these structurally weak points. Therefore, device lift-off and the many problems encountered in processing lead to the decision that *photoresist sacrificial was unsuitable* for this project. For further reading, Bartek et al. has remedied the sidewall profile problem using an advanced exposure technique [5]. In their work, they have utilized multiple shifted exposures of the same pattern to control the photoresist sidewall profile. This technique was difficult to achieve with the mask aligner available to the author.

2.6.2 Silicon Sacrificial

The second sacrificial material chosen was silicon. Silicon was chosen primarily due to its ease of removal in an isotropic xenon difluoride (XeF_2) gas etch as well as a

plasma etching system. Both these processes are gas-based, or so called “dry-release”, which circumvents the stiction issues related to wet-release techniques as discussed in section 2.6.1. The etching selectivity of silicon to the structural material, aluminum, was also very high, which allowed easy removal of any sacrificial residues with overetch [8]. The sacrificial silicon was deposited through sputtering as described in section 2.3 with thicknesses ranging from 200nm to 350nm.

The removal of the sacrificial silicon underneath the structures requires an isotropic etch process (etch rate is nominally equal in all directions). Therefore, isotropic XeF_2 gas etching was used as the final dry release process. The details of this process are provided in section 2.8. Devices fabricated with silicon sacrificial in conjunction with the Cr/Al bimetallic structure and XeF_2 etching showed survival ratios as high as 45/50. This indicated a reliable set of processes which we can build the proposed devices on.

2.7 Isotropic Wet Etching

After a photoresist pattern has been defined on a substrate, this pattern is often transferred onto the underlying layer using wet chemical etching. The substrate is immersed in an etchant designed to chemically attack one material while etching the masking material at a much slower rate, if at all. This is purely a chemical process. Most wet chemical etching of metals attack all exposed surfaces at an equal rate, or isotropically.

The aluminum and the chrome layers were both patterned using isotropic wet etching. The etching of aluminum was done with gentle agitation in a heated bath of H_3PO_4 phosphoric solution (70% phosphoric acid, 15% acetic acid, < 5% nitric acid) at 50 degrees Celsius. This recipe has an etch rate of approximately 400nm/min. The

etching of chrome, on the other hand, was done also with gentle agitation in a room temperature mixture of HNO₃ nitric acid (15% ceric ammonium nitrate, < 7% nitric acid) at approximately 70nm/min. Photoresist as prepared in section 2.5 was used as the masking layer for all wet etches.

2.8 Isotropic XeF₂ Silicon Etching

XeF₂ gas has been shown to etch silicon without external excitation such as heat or plasma, making it a very simple isotropic etching process [6]. In this work, etching of silicon sacrificial was performed in a XeF₂ chamber. During an etching process, the chamber was filled with XeF₂ etchant gas and allowed time to attack the exposed silicon. After the allowed period, the expensed gases and byproducts were pumped out, followed by a nitrogen purge. XeF₂ etchant was either introduced again to continue the etch process, or upon completion the chamber was purged and then vented with nitrogen. The process parameters were summarized in the following table.

TABLE 2.4: XEF₂ ETCHING PROCESS PARAMETERS

| | |
|--|------------|
| Chamber Pressure During Etch | 5 mTorr |
| XeF₂ Etch Duration Per Cycle | 90 seconds |
| N₂ Purge Duration Per Cycle | 30 seconds |
| Etch Cycles | 10 ~ 15 |

Complications to the XeF₂ etching process exist due to the reactivity of XeF₂ with water (i.e. moisture in air) [7]. The effect of this reactivity is such that the etch rate of silicon slows down dramatically when there is moisture in the chamber. Thus, the chamber was purged with nitrogen several times at the start of the etch to keep the

moisture level low.

When a large area of silicon is exposed to the attacking XeF_2 gas all at once, the etch rate across the entire substrate varies due to localized saturation of reactions. This is known as loading effect, and typically results in prolonged etching times. A practical way to avoid long XeF_2 etches was to first anisotropically etch away all the exposed silicon using plasma/reactive ion etching (higher silicon etch rate), and then perform XeF_2 etching on the remaining silicon. By removing the bulk silicon using plasma etching, this minimizes the loading effect during the XeF_2 etching.

2.9 Plasma/Reactive Ion Etching

Plasma etching and reactive ion etching (RIE) is a common etching technique utilizing a combination of reactive chemistry and physical ion bombardment. As a result, the etch profile (isotropic/anisotropic) can be adjusted through variation of the bias potentials, gas flow rates, pressure, and even temperature. For this project, a 90% CF_4 – 10% O_2 Si plasma recipe was used to pattern the silicon sacrificial just before the final release. An anisotropic recipe was utilized to avoid premature undercut of the devices. Another reason silicon was etched using plasma before the final XeF_2 release was to minimize loading effects during the final XeF_2 release. The settings for silicon plasma etching are listed in the following table.

TABLE 2.5: PLASMA ETCH PROCESS PARAMETERS

| Plasma Etcher | Trion ICP Plasma Etcher |
|---------------------------------|-------------------------|
| Chamber Pressure | 150 mTorr |
| CF₄ Flow Rate | 45 sccm |
| O₂ Flow Rate | 5 sccm |
| RIE Power | 50 W |
| ICP Power | 350 W |
| Etch Duration | 60 seconds |
| Etch Rate | 400 nm/min |

2.10 Chapter Summary

Each of the micromachining techniques used in the fabrication of the devices in this thesis has been introduced in this chapter. A set of properly characterized techniques is crucial in the ultimate success of the devices. Some of the techniques were discussed in more detail than others, due to the problems encountered and/or solved in the pursuit of successful fabrication sequences of the proposed devices. All the relevant parameters in these steps were provided in detail for future work.

CHAPTER 3: LITERATURE REVIEW

3.1 Overview

In this chapter, a short literature review on existing large-deflection micromachined actuators is provided. Before these designs are presented, brief background theory on electrostatic actuation and electromagnetic actuation are included for completeness. Following this chapter, the reader should have a good idea of how researchers prior to this work have tackled the problem of creating a large-deflection actuator in surface micromachined MEMS. The advantages and disadvantages of each design pertaining to the objectives of this thesis are also discussed.

Because the fabrication of the cascaded electrostatic cantilevers in the following section is very relevant to this work, we have also replicated this device in our own laboratory. Successful fabrication of these devices established a “control” set of fabrication processes with which we built our proposed devices. A short section discussing some of the results obtained here also reveals valuable information towards the successful fabrication of our large-deflection actuator.

3.2 Electrostatic Actuation Theory

Electrostatic actuation is the most common type of actuation used in RF MEMS switches [9, 7]. These devices require near-zero holding power and are relatively fast compared to other types of MEMS actuators. A typical in-line electrostatic switch is shown in Fig. 3.1. In these types of switches, an insulated pull down electrode is placed

underneath the switching cantilever. When electric potential is applied across the cantilever and the electrode, electrostatic forces draw the cantilever towards the electrode. By increasing the potential until the pull-down voltage, the switch eventually closes. The required pull-down voltage increases quadratically with electrode-cantilever separation. Therefore, in order to maintain a low pull-down voltage, the initial rest height of the cantilever is typically minimized. Unfortunately, this contradicts the goal of this project which is to maximize this initial separation while keeping the actuation voltage at a reasonable level. This is a problem to be addressed in next section.

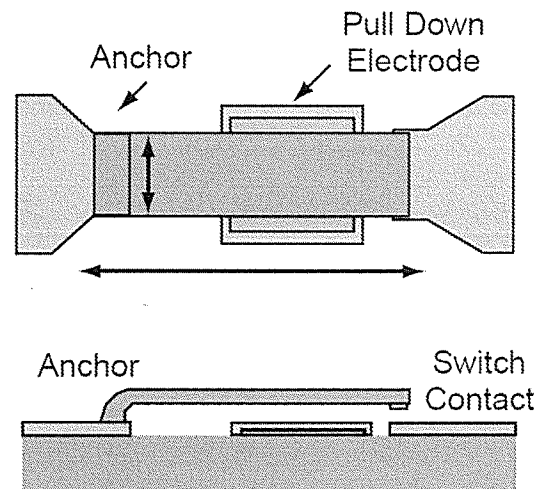


Fig. 3.1: Typical structure of an in-line MEMS Electrostatic Switch [9] © 2001 IEEE.

A characteristic of electrostatic actuators is that there is limited control over the position (height) of the moving cantilever during actuation. This is a result of the rapidly increasing nature of electrostatic forces between electrodes as the switch moves downwards. In other words, the entire switch quickly “snaps-down” once a certain critical voltage has been reached.

3.3 Cascaded Electrostatic Cantilevers

The first device reviewed is the cascaded electrostatic cantilevers. Because of the high relevance of this type of device to this thesis, it has been reviewed in greater depth than other devices in this chapter.

3.3.1 *Design and Actuation Principle*

Traditionally, surface MEMS devices have very small aspect ratios due to the nature of the silicon-based technology. In order to fabricate structures which stood out-of-plane with a large height, high aspect ratio processes such as LIGA or excellent sidewall coverage deposition are often required. However, one of the biggest challenges of this thesis was to create a MEM switch with out-of-plane deflection in the order of hundreds of microns without using such exotic processes. One of the methods used to achieve such a device in literature was the bimorph cantilever with differential thin film stresses in each material as described in section 2.4. However, if the single bimorph cantilever described in section 2.4 was actuated using electrostatic attraction, the required voltage would still be large due to its large resting height.

Yasuda et al. has overcome this problem by cascading several smaller bimorph cantilevers, each of which has a small deflection in itself [2]. The structure is illustrated in Fig. 3.2a, where each cantilever has a curved section plus a straight section. By attaching the cantilevers as shown, the overall tip height can be made very large. This cascaded effect is illustrated in Fig. 3.2b. The curvature of the individual arms and the increasing tip height of each stage are clearly visible.

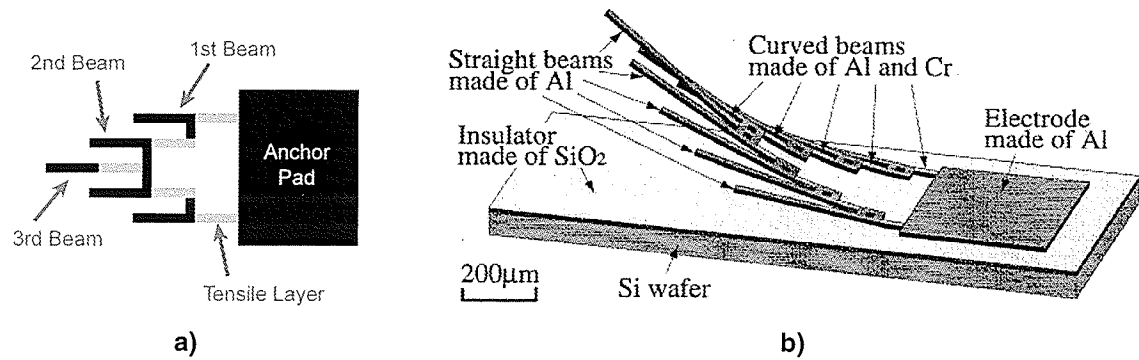


Fig. 3.2: (a) Top view of the cascaded bi-layer cantilevers. (b) Isometric view of a cascaded electrostatic actuator at rest (illustration (b) taken from [2]) © 1997 IEEE.

These cascaded cantilevers were actuated using electrostatic force. When a voltage is applied to the cascaded structure, the first beam experiences a large electrostatic force due to the smaller separation distance (Fig. 3.3a). Hence, the first beam bends the structure towards the substrate. This results in a situation shown in Fig. 3.3b where the second beam is now at the same separation to the substrate as the first beam was in Fig. 3.3a. The structure therefore continues to bend towards the substrate, until the last beam is pulled down as shown in Fig. 3.3d. This entire process happens abruptly once the critical voltage is reached.

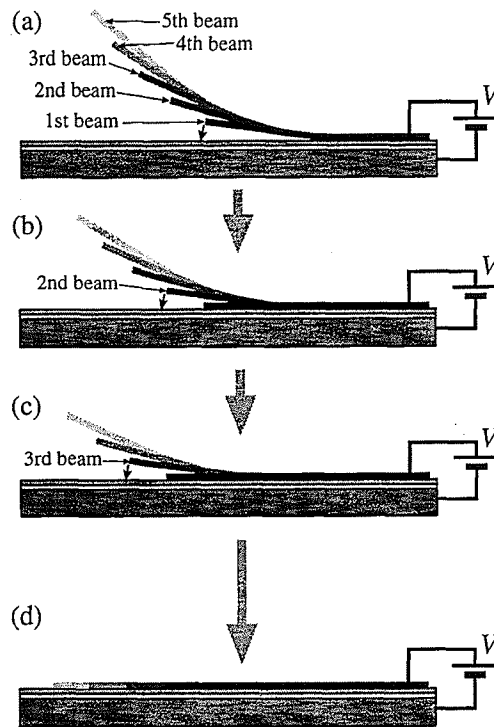


Fig. 3.3: (a) Initial position of cascaded structure. (b) After the 1st beam pulls down. (c) After the 2nd beam pulls down. (d) End position after actuation (all illustrations taken from [2]) © 1997 IEEE.

The cascaded structure of these electrostatic actuators allows them to be “switched” with a much smaller voltage (as low as 11.8V instead of several tens of volts) for a 245 μ m overall deflection. The dependency of this critical-snap down voltage on device dimensions was studied by Yasuda et al. in greater detail and is not the focus of this work. However, it should be noted that there is very little control of the position of the cascaded cantilevers – it is essentially an ON-OFF switch due to the nature of electrostatic actuation.

In summary, the cascaded electrostatic bimorph cantilevers show very desirable characteristics to the requirements of this thesis: large deflection, low voltage, and conventional fabrication. More in depth study of these devices in the next section will reveal some of the drawbacks associated with these cascaded devices.

3.3.2 *Fabrication of Cascaded Electrostatic Actuators*

As part of the preparation work done in this thesis, we have replicated the cascaded electrostatic actuators from Yasuda's work in our own set of processes. Fabrication of these actuators was a two-mask process illustrated in Fig. 3.4. The sequence begins with the sputtering of a 300nm sacrificial polysilicon layer, followed by thermal evaporation of a 630nm aluminum structural layer, and lastly evaporation of a 110nm chrome tensile layer onto a silicon substrate pre-coated with 1 μ m of wet thermal SiO₂. The first mask is used to pattern the tensile Cr layer, which is then wet etched. The aluminum is patterned next using the second mask and also wet etched. This defines the main structure of the cascaded cantilevers and results in the pre-release top view in Fig. 3.4. The fabrication completes with the release of the devices by isotropic etch of the underlying silicon sacrificial layer. Note that no patterning of the sacrificial layer was required thanks to a mask design technique where the anchor pads were made to be much larger than the undercut rate of the final release. Thus, the devices will all have been released well before the anchor pads are completely undercut. As an added benefit, this technique also circumvents the potential structural weak points caused by any sidewall coverage issues over step edges of a patterned sacrificial. The detailed parameters for each of the above processes can be found in chapter 2.

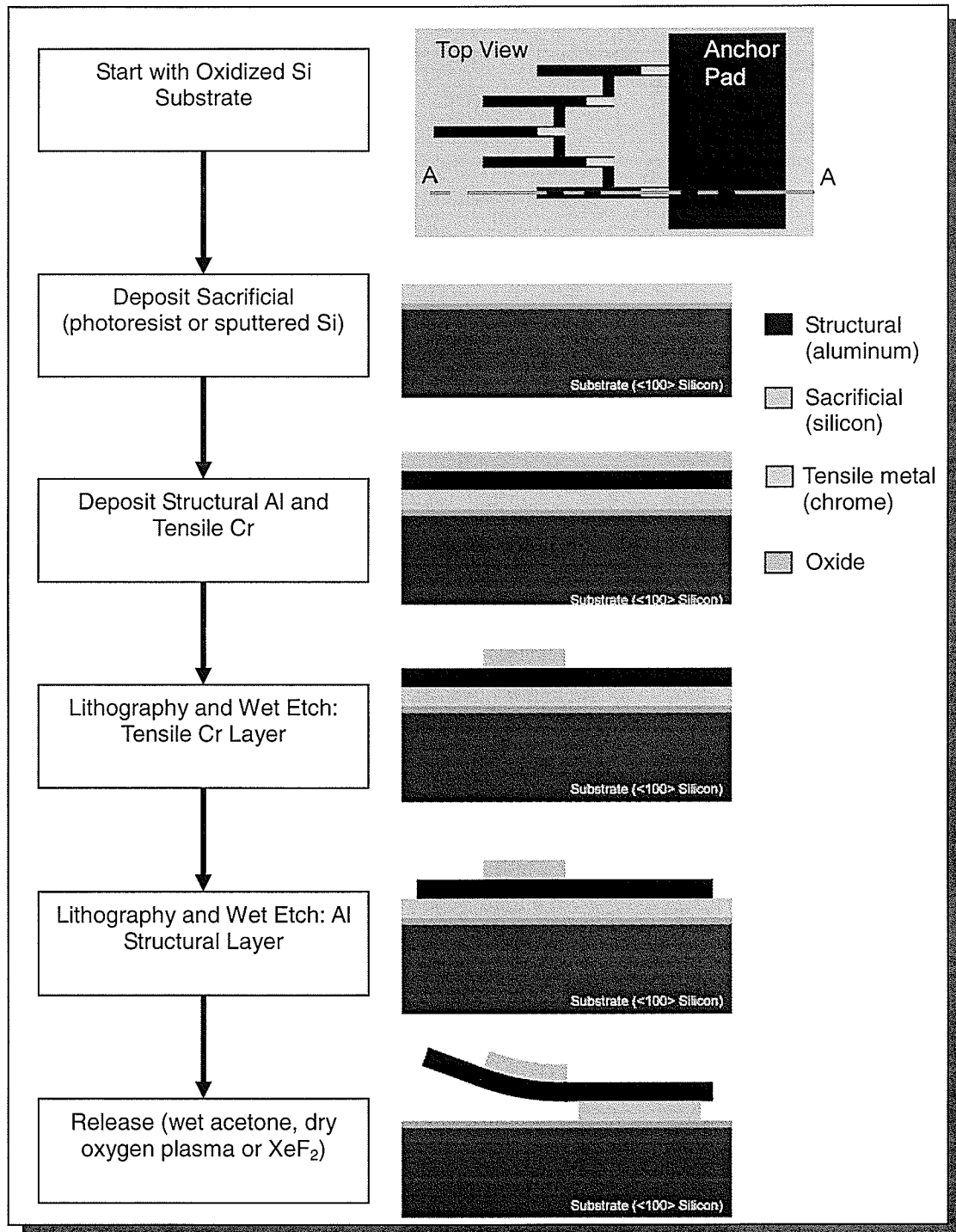


Fig. 3.4: Fabrication Sequence of the Cascaded Electrostatic Curled Cantilevers (not to scale).

3.3.3 Test Results

By completing successful fabrications of the same devices as Yasuda's work using

our own set of equipments and processes, we have established a reliable set of processes which we can employ for future devices of similar nature, namely the bimetallic cantilevers. A representative photograph of two successfully fabricated cascaded cantilevers and a device suffering stiction is shown in Fig. 3.5. The white areas in the figure are the structural aluminum which lie flat to the substrate. The devices which appear to be black are the successfully released ones which do not reflect light back at the microscope camera. From Fig. 3.5, we can clearly see the light gray chrome tensile layer at the base of the cantilevers. The increasing height with each cascading level of cantilever can also be seen, indicating a well behaved bimorph structure. The top device shown had all three cascaded cantilevers covered with Cr, whereas the bottom device had only two levels of curled cantilevers and a straight last section. This is observed via the difference in rest height of the third segment.

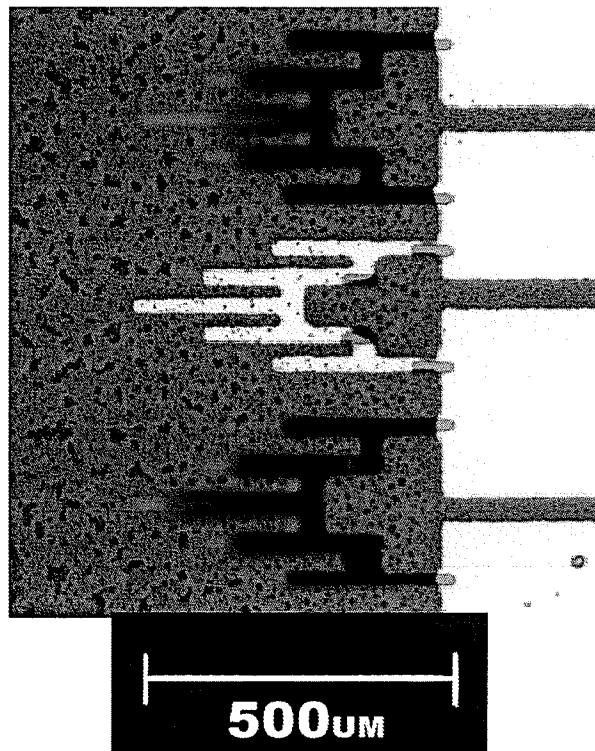


Fig. 3.5: Picture of three curled cantilever switches.

A basic actuation test was performed on a device with $28\mu\text{m}$ wide individual cantilevers, each $120\mu\text{m}$ long with $50\mu\text{m}$ of Cr covered section. These devices showed individual cantilever tip deflections of $58\mu\text{m}$, with an overall tip deflection over 3 cascaded levels of $200\mu\text{m}$. The required snap-down voltage in this device was $45\text{V} \sim 50\text{V}$. More importantly, these basic tests show that this set of fabrication processes are in par with expectations for bimetallic devices.

On the down side, the biggest problem encountered with the cascaded cantilevers was post-release stiction. The majority of stictions occur during actuation of the devices, when the contact area with the insulating oxide is at its maximum. The main reason which leads to this problem stems from its very own design. The cascaded cantilevers are, by design, relatively low in spring constant. Thus, it is not surprising that almost all of the devices did not recover after only a few actuation cycles. In conclusion, the severe stiction problems for the low restoration force devices limit their practicality as a large deflection switch despite the advantages it offers.

3.4 Curved electrostatic cantilever with stopper

An application stemming from Yasuda's work on the electrostatic bimorph cantilevers was a large-deflection optical ON-OFF switch studied by Chen et al. [10]. In this device shown in Fig. 3.6a, a single large deflection cantilever which also curved out of plane due to residue film stresses was used as the actuator. As mentioned before, a single curved electrostatic actuator with large deflection would usually require a large actuation voltage. In order to minimize this problem, Chen et al. incorporated substantially sized electrodes in a lengthy cantilever (1.5mm long) to achieve a relatively

low actuation voltage of around 20V for a tip deflection of $300\mu\text{m}$.

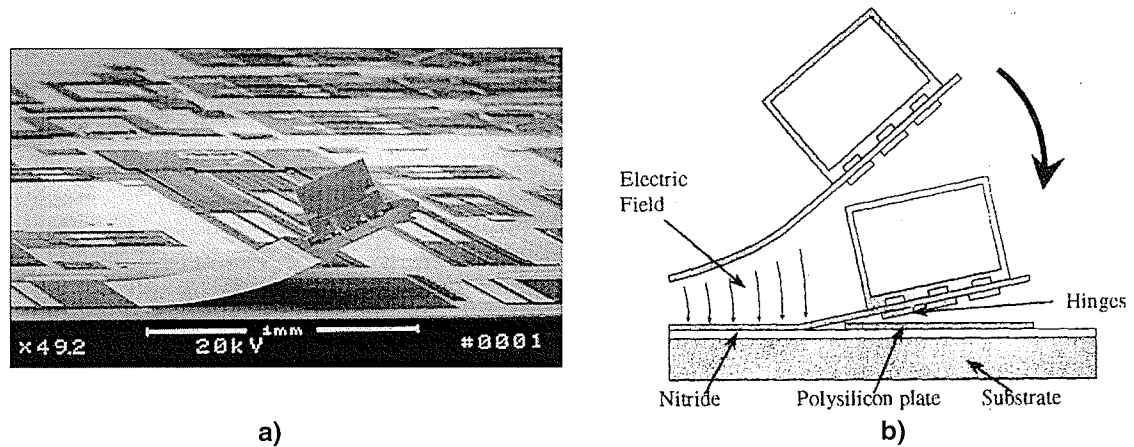


Fig. 3.6: (a) Single large-deflection curved cantilever used as optical switch by Chen et al. (b) Illustration of actuation principle showing the polysilicon stopper plate concept (taken from [10]) © 1999 IEEE.

As we have learned from the cascaded electrostatic actuator experiments, contact adhesion for such a device would be enormous and disastrous for operating reliability. The distinguishing feature of Chen et al.'s device is the use of a "stopper" plate placed beneath the straight cantilever section. The addition of this layer prevents the straight portion of the cantilever from contacting the substrate upon snap down, as shown in Fig. 3.6b. As a result, the reduced contact area leads to a much more reliable actuator for a device its size.

The complete fabrication of Chen et al.'s device was rather demanding due to its application as an optical switch. By excluding the steps involved in optical switch fabrication, the relevant processing steps of these curved cantilevers employ a similar stressed-film idea to that used for the cascaded cantilevers.

3.5 Electromagnetic Actuation Theory

Electromagnetic actuation of MEMS devices can be done using Lorentz force. The principle of Lorentz force is that charged particles traveling through a length of conductor under a perpendicular magnetic field will experience a force. The Lorentz force \vec{f} experienced by the particle (and indirectly the conductor itself) can be calculated using the following equation relating the magnetic field flux density \vec{B} , current \vec{i} , and length L of the conductor [7].

$$\vec{f} = \vec{i} \times \vec{B}L \quad (3.1)$$

In micromachining terms, current traveling through a wire of length L in a magnetic field with flux density \vec{B} will experience a force given by the cross product of $\vec{B}L$ and \vec{i} . To illustrate, consider a wire suspended between two anchors with a magnetic field perpendicular to the wire as pictured in Fig. 3.7. When driven with a current as shown, the wire will deflect to the side from the resulting Lorentz force evenly loaded on the length of wire.

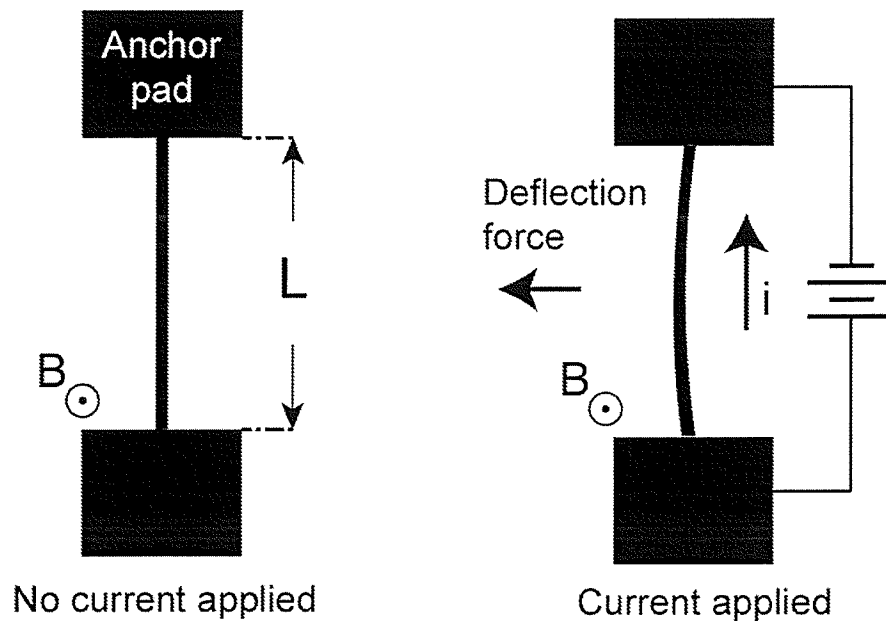


Fig. 3.7: Illustration of Lorentz force on a piece of suspended wire.

3.6 Integrated Coil Lorentz Cantilevers

Cho et al. have studied a surface micromachined cantilever switch with coils built into the top of the cantilever Fig. 3.8 [11]. The actuation principle in this device is Lorentz force, where the number of coils adds to the overall effect of the Lorentz force. The forces experienced by portions of the coil parallel to the cantilever's length are equal and opposite. The same case goes for the lengths of coil at the end and at the base of the cantilever; however the difference is that the base of the cantilever is fixed whereas the tip is free to move. Hence the overall effect of Lorentz force on the entire cantilever is due to the segment of the coil at the end of the cantilever and is in the z -direction, causing the cantilever tip to flex up or down depending on the direction of current travel. The tip of the cantilever has contact metal on the under side where it closes a circuit when actuated. An electrostatic holding electrode has also been incorporated into this design

to minimize its power requirements in the closed position. Since the deflection of the device is based on Lorentz forces (i.e. force is proportional to current), the voltage required to actuate the device across its entire range of motion can be made very small by using low electrical resistance coils. In short, such hybrid actuators offer both low-power and low-voltage characteristics with proper design.

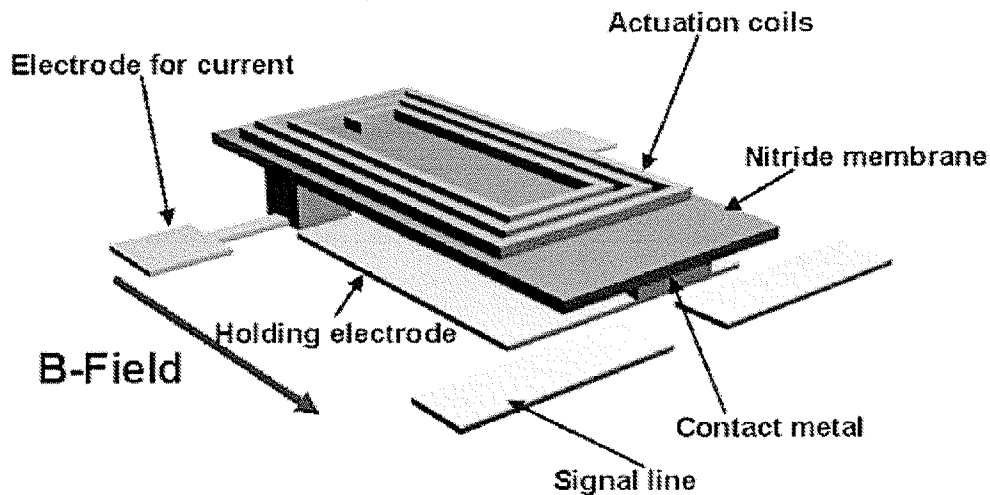


Fig. 3.8: Illustration of integrated coil cantilever actuator studied by Cho. et al. (image taken from [11]) © 2005 IEEE.

In the above switch for RF applications, they were also aiming for a large out-of-plane deflection. In their case, the largest deflection of $10\mu\text{m}$ was achieved using a thick sacrificial process. As mentioned before, thick sacrificial layers would mean that decent sidewall coverage deposition techniques are required. In order to extend this design to even larger out-of-plane deflections ($>100\mu\text{m}$) as required by this thesis, more advanced processing techniques would be needed on top of the already complex fabrication sequence (6 layers). Thus, this design is infeasible for deflections $>100\mu\text{m}$ within the constraints of this work.

Despite the unsuitability of this design to extend to even greater deflections, the

researchers have demonstrated many performance improvements of a ($10\mu\text{m}$) large-deflection MEMS device in RF switches. This illustrates the motivation of this thesis to achieve even larger deflections for such applications. From Cho et al.'s work, they have shown a hybrid actuator is possible, and such design is a well combination of Lorentz and electrostatic actuation for the amount of deflection in question.

3.7 Horseshoe Lorentz Force Actuators

The other Lorentz actuator with a large deflection reviewed for this thesis is the horseshoe shaped Lorentz force actuator [12, 18]. This device consisted simply of one conductive path anchored to two contact pads. The principle behind this design was that current traveling through the side arms of the structure will produce equal and opposite forces. Hence, the net force acting on the structure will be the result of the Lorentz force acting on the crossbar, as illustrated in Fig. 3.9. Once again the direction of tip travel is dependent on the direction of the current.

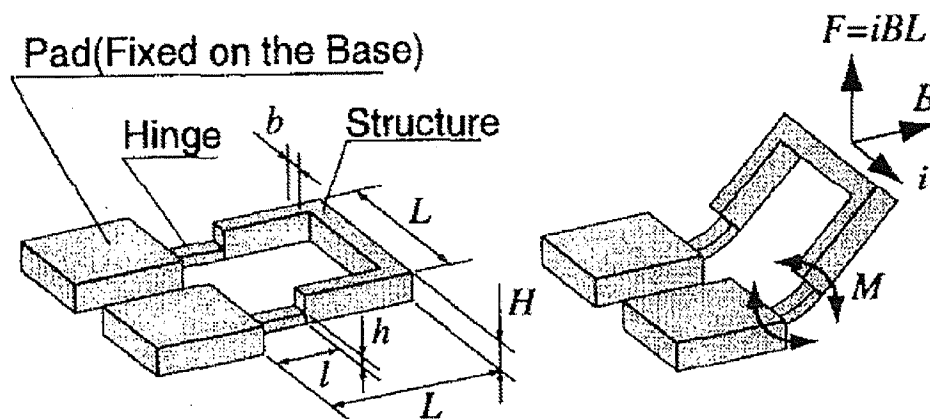


Fig. 3.9: Illustration of Shimoyama's Lorentz Actuator (taken from [18]) © 1998 IEEE.

Upon release, the device rests close to the surface of the substrate. The

researchers obtained a large initial height through plastic deformation of the structure at the hinges. This “bending process” was performed on a device to device basis by applying excessive upward actuation using Lorentz forces. This procedure is done in several successive stages, where the orientation of the magnetic field in each stage is slightly rotated in order to achieve large enough forces for plastic deformation to occur. The end result is a U-shaped structure which rests in a profile as shown in the right side illustration in Fig. 3.9. The device can then be actuated in either direction using the very same Lorentz force.

An advantage of this design is that large out-of-plane deflections can easily be achieved using conventional micromachining processes with low aspect ratios. These researchers have been able to achieve > 90 degrees of out-of-plane rest height of these U-shaped structures. The tip height of these actuators is then determined by the final rest angle and the length of the arms. Several tens of microns to few hundreds of microns deflection have been achieved using this setup. Low actuation voltage for this large deflection is also an advantage characteristic of most electromagnetic actuators. Furthermore, when compared to the coiled electromagnetic cantilever presented in section 3.5, the device design here is also considerably simpler. This is reflected in its significant reduction in fabrication requirements. This design requires just one conductive layer and a sacrificial layer using conventional low aspect ratio processes.

The disadvantage of these U-shaped actuators is that post-fabrication “adjustments” are required in order to achieve the desired large deflection. Moreover, this large deflection is not determined by device design, but by the actual process used to plastically deform the device hinges. This could lead to some inconsistency from device

to device, with the additional problem of increased metal fatigue at the hinges.

3.8 Chapter Summary

Two types of actuation principles were reviewed in this chapter as potential candidates for the proposed large-deflection actuator: electrostatic and electromagnetic. The electrostatic actuators achieved a large initial deflection via the use of residual film stresses. However, electrostatic actuation inherently disassociates large-deflection with low actuation voltages unless the structure is cascaded. Experimental work done in this thesis has shown that such cascaded devices were structurally soft (low spring constant and restoring force), leading to limited control of position under actuation. One way of minimizing such stiction is to limit the contact area to only the actuation electrodes, such as using a stopper layer underneath the cantilever. On the other hand, electromagnetic Lorentz force actuation allows large out-of-plane deflection with low actuation voltages in an external magnetic field. The problem with the presented U-shaped Lorentz actuators was that plastic deformation was required to obtain an initial rest height of the device, leading to the difficulty in a predetermined tip height. Previous work has demonstrated the feasibility of hybrid electromagnetic-electrostatic actuators and its well suited behavior for our design goals.

CHAPTER 4: LARGE-DEFLECTION LOW VOLTAGE ELECTROMAGNETIC ACTUATOR

4.1 Overview

In this chapter, we describe the design of an actuator that combines several advantages of the existing large-deflection devices. More specifically, the described device has been designed to provide low actuation voltage, deterministic large-deflection, low power, as well as low aspect ratio fabrication compatibility.

4.2 Introduction and Basic Design

The proposed design of the large-deflection actuator in this thesis is based on the Lorentz force actuator discussed in section 3.7. A representative structure of the basic Lorentz force U-shaped actuator is shown in Fig. 4.1. The main difference between this actuator and the one presented earlier in section 3.7 is that this design incorporates the residual film stress technique in which the two arms are partially covered with tensile chrome. As a result, the arms have a curvature wherever chrome metal is present. This eliminates the post-fabrication steps required to obtain a large out-of-plane deflection for the device in section 3.7. These arms are linked at the end via a crossbar. When current is applied through the U structure, the Lorentz forces felt by the arms of the U structure are equal and opposite regardless of the curvature. Thus, the net force experienced by the structure is the force on the crossbar in the z-direction causing the tip of the device to deflect up or down, depending on the direction of current travel.

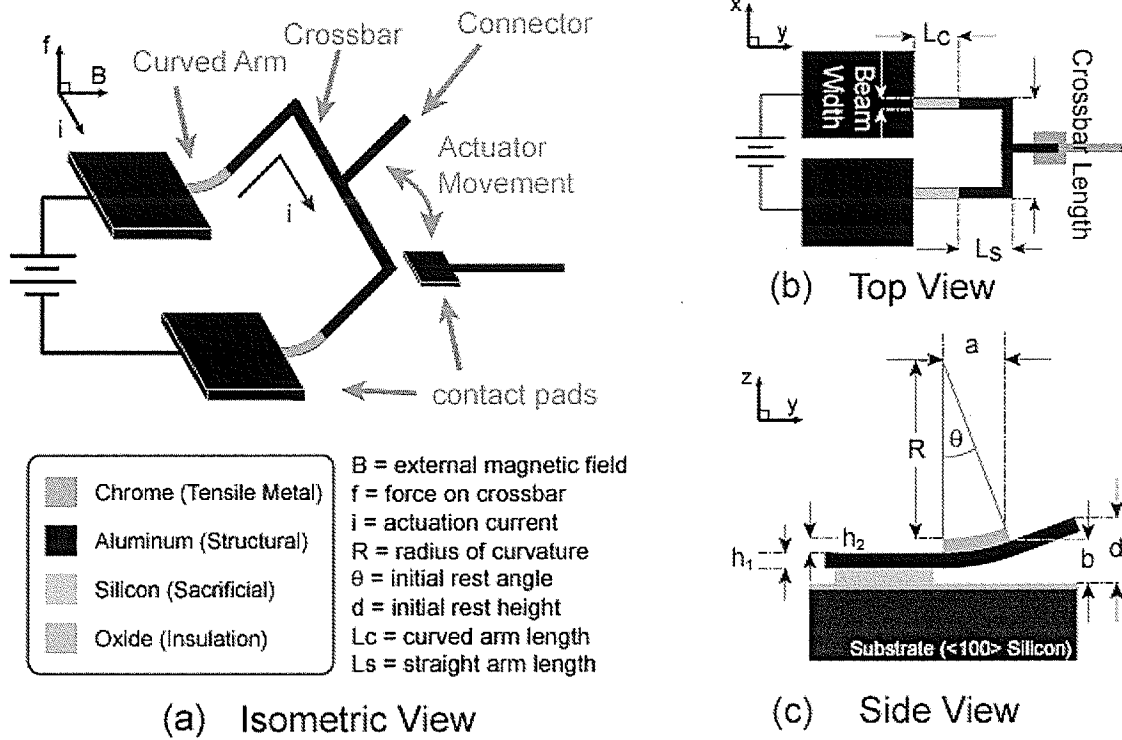


Fig. 4.1: a) Illustration of Lorentz force actuators, showing orientation of force, magnetic field, and current b) top view showing device design dimensions c) side view showing released curved cantilever and measurements.

A practical advantage of the Lorentz actuator is its ability to reverse directions by reversing the applied current. Since stiction is often a serious problem for these relatively soft, large-deflection devices, being able to reverse the actuation direction allows the device to be actively “un-stuck” in the event of a minor stiction. Because of the initial rest height of the device, we can swing the structure both forward and reverse for added displacement range if desired.

The advantage of low-voltage actuation in Lorentz actuators is also part of the device design. This means that these actuators can be incorporated with, for example, CMOS electronics for ease of system integration.

In order to function as a switch, the basic Lorentz actuator was fitted with a metal

connector in the middle of the crossbar as the switch element. This forms the basic design of the Lorentz switch with curled arms as shown in Fig. 4.1a. The addition of the connector also allows us to use it as the electrostatic holding electrode for hybrid actuation that minimizes the power consumption in the closed position similar to the device in section 3.6 [11]. The way this hybrid scheme works is by first actuating the switch through its entire range using the Lorentz force such that the connector tip is brought very close to the bottom electrode. Then, by applying an electrostatic holding voltage across the connector and the bottom electrode, the switch is held closed with minimal power.

At first glance, this device might not seem all that much different from the existing horseshoe device studied by Shimoyama et al. in section 3.7. But the impact on device performance from the addition of a residual stress layer will be more apparent as the simulations results are presented in the later section. Further discussion on the advantages of this device will be continued as the results are presented.

4.3 Fabrication

Fabrication sequence of the proposed Lorentz actuators is very similar to that of the curled cantilevers. The difference between the two is the addition of a bottom metal layer to be used for contact pads/electrostatic holding electrode beneath the connector. The material used for this bottom layer was sputtered aluminum 300nm thick, and later etched using standard wet phosphoric acid solution as described in section 2.7. The remaining steps involve sputtering of the silicon sacrificial (400nm), thermal evaporation of the structural Al and tensile Cr layers (0.7 μ m and 70nm, respectively), followed by

patterning of the tensile and structural layers, and finally the XeF_2 etch release. For details regarding these individual processes, refer to Chapter 2. The optional plasma etch of silicon sacrificial prior to XeF_2 release was also performed on the Lorentz actuators to save time. The complete fabrication sequence is shown in Fig. 4.2.

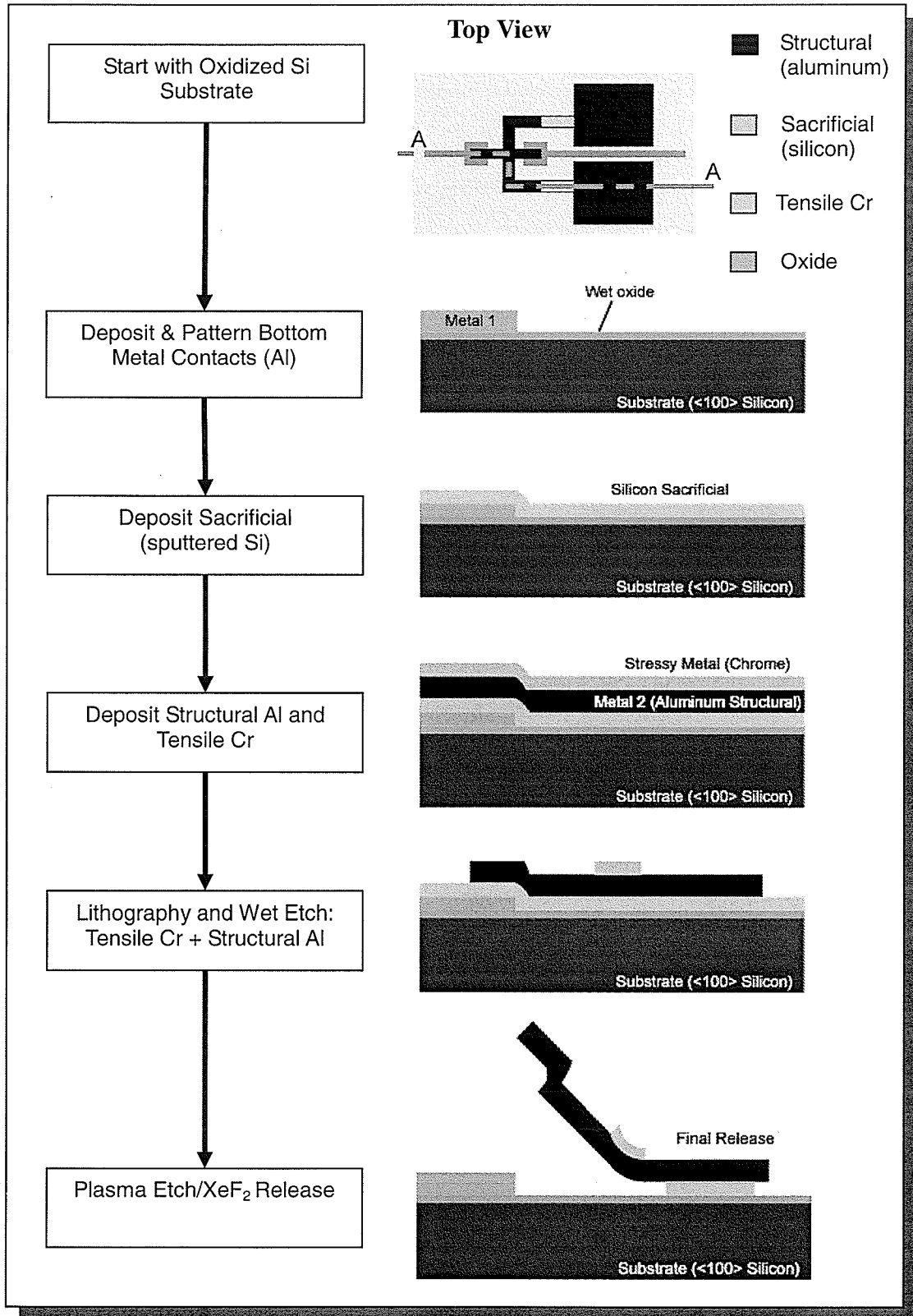


Fig. 4.2: Fabrication sequence of the Lorentz switches (not to scale).

4.5 Finite Element Modeling

4.5.1 Stress Analysis

The COMSOL Multiphysics 3.2 software package was used to model the Lorentz actuators with respect to stress in the chrome layer and Lorentz actuation force. The 3D finite element model (FEM) was created in the MEMS module of the software package, and analyzed using solid stress-strain physics. Table 4.1 lists some basic properties of the model. The basic model shown in Fig. 4.3a illustrates a device at rest with out-of-plane deflection due to residue stress, and Fig. 4.3b shows the mesh used in the model. For complete and detailed information on the model, refer to Appendix B1.

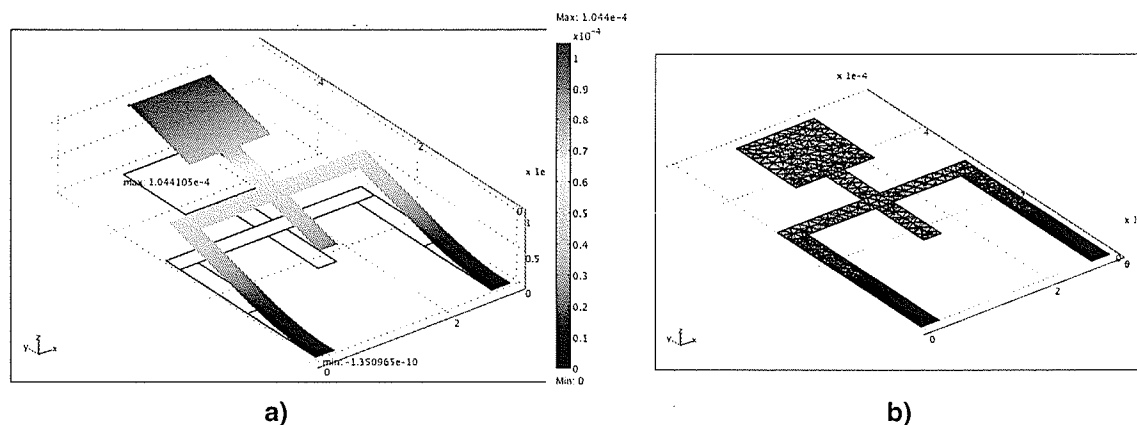


Fig. 4.3: (a) Basic model showing device at rest out-of-plane due to residue stress. (b) Mesh structure used for FEM analysis.

TABLE 4.1: BASIC PARAMETERS OF THE FEM MODEL

| Parameter | Value | Parameter | Value |
|------------------|-------------------|---|-------------------|
| Arm Length | 300 μm | Structural Metal | Al |
| Arm Width | 28 μm | Structural Thickness | 0.7 μm |
| Crossbar Length | 300 μm | Structural Stress σ_{Al} | 0 GPa |
| Crossbar Width | 28 μm | Tensile Metal | Cr |
| Connector Length | 200 μm | Tensile Metal Thickness | 0.1 μm |
| Connector Width | 28 μm | Tensile Metal Coverage | 136 μm |
| | | Tensile Metal Stress σ_{Cr} | 0.45 GPa |

The first part of the FEM analysis studied the deflection of the device as a function of the tensile stress in the Cr layer for the basic Lorentz switch shown in Fig. 4.3. For simplicity, the stress in the structural Al layer σ_{Al} was assumed to be zero. The validity of this assumption is confirmed with empirical observations that the Al films used in this work by themselves showed very low-levels of out-of-plane bending, indicative of low levels of stress.

From the stress theory presented in section 2.4, the radius of curvature of a bimetallic structure decreases with increasing tensile stress in the Cr layer. In other words, the curvature becomes more pronounced with higher stress σ_{Cr} , which leads to an increase in tip height. In Fig. 4.4a, the initial deflection of the connector tip is plotted versus stress in the Cr layer for the simulation result. This shows an increasing trend as expected according to equation 2.2.

The cross sectional profile of the arm in Fig. 4.4b shows well-behaved bimetallic structures with curved sections wherever Cr is present. The profiles for multiple stress

values were plotted in the same figure to also show the decreasing radius of curvature as σ_{Cr} increases. From these results, we can approximate the actual stress in the tensile Cr layer of the fabricated device by matching actual and simulated deflections of the arm. Foreshadowing the actual tip height measurement of a fabricated device with identical dimensions, the stress value which matches the measured $107\mu\text{m}$ tip height is approximately 0.45GPa , where the simulated result showed a tip height of $104\mu\text{m}$. For the simulations in the next section, the stress value was fixed at 0.45GPa .

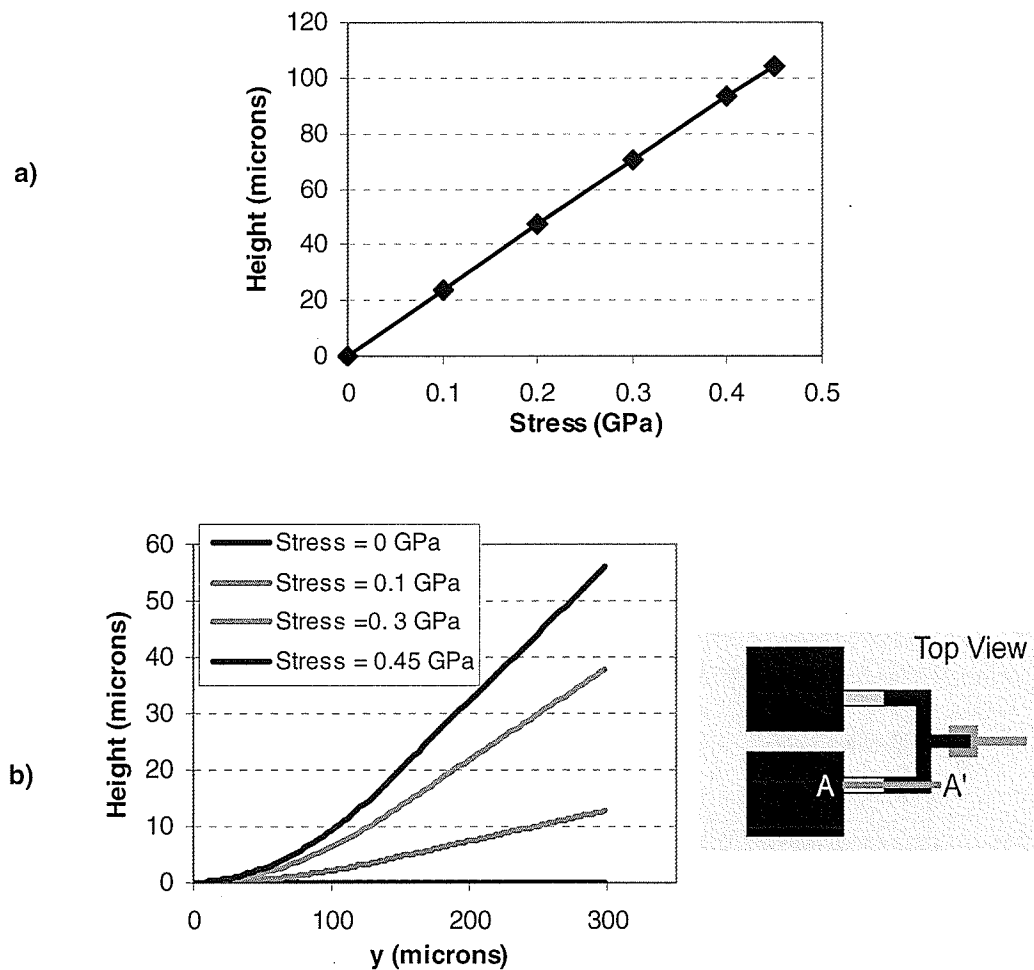


Fig. 4.4: (a) Connector tip height versus stress in simulated results. (b) Profile of one of the arms along its length for different stress levels, showing curvature where Cr is present ($136\mu\text{m}$ length) and straight sections everywhere else ($164\mu\text{m}$).

4.5.2 Actuation Analysis

The second part of the FEM analysis involved the application of Lorentz forces to the structure above with an initial deflection due to stress and strain. In order to truly simulate the effects of electromagnetic force interaction with the stress and strain simulation, several physics packages in COMSOL were required to be solved simultaneously. However, from the theory presented in section 3.5, it is a good approximation that the bulk effect of the Lorentz forces on the structure would be a force acting on the crossbar in the z-direction. Therefore, the model can be simplified by approximating the Lorentz force with a constant force per unit area f_L on the top face of the crossbar in the z direction. This simplification would allow the model to be solved using just one physics package, which shortens the solving time of the model tremendously. From this point on, let $f_L > 0$ be in the direction where the force is directed towards the substrate.

Actuation analysis was performed on the simulated results from the previous section using $\sigma_{Cr} = 0.45\text{GPa}$. The crossbar was loaded with forces for $f_L = 0 \sim 160\text{N/m}^2$, and the results are plotted in Fig. 4.5. Fig. 4.5a shows the tip height d of the connector versus applied force, where we observe a linear relationship from the initial resting position ($f_L = 0\text{N/m}^2$, $d = 107\mu\text{m}$) to the position where the tip touches the surface ($f_L = 160\text{N/m}^2$, $d = 0\mu\text{m}$). The fact that this motion is near linear through the entire movement range of the device is a desirable feature for applications which require analog control over the tip position. On the other hand, the cross sectional plot of the arm along its length in Fig. 4.5b shows an interesting arm profile. As f_L increases, the profile of the arm increasingly resembles a dome structure because of two forces. The bimetal at

the base of the arm causes the arm to elevate above the surface, whereas the net Lorentz force concentrated at the end of the arm pushes it towards the surface. Thus, the overall effect is curvature along the length of the arm under actuation. The shape and degree of this curvature when the actuator is under full actuation is determined by the length of C_r at the base of the arm. Further simulations of the same device with different C_r lengths allow us to plot the arm profiles in Fig. 4.6a. This plot shows the change in dome structure as the lengths of C_r varied. Note that the fully C_r -covered arms cease to exhibit the dome profile under actuation.

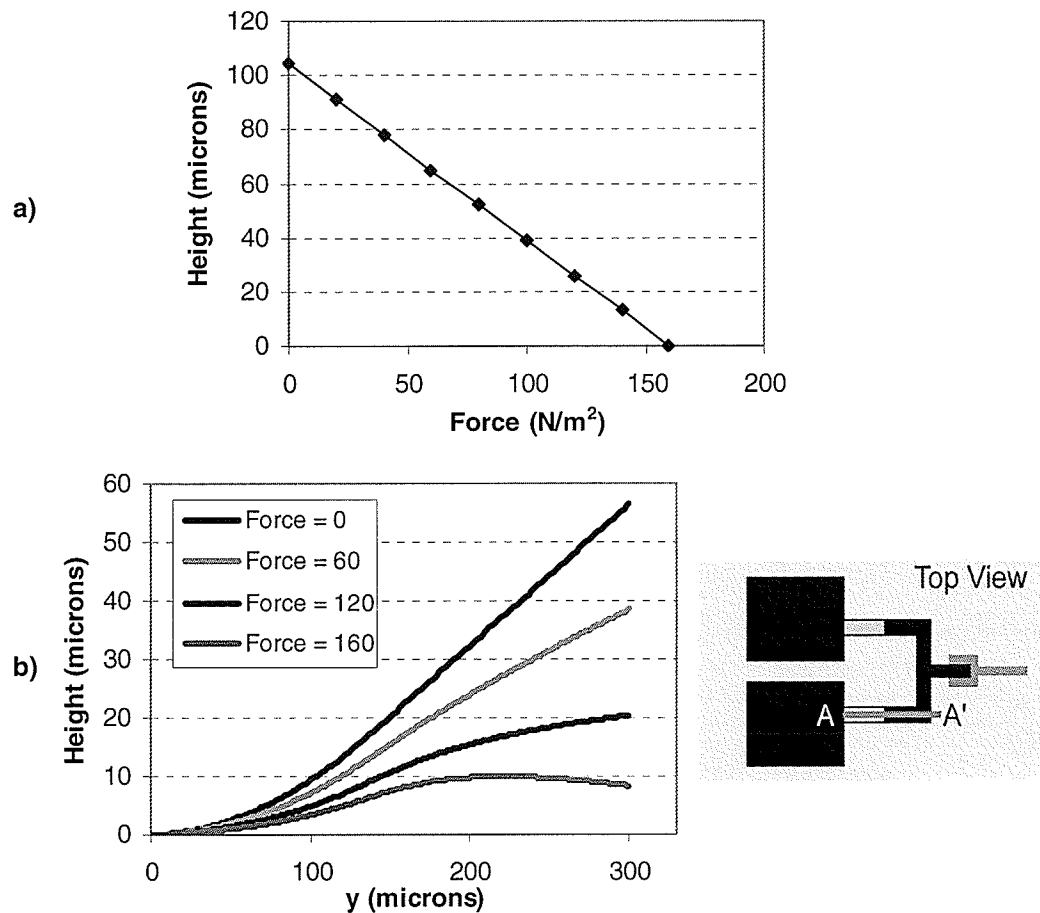


Fig. 4.5: (a) Connector tip height versus actuation force per area f_L . (b) Arm profiles for increasing actuation forces (in N/m^2), showing the increasing domed profile.

In addition to the arm curvature, the profile of the crossbar along its length also shows increasing bowing under actuation. This bowing is a combined result of the distributed downward Lorentz force on the crossbar and the upward restoring force of the arms concentrated at the two ends of the crossbar. The curvatures of the arms and the crossbar are best illustrated in an exaggerated plot of the device at touch down in Fig. 4.6b, where the color legend shows height. The significant implication of these two characteristics of the actuator is that the portion of the entire switch which “touches down” first is the tip of the connector, which was positioned there for the main purpose of a good metal-to-metal contact. Hence, a significant advantage of this actuator design for MEMS is that it minimizes the unnecessary contact of any non-switching part of the actuator, thus reducing the possibility of stiction at these areas. For a device with low restoration forces, this is a valuable feature which improves device reliability under actuation.

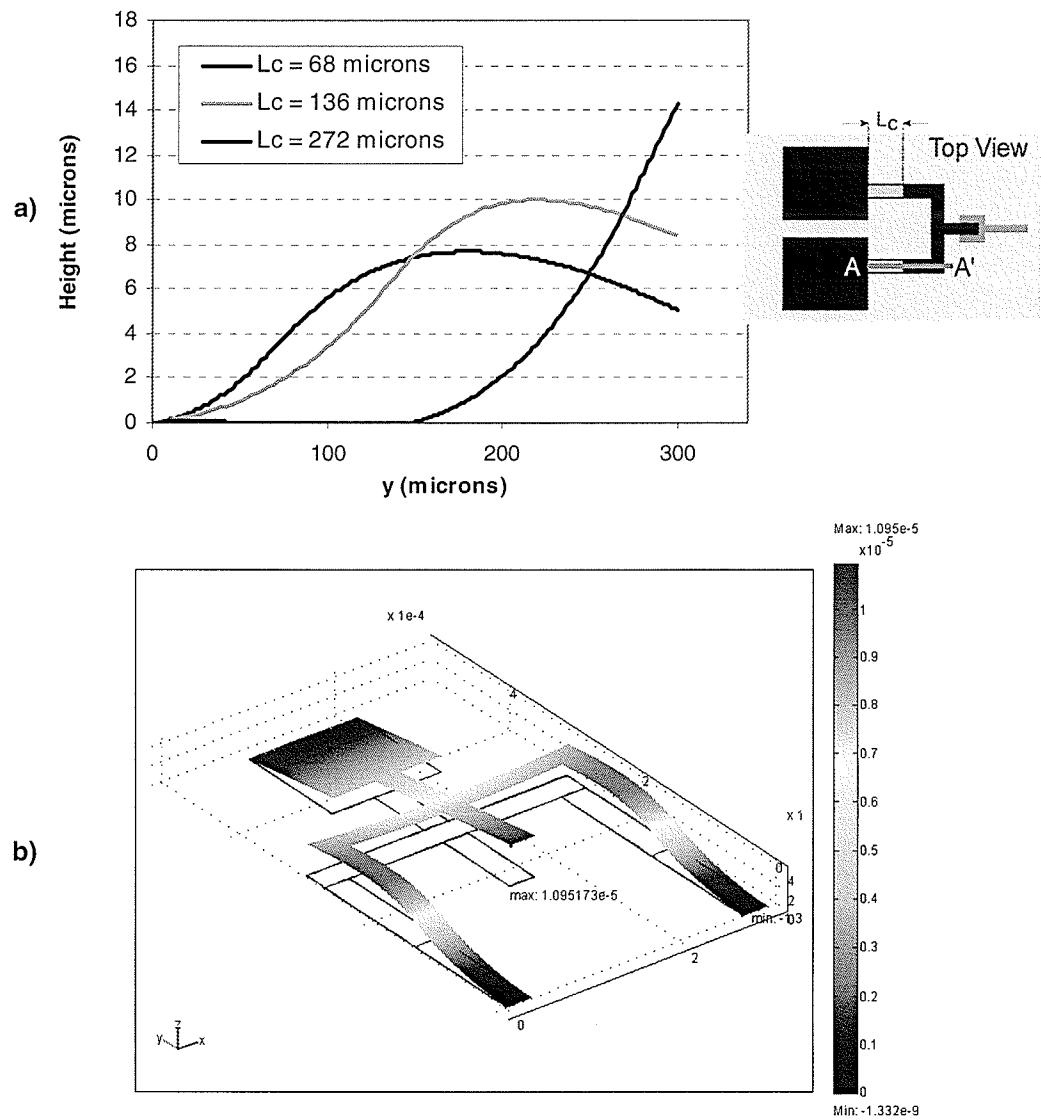


Fig. 4.6: (a) Change in dome profile when tip is touched down for different Cr lengths. (b) Exaggerated (5x) snapshot of the simulated device at touchdown position, showing both the curvatures of the arm and crossbar.

In addition to the reduced stiction-prone surface area, another advantage of this bimetallic actuator is the ability for it to be a tri-state switch. The first state is shown in Fig. 4.6b, where the outer connector tip is held down. The second state is its resting state, shown in Fig. 4.3a, where the bottom connector can be in contact with another bottom metal layer positioned between the arms of the device. In order to make contact

in this state, the length and resting angle of the bottom connector needs to be designed accordingly. The actuator can also be in a third state where neither ends are making contact, thus making this device a tri-state switch. This behavior can be illustrated with the plot of connector tip angle versus actuation force in Fig. 4.7, where the zero degree plane is parallel to the substrate.

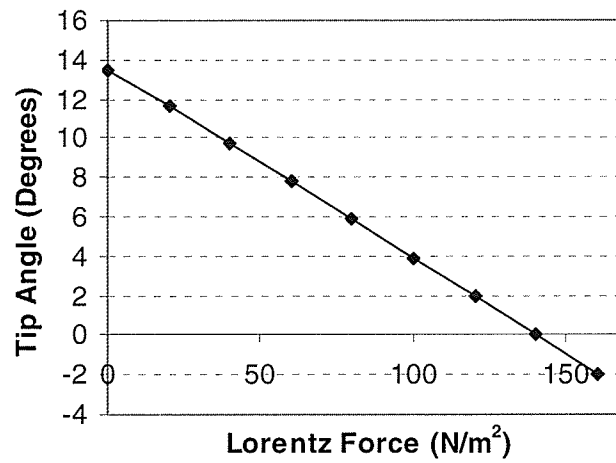


Fig. 4.7: Connector tip angle as a function of applied force.

4.7 Joule Heating Effects

A factor that was not taken into account in the above FEM analysis is the Joule heating effect of the structure itself from the actuation current. This increase in temperature at the arms and crossbar is especially important to the bimetallic structure, because mismatch in thermal expansion coefficients between the aluminum and chrome layers will cause additional change in stress. This differential thermal stress in turn causes the cantilever to deflect up or down, and affects the overall accuracy of the Lorentz only FEM analysis in the previous section. This effect has been studied in more detail in a previous work that utilized very similar Lorentz actuators to make

micro-mirrors by J. Johnson [4]. From his work, it was clear that the effects of thermal expansion are insignificant in the range of operation (less than 5% of the overall deflection within 30mA of actuation). Thus, the rest of this work will leave out the effects of thermal expansion for simplicity in the analysis. For more information, see Appendix D: Heat Analysis of the Basic Actuators.

4.8 Chapter Summary

The design and extensive FEM characterization of a large-deflection low-voltage MEM actuator based on a “U shaped” conductor was presented in this chapter. This design incorporated features from several existing devices capable of large out-of-plane deflection, such as residual film stresses, to give Lorentz actuators a large but well defined initial deflection as required by this thesis. In addition, the linear motion of the device tip across the entire range of actuation was also revealed by FEM simulations. The simulation results also show some of the actuator’s unique characteristics under actuation. As the actuator tip is actuated to the touch-down position, the arms of the device exhibit an increasing domed profile. At the same time, the crossbar of the device exhibits increasing bowing due to the distributed Lorentz force. These two unique characteristics have allowed the tip of the connector in this design to be the only portion in the entire device to make contact with a bottom contact pad under actuation. In other words, the design of the proposed actuator minimizes the chances for stiction to occur in the device by minimizing any unnecessary contact with the substrate. This desirable attribute was not present in the existing design reviewed in this thesis. Another significant characteristic of the proposed design is the ability to function as a tri-state

switch. In summary, simulation results in this chapter show that the goals of this thesis can be achieved with the proposed design, pending verification of its behavior with testing of the actual fabricated devices.

CHAPTER 5: ROTATIONALLY CORRECTED ELECTROMAGNETIC ACTUATOR

5.1 Overview

In addition to the basic proposed design in Chapter 4, we further present a rotationally corrected (RC) design as an extension to the U-shaped Lorentz actuators. This novel electromagnetic and electrostatic hybrid actuator is designed to have large deflections while allowing the tilt/position of the tip to be corrected at a much finer scale. The simulation results of this advanced design that are presented in this chapter will provide a good view of its unique characteristics and advantages.

5.2 Introduction and Design

The rotationally corrected Lorentz actuator was designed with a different purpose from the basic U-shaped Lorentz actuator in Chapter 4 in mind. While the basic actuator was designed with the primary purpose of large-deflection, the rotationally corrected actuator was designed to include versatility to go with that large deflection. The concept behind the rotationally corrected actuator, shown in Fig. 5.1, is to have a smaller U-shaped Lorentz force actuator, located within the primary actuator, and coupled to the crossbar of the primary actuator. Since the outside crossbar is longer than the inside crossbar, it experiences a greater Lorentz force under the same current and magnetic field. Applying current to the outer arm would then result in the large-deflection movement of the actuator. Similarly, applying current to the inside arm results in force of a lesser

magnitude which primarily changes the tilt of the connector. Thus, the actuator is capable of large deflections while preserving the ability to correct its position and angle at a finer scale with separate drive signals.

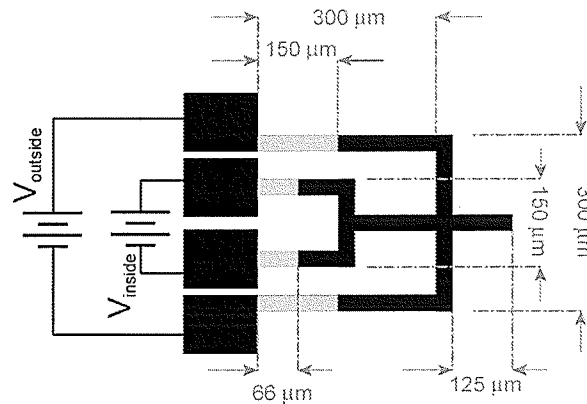


Fig. 5.1: Rotationally corrected Lorentz actuator showing simulated dimensions.

The rest of this design shares many similar advantages with the basic actuator – deterministic large initial deflection from the bimetallic structure, conventional fabrication process, low-voltage actuation and bi-directional actuation. In fact, the rotationally corrected design can be fabricated using the exact same processes as the basic U-shaped actuator as presented in chapter 4. This design can also be an electrostatic-electromagnetic hybrid as well, where the tip is held down using electrostatic force after being brought into contact using Lorentz force.

The author would like to point out the fact that the outside actuator of this RC device has identical dimensions to that of the basic U shaped actuator in chapter 4. This would allow us to compare the RC device characteristics under actuation to that of the basic actuator.

Because of the increased complexity of the RC devices, throughout the rest of this thesis the term “device” will be used to refer to the rotationally corrected Lorentz actuator

as a whole. The terms “inside actuator” and “outside actuator” will be used to refer to one of the two U-shaped Lorentz actuators in the device. The terms “basic actuator” and “basic design” refer to the single U-shaped bimetallic actuator presented in chapter 4.

5.3 Finite Element Modeling: Rotationally Corrected Devices

5.3.1 Stress Analysis

The modeling process of the rotationally corrected device was very similar to that of the basic design. Once again the simulation had two parts: first the effect of tensile stress was simulated with respect to initial deflection, and second, the effects of Lorentz forces were simulated. The dimensions of the model are included in Fig. 5.1, and the model mesh used is shown in Fig. 5.2a. For complete details regarding the modeling setup, see Appendix B2.

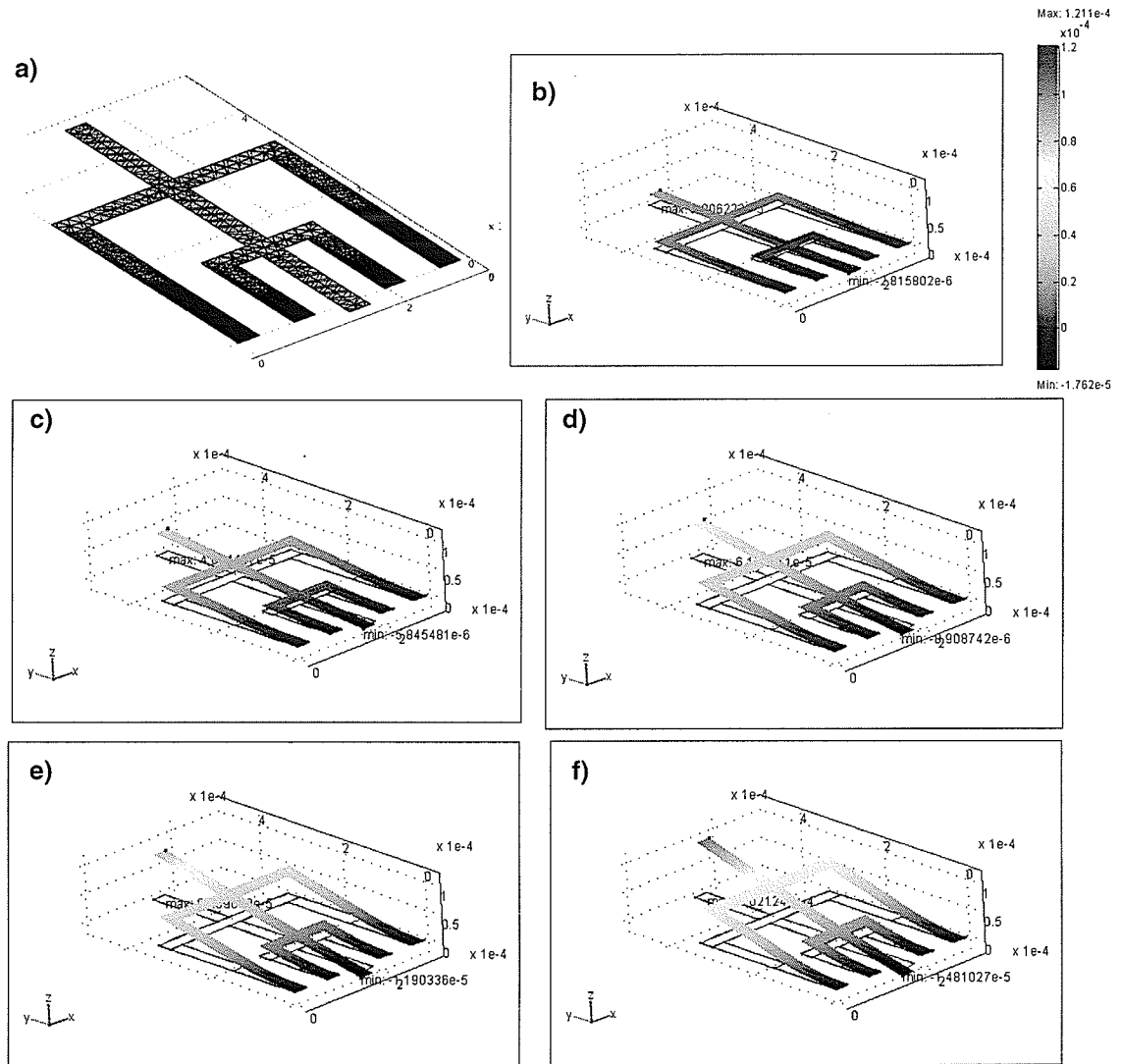


Fig. 5.2: (a) RC device model mesh. (b)~(f) Snapshots for stress values $\sigma_{Cr} = 1e8, 2e8, 3e8, 4e8, 5e8$ Pa, respectively, to show increasing arm curvature. Red= $121\mu\text{m}$ and dark blue= $0\mu\text{m}$.

In order to start examining the effects of increasing stress in the Cr layer, we simulated the basic model from $\sigma_{Cr} = 0\text{GPa}$ to 0.6GPa . The profiles of the structure as stress increases are progressively shown in Fig. 5.2b ~ 5.2f. These snapshots of the device are shown for representative stress values of 0.1GPa , 0.2GPa , 0.3GPa , 0.4GPa , and 0.5GPa . The color legend in the figure shows the height of the device at each location, with red corresponding to approximately $121\mu\text{m}$ and dark blue corresponding to

0 μ m. From these snapshots, we can clearly see the same increase in curvature in the Cr covered sections of the arm just like in the basic U device. The main point in this section of the simulation was just to verify the proper behavior of the model with regards to stress and strain. Furthermore, a rough indication of the stress level of the actual deposited film can be obtained by matching the measured tip height with the closest tip height in this set of simulations. In this case, stress level of $\sigma_{Cr} = 0.45\text{GPa}$ matches the actual results, and will be used as the basis for the actuation analysis in the next section.

It is also interesting to compare the connector tip height versus Cr stress plot of the RC device to that of the basic device in Fig. 5.3. Since the outside actuator of the RC device has identical dimensions as the basic device, their deflection curves are closely matched. The RC device deflects slightly less with stress only because its inside actuator was designed with less Cr coverage. In other words, the inside actuator is progressively exerting resistance as stress level increases due to its smaller angular deflection. Conversely, if the inside arm is designed with more Cr coverage, it would increase the deflection in a very similar fashion.

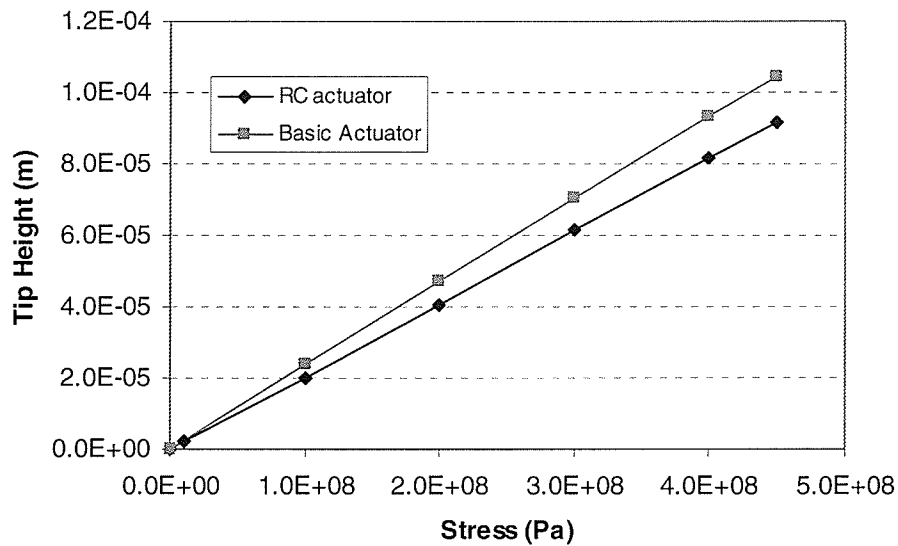


Fig. 5.3: Simulated tip height versus Cr stress for the RC device and the basic device.

5.3.2 Actuation Analysis

In the actuation analysis of the RC devices, the simulation was further divided into four cases:

- A. actuating the outside crossbar only ($f_{L-in} = 0$)
- B. actuating the inside crossbar only ($f_{L-out} = 0$)
- C. actuating both crossbars in the same direction ($f_{L-in}, f_{L-out} > 0$)
- D. actuating both crossbars in opposite directions ($f_{L-in} < 0, f_{L-out} > 0$)

where f_{L-in} is the force per unit area exerted on the inside crossbar, and f_{L-out} is the force per unit area exerted on the outside crossbar. The point of these four setups was to try and isolate the effects of each actuator, and to find out whether the nature of these individual effects changes when combined.

For case A, the movement of the connector tip as a result of actuating the outside crossbar only is plotted in Fig. 5.4. The plot shows a linear curve with a total vertical

range of $31 \mu\text{m}$ over 80 N/m^2 applied force ($-0.381 \mu\text{m}$ per N/m^2 applied). Compared to the basic U actuator, which displaced $52 \mu\text{m}$ over 80 N/m^2 ($-0.65 \mu\text{m}$ per N/m^2 applied), the double beam structure is significantly stiffer. This is not surprising since there is now an extra set of arms holding onto the connector. Although this means that more drive current will be required to move the RC actuators for a given distance, the device is still capable of a large deflection range given enough applied current within its current carrying limit.

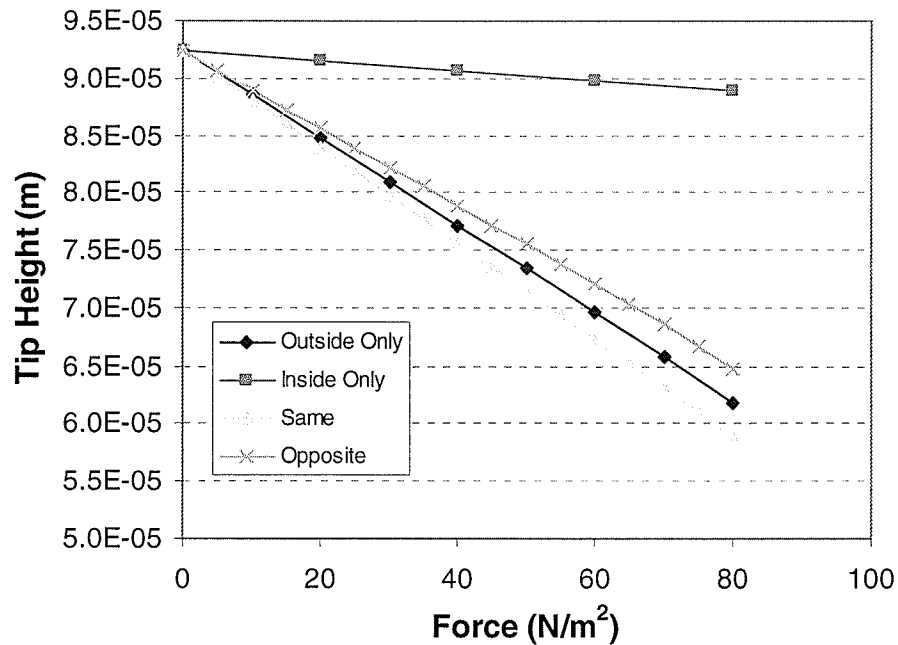


Fig. 5.4: Plot of simulated tip height vs Lorentz force for four actuation cases. The direction of the outside arm is kept the same while the inside arm switches for the cases when both arms are actuated simultaneously.

For case B, the tip deflection versus applied force to the inside crossbar is also plotted in Fig. 5.4. Once again we observe a linear curve, only this time a much lesser range of only $3.5 \mu\text{m}$ over 80 N/m^2 of applied force is observed ($-0.043 \mu\text{m}$ per N/m^2 applied). This agrees with our expected result of a “fine-tuning” inside arm.

Cases C and D explore whether the fine-tune ability was affected by actuation of the outside actuator. Therefore, the outside and inside actuators were simultaneously loaded with forces, either in the same direction (case C) or opposite direction (case D). For ease of comparison, the direction of outside actuation was kept the same while the inside actuation switches directions. In both cases, the forces per unit area on both crossbars are equal (i.e. $f_{L-in} = f_{L-out}$).

The results shown in Fig. 5.4 are promising. In case C, when the two arms are actuated in the same direction, we observe a range of $34\mu\text{m}$ over the same 80N/m^2 range, or a slope of $-0.420\mu\text{m}$ per N/m^2 applied. This slope is almost equal to the sum of the individual actuation in cases A ($-0.381\mu\text{m}$ per N/m^2 applied) and B ($-0.043\mu\text{m}$ per N/m^2 applied). On the other hand, in case D, we observe a range of $28\mu\text{m}$ over 80N/m^2 . The slope here is $-0.344\mu\text{m}$ per N/m^2 applied, which is almost equal to the difference of slope between Cases A and B. From these results, it would suggest that the effects of these two actuators on tip height are almost independent of each other in the range studied.

The ratio of the slopes of the outside to the inside actuation is about an order of magnitude, specifically $-0.381/-0.043 = 8.8$. To first order, this ratio depends on the relative lengths of the crossbars because of the Lorentz force's direct dependence on crossbar length. The longer the inside crossbar is relative to the outside crossbar, the closer the ratio is to 1. Conversely, the shorter the inside crossbar relative to the outside, the larger the ratio will be. Unfortunately, the ratio also depends on other design factors such as the length of connector between the crossbars, the lengths of the arms, and even the lengths of Cr, etc. The exact characterization of this relationship is definitely an

interesting study. However, a detailed analysis is beyond the scope of this thesis.

5.3.3 Advanced Actuation Analysis

To show that the determination of slope ratio of the two actuators is not a trivial one, another set of simulations is done on another RC actuator. The dimensions of this second device are such that the ratio of the lengths of the crossbars is kept approximately the same, but both crossbars are twice as long. The dimensions of the wider device are shown in Fig. 5.5a. All arms and crossbars in this device have a width of $50\mu\text{m}$.

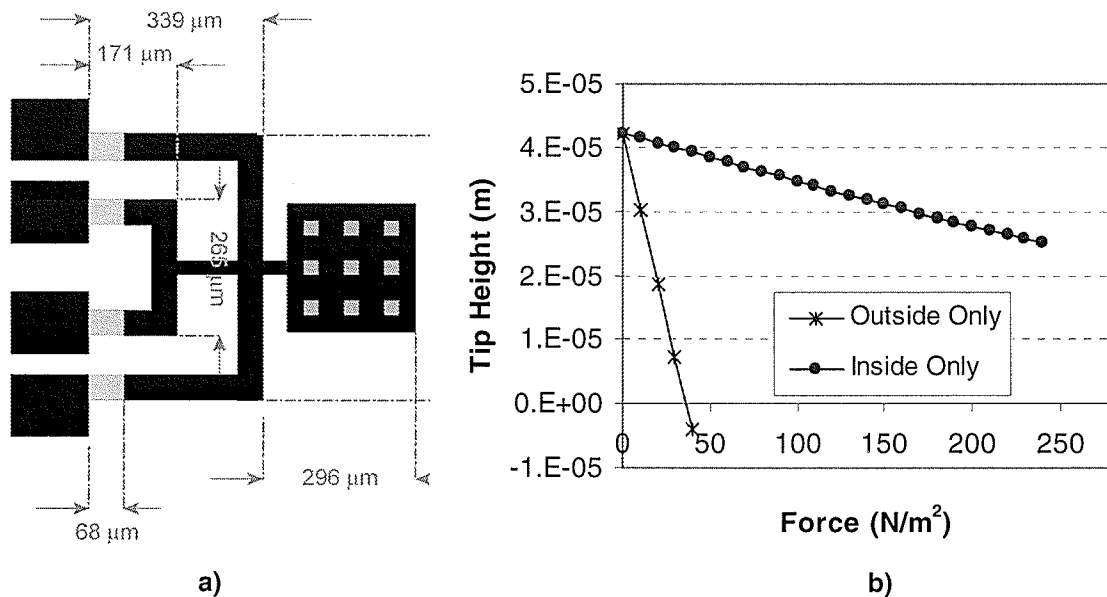


Fig. 5.5: (a) dimensions of a second RC device with wider overall crossbars. (b) Simulated tip height vs force for the two actuators.

The results from subjecting the wider RC device to individual actuation of the actuators are shown in Fig. 5.5b. The first thing we notice is the increase in slope as a result of overall wider crossbars. For case A, the tip showed $46\mu\text{m}$ of range over 40N/m^2 , whereas in case B the range was $2.9\mu\text{m}$ over 40N/m^2 . Despite the same ratio in

the outside to inside crossbar lengths, the slope contrast ratio in the wider device is much higher ($46/2.9 = 15.9$ - much higher than the 8.8 in the previous RC device). This confirms that the slope contrast ratio is not a simple function of the lengths of the crossbars.

Another reason that we have presented a second RC device of different dimensions was to illustrate the full advantage of the bi-directionality of Lorentz actuation. The wider RC actuator was designed with half as much chrome length on the arms. This has led to a smaller initial resting tip height of $42\mu\text{m}$, which is somewhat in the middle of the $0\sim 100\mu\text{m}$ range. By actuating the outside arm in the positive z -direction, we can achieve the required large deflection of $100\mu\text{m}$. By the same token, we can switch the tip of the device down by actuating in the opposite direction. The advantage gained here is two fold: half as much actuation (current) required for the same overall range and actuation symmetry in the range of interest. The trade off made here is that we now require constant actuation (power) to hold the tip in positions higher than the initial resting height.

One important aspect of the RC devices with respect to the individual actuation of the arms is also revealed in the tip height versus actuation plot of Fig. 5.6a. For the outside actuator curve, we see that this function is essentially linear in the range of interest. A similar curve is observed for the inside arm actuation, just like we have already seen for the first RC device. If we now fix f_{L-out} to an arbitrary non-zero value ($+20\text{N/m}^2$ and -20N/m^2 in this case), and then vary f_{L-in} , we obtain the extension curves shown in green and yellow. The force axis for these two curves has been offset from the 0N/m^2 axis by $+20\text{N/m}^2$ and -20N/m^2 respectively for more intuitive illustration.

Immediately, comparing these two offset curves to the original inside arm actuation curve, we observe a flattening out behavior at higher actuation forces (e.g. $>150\text{N/m}^2$). This phenomenon is due to the bending of the connector when the net forces exerted on the top and bottom crossbars are not equal. In other words, at the point where $f_{L-out} = +20\text{N/m}^2$ and $f_{L-in} = 0\text{N/m}^2$, clockwise torque is exerted along the connector length in Fig. 5.6b. The location of this “kink” in the profile (located at about $y = 171\mu\text{m}$) coincides with the attachment point of the lower crossbar to the connector. We can also see that as f_{L-in} increases, the degree of bend in the connector decreases. This change in connector angle is ultimately reflected in the tip height by the flattening out behavior we observed in Fig. 5.6a. An almost identical behavior is also observed for the case when $f_{L-out} = -20\text{N/m}^2$ and $f_{L-in} = \{0\text{N/m}^2 \sim -240\text{N/m}^2\}$.

The point being made here is that the fine tuning characteristics provided by the inside actuator are affected by the position of the outside actuator. For small actuation forces such as the range studied for the first RC device, little effect is observed. For larger actuation forces, the bending of the connector becomes significant.

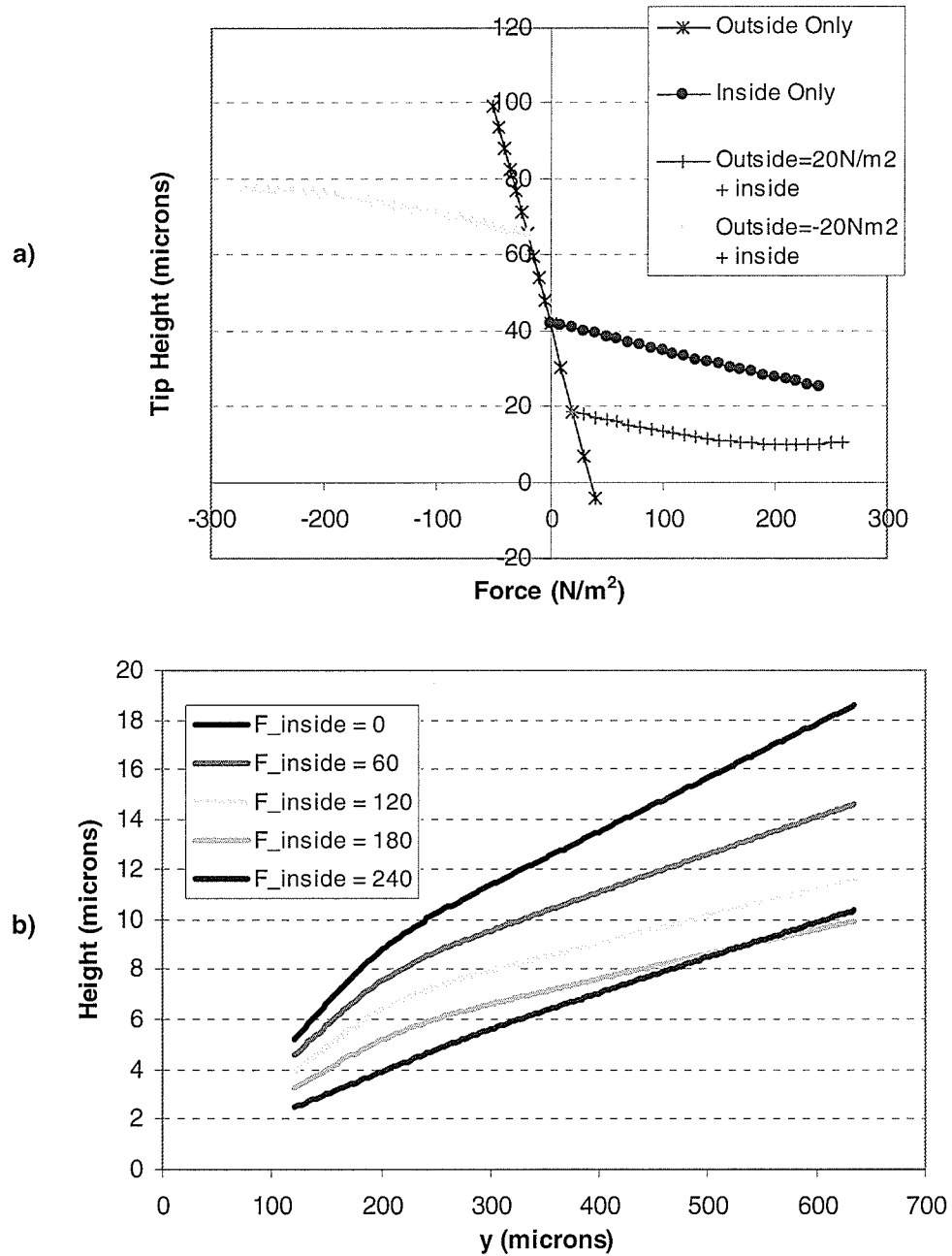


Fig. 5.6: (a) Extended tip height versus actuation force plot for the wide RC actuator showing actuation symmetry about the resting position. Note the flattening out of the inside actuator curves as forces increase. (b) Profiles of the connector along its length for $f_{L-out} = 20N/m^2$ and various f_{L-in} . Note the pivoting behavior about the point at $y = 171\mu m$ where the inside crossbar is attached.

5.4 Chapter Summary

In this chapter, we have presented the general design of a novel large-deflection

electromagnetic actuator with rotationally corrected motion throughout its entire range. Through detailed FEM analysis of two different devices, we have studied the main aspects of the device with respect to film stress and actuation. This device still holds many of the desirable characteristics of the basic Lorentz actuator in chapter 4, at the same time it also presents several more aspects of the design yet to be studied and characterized in detail.

CHAPTER 6: TESTING AND VERIFICATION

6.1 Overview

Following the successful fabrication of the Lorentz actuators, these devices were subjected to a series of characterization tests in order to verify their intended design. These tests included initial height measurements, radius of curvature, static DC deflection versus current, lifetime test, and hybrid actuation test. These tests are not meant to be an exhaustive characterization of the devices, but rather they serve as a good proof of the design concepts. The details of how the tests were performed and their respective results are presented in this chapter for both the basic and RC actuators.

6.2 Experiment Setup

Testing of fabricated devices were performed on a probe station equipped with an optical microscope of depth of focus $< 2\mu\text{m}$. The probe station is set on an anti-vibration air-damped table shown in Fig. 6.1. The static rest height of the devices at various points is determined by measuring the height between focusing on the base of the arm and the point of interest. The same method can be used to measure the deflection of the devices under DC actuation currents. The actuation is applied using an Agilent E3649A Programmable DC Power Supply through micro probes placed onto the device contact pads. External magnetic field is achieved using permanent magnets which have a magnetic field of 0.25T measured at its surface. A custom aluminum holder was used to hold the devices and magnets in proper (orthogonal) orientation for

Lorentz actuation.

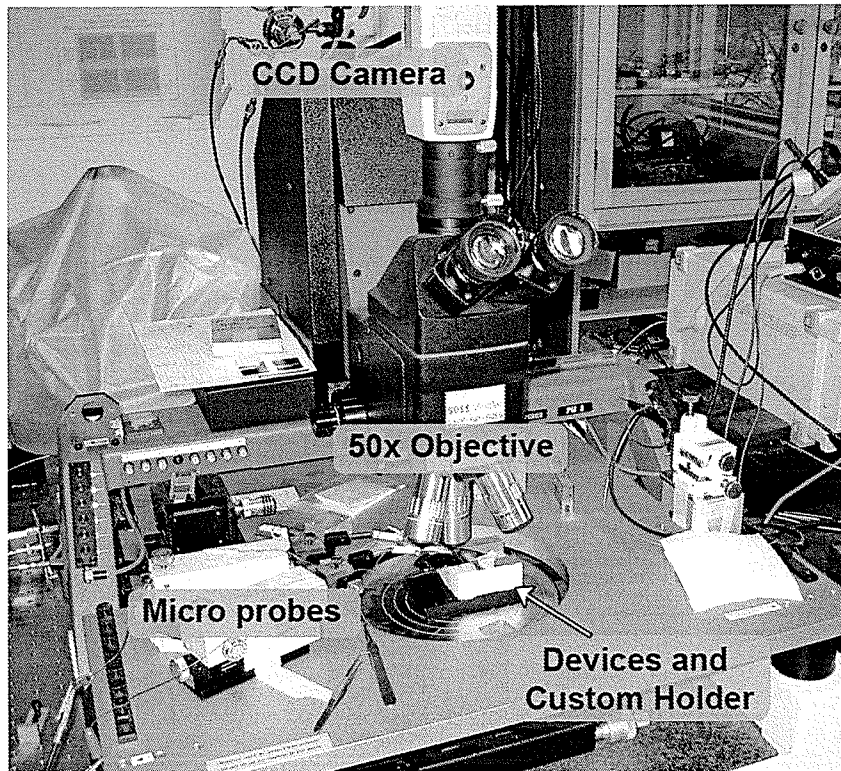


Fig. 6.1: Experimental setup of the Lorentz actuator probe station.

6.3 Basic U-Shaped Actuator Results

6.3.1 Static Analysis

The initial tip rest height of the fabricated basic U-shaped actuator was measured to be $107\mu\text{m}$. This agrees with the previous simulation result of $104\mu\text{m}$ for $\sigma_{Cr} = 0.45\text{GPa}$. To gain further confidence in this measurement, we first measured the height of the device at key locations illustrated in Fig. 4.1c, and then use equation 2.4 to calculate the radius of curvature in the arms of the fabricated device. The radius obtained this way is $7.3 \times 10^{-4}\text{m}$. On the other hand, the expected radius from theory of equation 2.1a for stress levels $\sigma_{Al} = 0$ and $\sigma_{Cr} = 0.45\text{GPa}$ is $6.7 \times 10^{-4}\text{m}$. The discrepancy

in radii is likely due to the difference between actual and measured film thicknesses, and also due to uncertainties in the stresses of the deposited layers. Nevertheless, the similarity between measurements and calculations does indicate that the fabricated devices are in fact behaving properly as bimetallic stressed devices should. The picture of a representative device at rest in Fig. 6.2 further shows curvature where the Cr sections are, and more or less straight structural beams everywhere else. The bright areas are those which reflect light directly back at the microscope camera, whereas the darker areas correspond to places where less light is reflected back at the camera, indicating an inclined surface. Notice that the Al-only sections of the device have a nice linear gradient, indicating that the inclined surfaces are not warped. This confirms that the structural Al used is low in stress as desired.

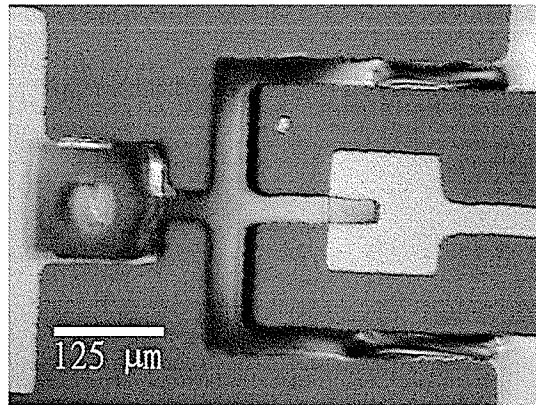


Fig. 6.2: Picture of a representative basic U-shaped actuator.

6.3.2 Actuation Analysis

To determine the characteristics of the basic U-shaped device under actuation, we applied DC currents to the device and then measured its tip deflection. The tip height of the basic Lorentz actuator is plotted as a function of applied current in Fig. 6.3. This figure also shows the simulated results from section 4.4.4 converted to current using

equation 3.1. There is good agreement between the two sets of data. Both show linear movement of tip height versus current, and a touch-down point below 20mA. This verifies the linear characteristic of the proposed basic actuator. The required actuation voltage across this device at 20mA was 90mV, which corresponds to 1.8mW of power and 4.5Ω of resistance across the actuator.

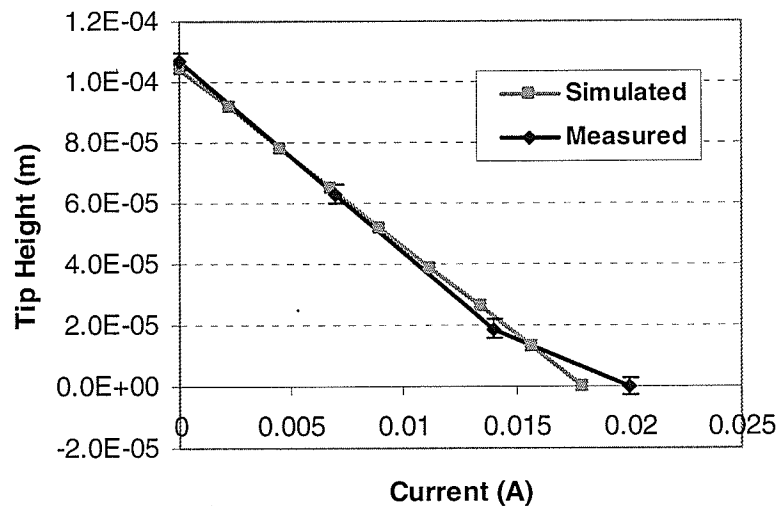


Fig. 6.3: Deflection vs Drive Current for basic Lorentz Actuator

After the tip of the actuator has been brought into contact with the bottom electrode using Lorentz actuation, electrostatic voltage was applied to the bottom electrode to hold the tip in position. Once the electrostatic force takes over, the Lorentz actuation can be released, thus minimizing steady state holding power. The minimum required holding voltage here was 10.3V. At first glance, this voltage is quite high considering the two electrodes have large dimensions of $125\mu\text{m} \times 125\mu\text{m}$ and that the tip is already touching the surface. However, recall from section 4.5.2 that the domed profile of the arms during actuation actually causes an inclined angle of the connector with respect to the substrate. The separation between the connector and the electrostatic

electrode actually increases as we move along the connector away from the tip, hence the large holding voltage. Nevertheless, this experiment shows that the actuator is capable of being used as a hybrid switch which greatly reduces the holding power.

A final note on the actuation of the basic Lorentz devices is regarding their ability to adjust the initial resting height through plastic deformation of the structure. The idea here is to “bend” the structure upwards using the same Lorentz actuation beyond its elastic regime, thus causing permanent deformation in the arms. This technique has been directly used in [12] on non-bimetallic U-shaped devices to obtain increasing out-of-plane curvature with each time the devices are deformed. On our bimetallic structures, we can further study the ability to adjust the rest height in the opposite direction where the structure is driven *into* the surface. This was observed on the basic U-shaped actuator when the actuator was driven to 47mA, well beyond the touch down point of 20mA. Subsequently, the initial rest height of the device dropped to only 57 μ m instead of returning to its 107 μ m position. This deformed final shape is illustrated in the actuation snapshots in Fig. 6.4. The 20mA touchdown snapshot also shows that the crossbar is resting at a certain height (indicated by its shadow) while the tip is in contact with the bottom electrode. The exact height for this particular device under test was within measurement limits ($< 5\mu$ m), therefore it is not presented. Nonetheless, it does confirm our expectation of the domed profile of the arms.

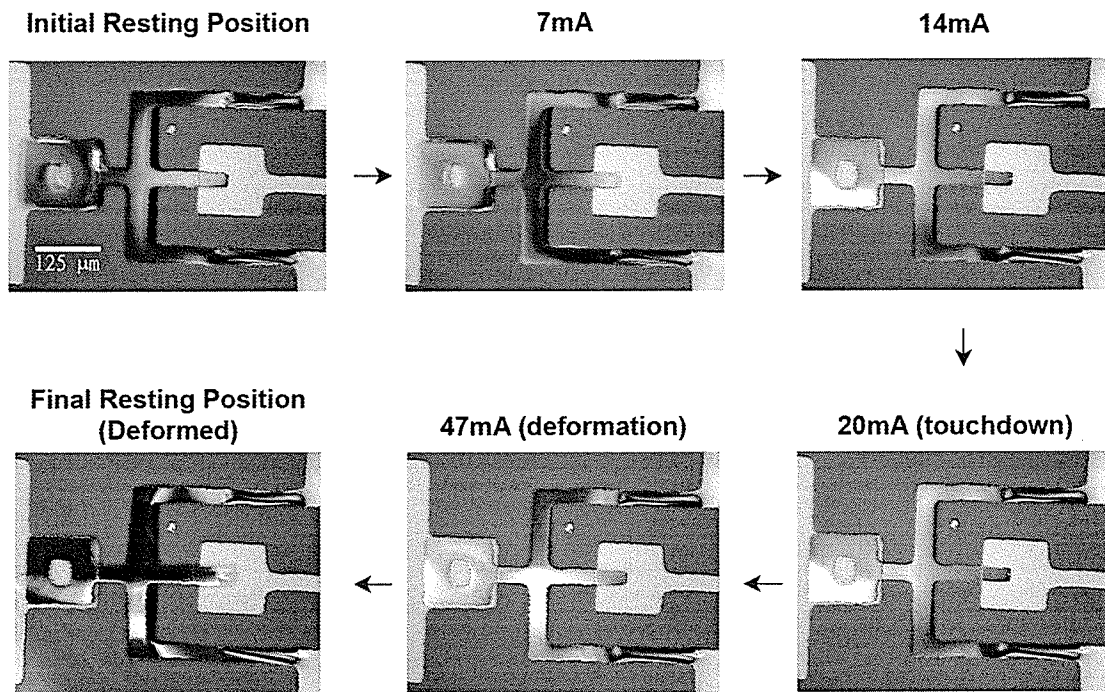


Fig. 6.4: Actuation snapshots of the basic actuator, showing the entire actuation process and the post-release height adjustment process.

6.4 Rotationally Corrected Devices

6.4.1 Static Analysis

For the RC devices, tip height measurement as a function of stress was also done using the same experimental setup. Radius of curvature analysis was already discussed in the basic actuator section, and will not be discussed again here for the RC devices since the analysis would be almost identical. The initial resting tip height for the first RC device also agrees reasonably well with simulation: measured $97\mu\text{m}$, simulated $92.3\mu\text{m}$. The first fabricated RC device showed a stress of 0.45GPa , whereas the second RC device (double width) showed a different stress level of 0.25GPa due to on-wafer variations in fabrication conditions. The measured resting height for the

second RC device is $38\mu\text{m}$ and the simulated height was $42\mu\text{m}$ at this stress level. For both devices, the measured height agrees reasonably well with simulated results.

6.4.2 Actuation Analysis

The deflection versus applied current measurements are plotted in Fig. 6.5 for the individual actuation of the inside and outside arms. The simulated result from section 5.3.3 is also included in the same plot for comparison. We present the collected data for the wide RC actuator here because of its higher slope ratio and overall deflection. Once again the simulated results are converted to current using equation 3.1.

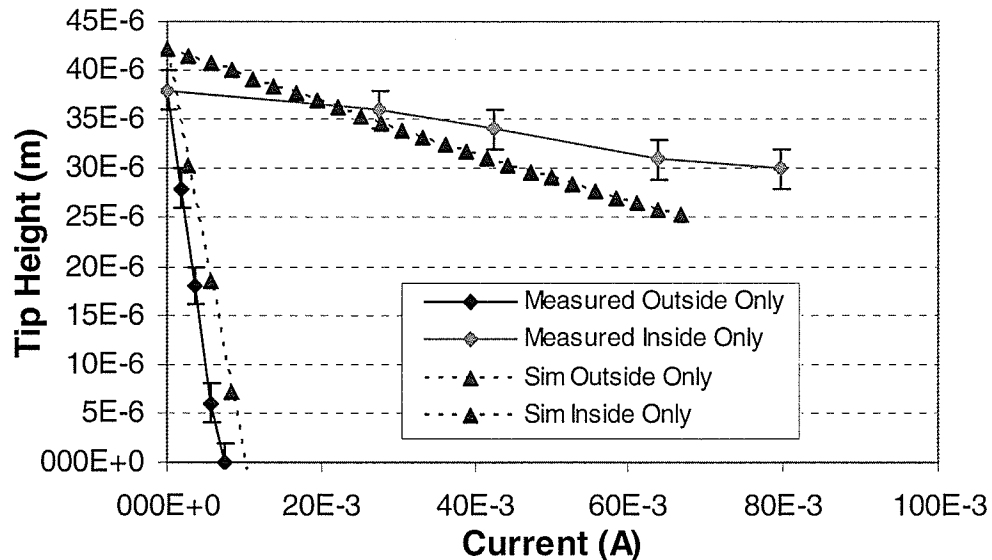


Fig. 6.5: Simulated and measured deflection versus current results for the wider RC device.

From this plot, we can see that the measured results and the simulated results agree well for the outside arm. For the inside arm, the slope differs slightly. This is likely due to differences between the actual path through which the current travels and the simulated path. This difference arises from the fact that the crossbar length in the

models includes arm widths, whereas the actual path is uncertain at the joint. Nevertheless, the observed curves confirm the intended design of the RC actuators' ability to provide large deflection with fine tune control. They also show a desirable linear characteristic in both curves for analog position control. Note that the slope for the outside arm actuation curve is also significantly higher than that of the basic actuator in section 6.2.2 due to the longer length of the crossbar.

Actuation tests for cases when both arms are under actuation were not conducted due to the limitation in depth measurement precision. The perturbation in height in these cases exceeds the limits of reliable measurement with the available equipment.

The degradation of the RC device over time was also tested by subjecting the device to over a million actuation cycles using a square wave at 500Hz. The voltages and offsets were setup such that the offset puts the actuator in the midpoint of its vertical range, and that the peak to peak values correspond to the touch down and initial rest height. The first RC device was presented here for its larger rest height of 100 μ m. Fig. 6.6 shows the deflection characteristics of this device before and after the 1.2 million cycle testing. The plot shows no major measurable signs of degradation, indicating that the arms are still within the elastic regime of operation over its entire range.

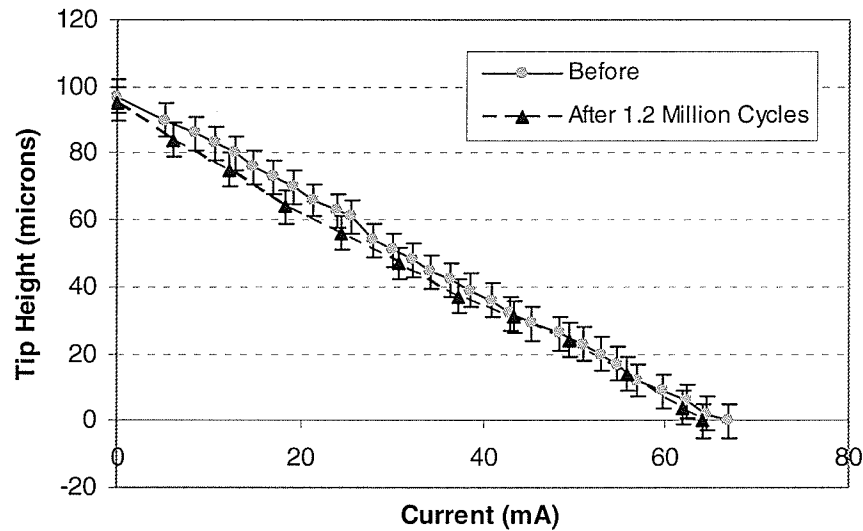


Fig. 6.6: Deflection characteristics before and after lifetime testing of 1.2 million cycles.

6.5 Chapter Summary

In this chapter, we have presented a set of measurement data collected on the fabricated devices with identical dimensions as the simulated devices. First, the basic U actuators showed initial deflection-stress characteristics that agree with theory, thus indicating that the devices are indeed behaving as bimetallic structures. Then, deflection of the basic devices under actuation agreed well with the simulated results, confirming that the devices do behave linearly in the range of interest. Second, the RC actuators were studied with respect to their deflection versus various actuation applied. The results here also agree with simulated results, and confirm that the RC devices indeed function as designed – with a large deflection and fine position control ability. Lifetime testing of over a million cycles indicates that these compliant structures are good candidates for such large deflections since it showed little or no degradation. Hybrid electrostatic actuation of the device was also verified.

CHAPTER 7: DISCUSSION OF RESULTS

7.1 Overview

This chapter presents a discussion of the results presented earlier with regards to the design and performance of the large deflection actuators. More specifically, the performance of the devices as an actual RF MEM switch, the different design parameters which affect actuator performance, and potential applications for the devices are elaborated in greater detail. The discussions in this chapter are not meant to provide a detailed scientific comparison of the devices, but rather to give the reader a general idea of how the actuators developed will fare against other actuators in literature.

7.2 Large-Deflection Switch Performance

The performance goals set out at the beginning of this work were to develop a large-deflection actuator with $> 100\mu\text{m}$ deflection, low actuation voltage and power. In chapter 6, these goals are met and verified. However, the performance of these actuators as RF MEM switches was not experimented in detail. Some of the common benchmarks in switch performance include switching speed, insertion loss and isolation, and power consumption.

Even though detailed characterization of these benchmarks on the actuator developed is outside the scope of this work, their general performance can be estimated. First, the absolute switching time of the basic and RC actuators would be higher (i.e.

slower) than most of the electrostatic switches studied in literature primarily due to the larger range of travel as required by our goals. But in terms of their resonant frequency, the analysis would be very close to a cantilever with a point load at the end of the arm. In other words, the resonant frequency of these actuators would be comparable to that of a similarly sized MEM actuator with electrostatic actuation. Cantilever devices with hundreds of micrometers lengths typically have resonant frequencies in the hundreds of Hz to a couple of kHz range [11].

Second, the insertion loss of the MEM switches at higher frequencies would be relatively low compared to solid-state devices, since the switches have metal-to-metal contacts. The isolation of the MEM switches developed should be much better than existing solid-state devices, and likely show a significant improvement over existing MEM devices.

Third, the power consumption of these large-deflection actuators is highly dependent on how the device is operated. When used as ON-OFF switches, the power consumption can be minimized due to the hybrid actuation scheme. Significant current is only required during switching, and none required when holding a state. Thus, the overall power consumption in this case would just be slightly higher than existing electrostatic switches. When used as micro-mirrors with analog control of position, constant current is required to hold its position. Therefore, much more power is consumed in this case compared to electrostatic devices.

7.3 Design Parameters Affecting Actuator Performance

There are several design factors which determine the performance of the actuators.

First, the length of the arms determines the spring constant of the actuator (given a fixed thickness), which in turn affects the switching speed and holding voltage. Second, the length of the crossbar is directly proportional to actuation force and required switching current. These two parameters should be designed to suit the application in mind for the basic actuator.

For the rotationally corrected actuator, the optimization of geometry is not as straightforward. In addition to the design of arm and cross bar lengths, another main factor to be considered is the positioning of the inside actuator with respect to the outside actuator. More specifically, the effects of various spacing between the two actuators on deflection need to be characterized in better detail to reveal any design considerations. Change in size of this spacing would likely cause more or less bending in the crossbar, thus affecting overall tip deflection. In addition to the spacing of the two actuators, the relative lengths of the tensile metal on the two arms also have an effect on initial rest height. Difference in the lengths of the chrome would cause the connector to bend while in the resting position, and would likely behave like a “bias” in the actuation of the device in either direction.

7.4 Potential Applications

The primary application for the actuators developed in this work would be RF switches. The large deflection offered by these actuators is their key advantage, and would certainly result in higher RF isolation during the off state. Metal-to-metal contact would also offer low contact resistance and insertion loss during the ON state. The large initial rest height also offers improved isolation during the OFF state. Other

advantages include the ability to actively release itself in the case of a minor stiction, thus improving reliability. The fine-tune ability of the rotationally corrected actuator could also be useful in the case of capacitive RF switches, where the position of the actuator can be used to change capacitance with high precision. On the downside, the primary concern of employing these actuators would be the requirement of an externally placed magnetic field parallel to the substrate surface. This is not always possible in certain applications.

An application to the rotationally corrected actuators is micro-mirrors and optical switches. The distinguishing feature of these actuators as micro-mirrors would be the ability to both obtain a large deflection range (and deflection angle) while maintaining fine position control at the same time. The basic actuators can also be used as micro-mirrors with as studied in detail by J. Johnson [4]. The major drawback to using these devices as micro-mirrors would be the requirement for constant current (power) during actuation.

7.5 Chapter Summary

In this chapter, inspirational discussions pertaining to the performance of the large-deflection actuators are presented. Compared to existing electrostatic switches, the Lorentz/electrostatic actuators offer much larger deflection at a lower voltage. Their switching speeds and power handling capabilities are also comparable to similarly sized electrostatic actuators. However, the major trade-off is the significant power consumed when analog control of position is required of these actuators. The discussion has also pointed out several factors which affect the performance of these actuators, and how

some of these factors might be optimized for their application.

CHAPTER 8: FUTURE WORK, SUMMARY AND CONCLUSIONS

8.1 Future Work

The work done in this project has shown that a magnetic-electrostatic bimorph actuator is a viable way to achieve large-deflection in micromachined devices with low actuation voltages and low power using conventional semiconductor processes. There is, however, much more future work in optimizing/improving the performance of these actuators.

The first way of improving the performance of the basic actuators is to customize the actuator geometry (length, width, and height of the arms and crossbar) according to the specific application. For the basic actuator, it is straightforward to specify a desired initial rest height and determine the required tensile metal length using equations 2.2 and 2.3. Then, the arm lengths and crossbar length can be designed to suit the desired application. Following the optimization of geometry, the performance of the actuator should be tested as a high-isolation RF switch to verify its performance in an RF system. A variation in geometry that could be considered is tapering of the arms along its length (i.e. decreasing width in the arms). This allows for even more control over the spring constant of the device.

For the rotationally corrected design, there are more ways in which they can be implemented. A few of these ideas and suggestions are shown in Fig. 8.1. These designs were mainly included here for the reader's interest and to inspire future designs.

In device “JJ3”, the mirror is placed in between the two actuators, hence potentially allows for more flexibility in controlling the connector angle. Alternatively, if the external magnetic field is oriented parallel to the crossbars, the forces generated from current through the arms would be equal and opposite in the z-direction. Therefore, the arms would exert torque about the connector when actuated, which in turn results in the rotation of the mirror about the connector (as opposed to rotating about the crossbars in the devices presented in earlier chapters).

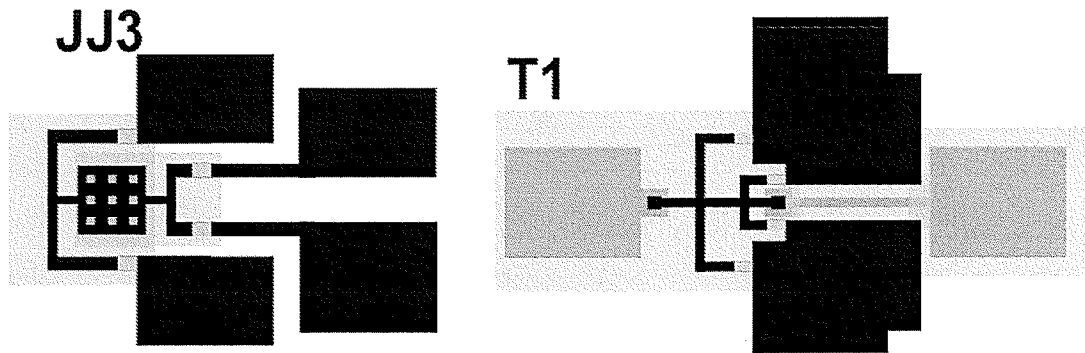


Fig. 8.1: Interesting extensions and alternative implementations of the rotationally corrected actuator. Design “JJ3” allows more control to the angle of the mirror by placing it in between the actuators, and it also allows the mirror to twist by orienting the magnetic field parallel to the crossbars. Design “T1” introduces an offset in the arm anchors for further flexibility in the design of the device.

Finally, the rotationally corrected actuator should be tested as a micro-mirror, and perhaps in a RF system with capacitive switching to better take advantage of their fine-tune ability.

8.2 Alternative Materials

The materials for structural and tensile layers in this work were chosen for two primary reasons. One is that neither aluminum nor chrome is magnetic. If they were it

would introduce deflection in the structure with just the external magnetic field. The other reason is the relative residual stresses between these materials are required for the desired initial rest height. For these reasons, the tensile layer (chrome, which is non-standard in electronic fabrication processes) can be replaced with any other material that exhibits similar residual stress (i.e. tensile). One material to consider in particular is titanium, because it is one of the standard electronic fabrication materials and allows for better process integration.

8.3 Summary

Large-deflection micromachined actuators have a potential to further improve the isolation of RF micromachined switches. A type of bimorph Lorentz actuators for such applications was developed in this work. These actuators were fabricated using a 2-mask low-aspect ratio process developed at the University of Manitoba. Upon release, the residual stress in the layers causes the actuator to deflect out-of-plane with a deterministic rest height. Actuation of the devices is very linear with applied current, and agrees well with FEM simulations. These simulations also revealed that the switches have minimal contact area when closed, and can also function as tri-state switches. Furthermore, the switches can also be held in the closed position using electrostatics, thus minimizing holding power.

An advanced extension of the basic actuator was also developed. This rotationally corrected design allows for large deflection and at the same time fine adjustments to the tip height and angle using separate controls. Such actuator would be suitable in applications such as the micro-mirror. Finite element modeling of this design

also confirms its intended design and agrees with measured results.

8.4 Conclusions

The results from this work has shown that a bimorph magnetic-electrostatic MEM actuator is capable of large-deflections $> 100\mu\text{m}$ requiring less than 10V actuation voltage. A two-mask fabrication process using conventional low aspect ratio semiconductor techniques has been studied and developed, which allows for reliable fabrication of the actuators. These actuators show great promise as high-isolation RF switches and micro-mirrors. Some additional development/optimization in the design of these actuators should allow them to be implemented in actual applications in future work.

REFERENCES

- [1] S.A. Campbell, "The Science and Engineering of Microelectronic Fabrication", 2nd edition, Oxford University Press, 2001.
- [2] T. Yasuda, I. Shimoyama, H. Miura, "CMOS Drivable Electrostatic Microactuator with Large Deflection", Proceedings from the Tenth IEEE Annual International Workshop on Micro Electro Mechanical Systems, 1997, 26-30 Jan. 1997, pp 90 – 95.
- [3] I. Song, P.K. Ajmera, "Use of a Photoresist Sacrificial Layer with SU-8 Electroplating Mould in MEMS Fabrication", Journal of Micromechanics and Microengineering, vol. 13, no. 6, November 2003, pp. 816 - 821.
- [4] J. Johnson, "Stressed Micromachined Magnetic Actuators for Micro-mirror Applications", M. Sc. Thesis, University of Manitoba, 2006.
- [5] M. Bartek, R.F. Wolffenbuttel, "Dry Release of Metal Structures in Oxygen Plasma: Process Characterization and Optimization", Journal Micromechanics and Microengineering, vol. 8 no. 2, June 1998, pp. 91–94.
- [6] H.F. Winters, J.W. Coburn, "The Etching of Silicon with XeF₂ Vapor", Applied Physics Letters, vol. 34, January 1979, pp. 70-73.
- [7] G.T.A. Kovacs, "Micromachined Transducers Sourcebook", WCB/McGraw-Hill, 1998.
- [8] P.B. Chu, J.T. Chen, R. Yeh, G. Lin, J.C.P. Huang, B.A. Warneke, K.S.J. Pister, "Controlled Pulse-Etching with Xenon Difluoride", Proceedings of Transducers '97, the 1997 International Conference on Solid-State Sensors and Actuators, Chicago, IL, June 16-19, 1997, vol. 1, pp. 665-668.
- [9] G.M. Rebeiz, J.B. Muldavin, "RF MEMS Switches and Switch Circuits", IEEE Microwave Magazine, vol. 2, Issue 4, Dec. 2001, pp. 59 – 71.
- [10] Chen, R.T.; Nguyen, H.; Wu, M.C., "A low voltage micromachined optical switch by stress-induced bending", Micro Electro Mechanical Systems, 1999. MEMS '99. Twelfth IEEE International Conference on 17-21 Jan. 1999 Page(s):424 - 428

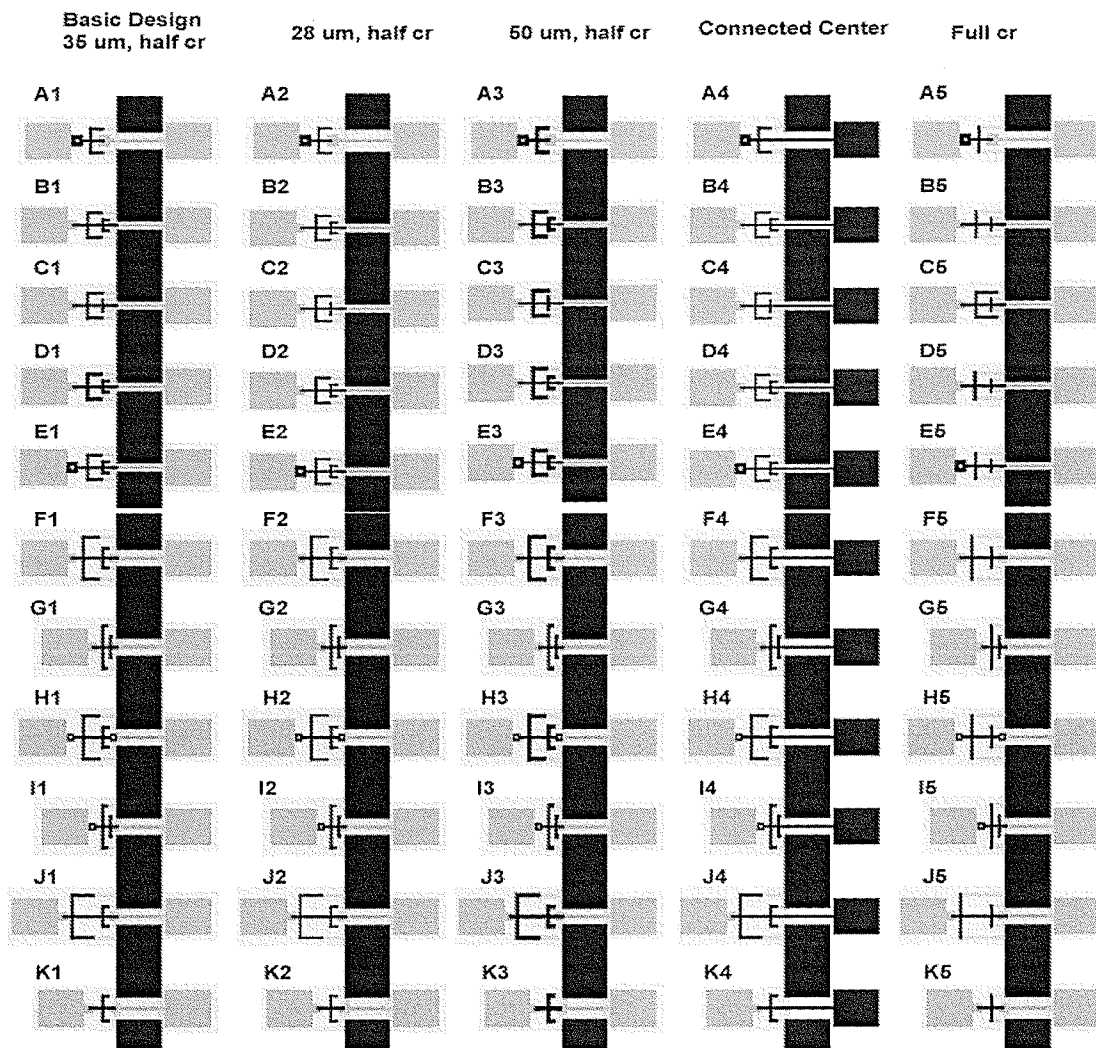
- [11] I. Cho, T. Song, S. Baek, E. Yoon, "A Low-Voltage and Low-Power RF MEMS Series and Shunt Switches Actuated by Combination of Electromagnetic and Electrostatic Forces", IEEE Transactions on Microwave Theory and Techniques, vol. 53, no. 7, July 2005, pp. 2450 – 2457.
- [12] R. Holzer, I. Shimoyama, H. Miura, "Lorentz Force Actuation of Flexible Thin-Film Aluminum Microstructures", Micro Electro Mechanical Systems 1998, proceedings of the eleventh annual international workshop on, 25-29 Jan. 1998, pp. 24 – 28.
- [13] R.N. Simons, D. Chun, L.P.B. Katehi, "Microelectromechanical Systems (MEMS) Actuators for Antenna Reconfigurability", Microwave Symposium Digest, 2001 IEEE MTT-S International, vol. 1, 20 – 25 May 2001, pp. 215 - 218.
- [14] L. Que, J.S. Park, Y.B. Gianchandani, "Bent-beam Electrothermal Actuators-Part I: Single Beam and Cascaded Devices", Journal of Microelectromechanical Systems, vol. 10, Issue 2, June 2001, pp. 247 – 254.
- [15] T. Fujita, K. Maenaka, Y. Takayama, "Dual-axis MEMS mirror for large deflection-angle using SU-8 soft torsion beam", Sensors and Actuators A: Physical, vol. 121, Issue 1, 31 May 2005, pp. 16-21.
- [16] A. Borgioli, Y. Liu, A.S. Nagra, R.A. York, "Low-Loss Distributed MEMS Phase Shifter" IEEE Microwave Guided Wave Lett., vol. 10, pp. 7–10, Jan. 2000.
- [17] I. Schiele, B. Hillerich, F. Kozlowski, and C. Evers, "Micromechanical relay with electrostatic actuation", 1997 International Conference on Solid-State Sensors and Actuators", Transducers '97, Chicago, June, vol. 2, pp. 1165–1168.
- [18] I. Shimoyama, O. Kano, H. Miura, "3D Micro-structures Folded by Lorentz Force", The Eleventh Annual International Workshop on Micro Electro Mechanical Systems, 1998. MEMS '98 Proceedings, 25-29 Jan. 1998, pp. 24 – 28.

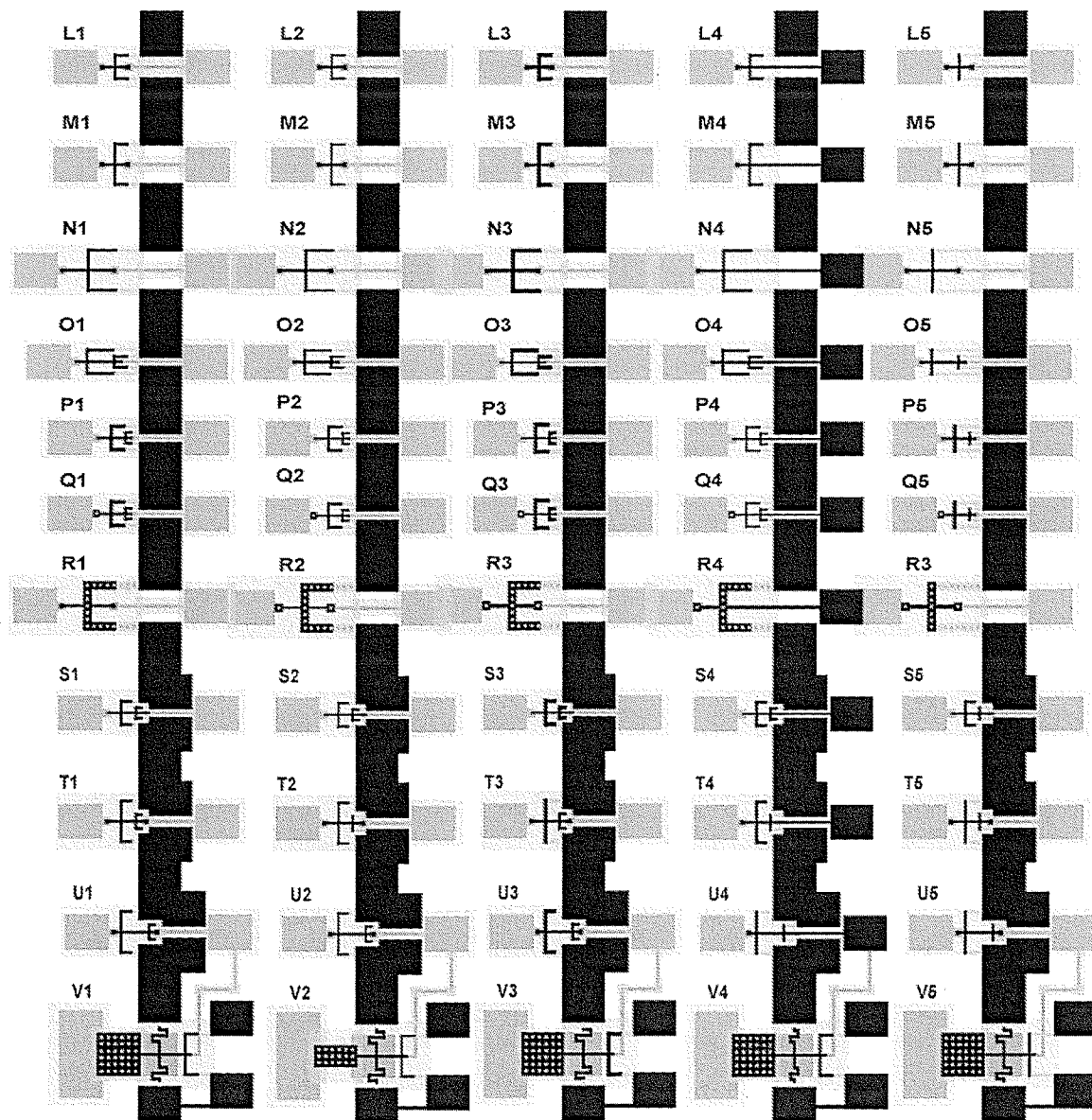
All referenced images reprinted with permission in [2, 9, 10, 11, 18]. © IEEE

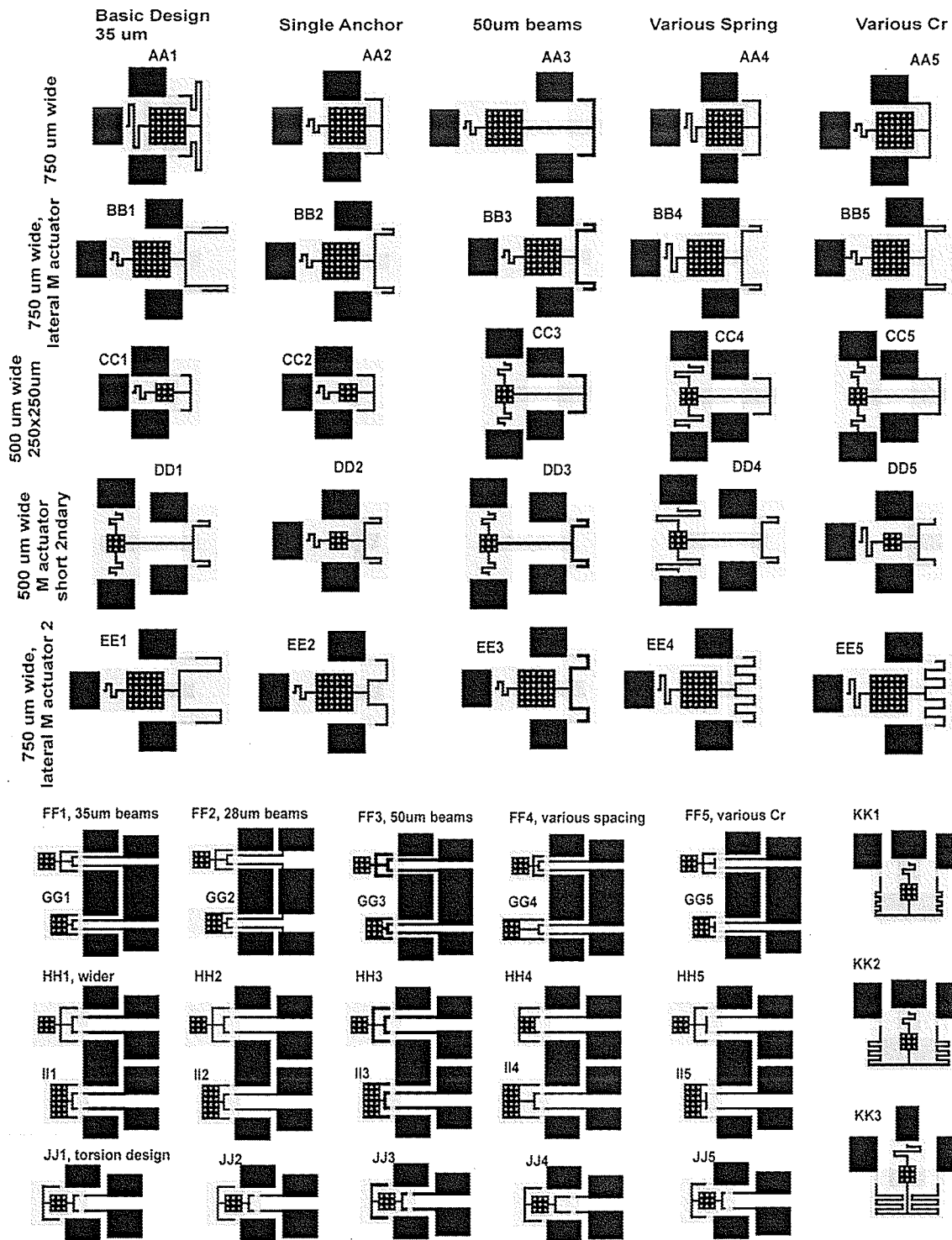
APPENDICES

| | |
|--|-----|
| APPENDIX A: Design masks in Adobe Illustrator® format | A1 |
| APPENDIX B1: Detailed information on COMSOL Multiphysics model of the basic actuator | A7 |
| APPENDIX B2: Detailed information on COMSOL Multiphysics model of the rotationally corrected actuator | A19 |
| APPENDIX C: Matlab code for radius of curvature calculation in a bimorph cantilever | A30 |
| APPENDIX D: Heat Analysis of the Basic Actuators | A32 |

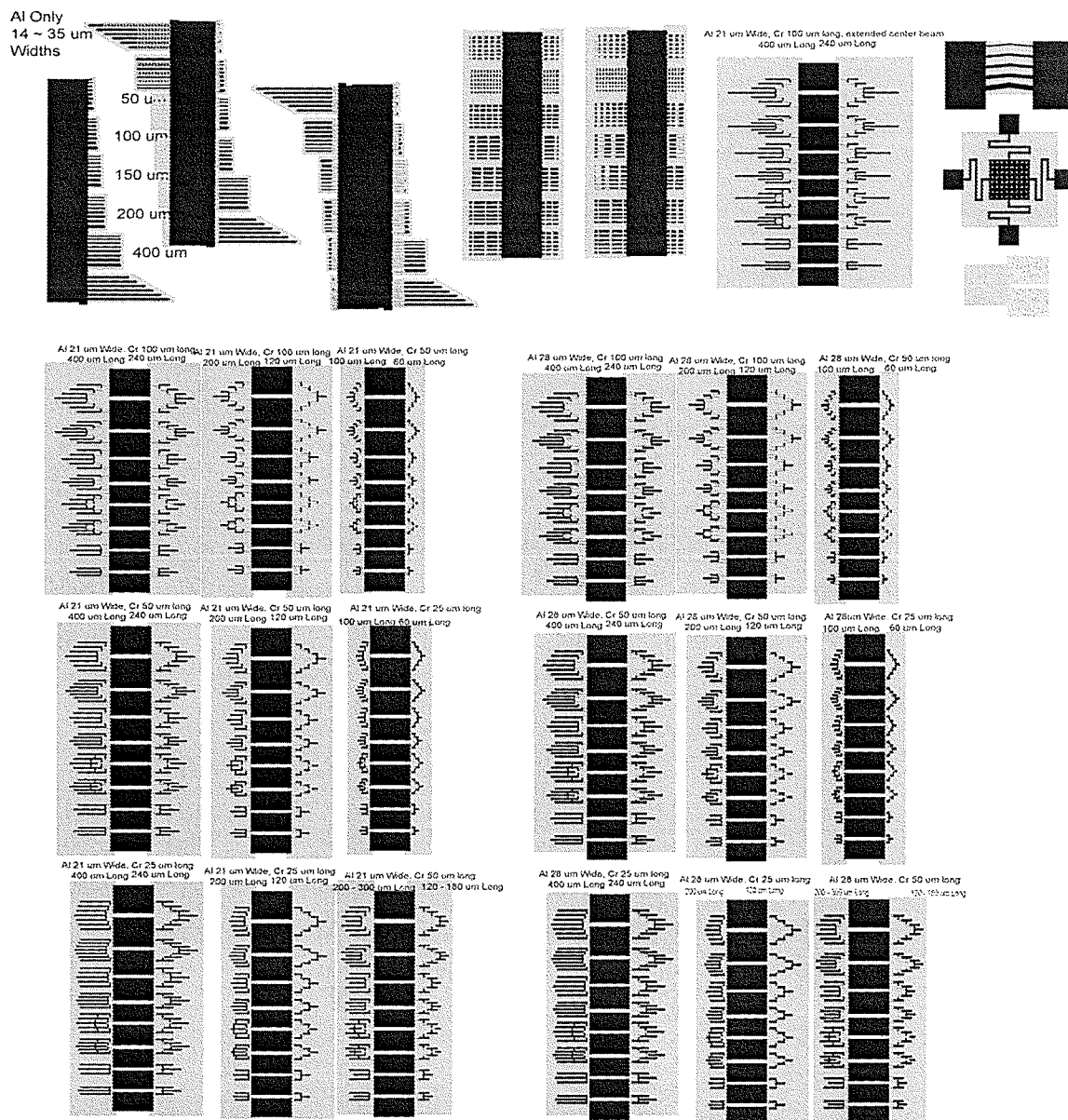
Appendix A1: Basic U-Actuator and Rotationally Corrected Actuator Design Masks in Adobe Illustrator® Format







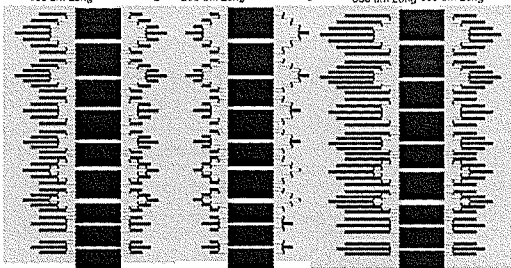
Appendix A2: Cascaded Electrostatic Cantilevers Design Masks in Adobe Illustrator® Format



Al 35 μ m Wide, Cr 100 μ m long
400 μ m Long 240 μ m Long

Al 35 μ m Wide, Cr 100 μ m long
200 μ m Long 120 μ m Long

Al 35 μ m Wide, Cr 100 μ m long
600 μ m Long 360 μ m Long



Al 28 μ m Wide, Cr 28 - 42 μ m
400 μ m Long 240 μ m Long

Al 28 μ m Wide, Cr 28 - 56 μ m
400 μ m Long 240 μ m Long

Al 28 μ m Wide, Cr 56 - 100 μ m
400 μ m Long 240 μ m Long



Al 28 μ m Wide, Cr 28 - 42 μ m
decreasing lengths < 400 μ m

Al 28 μ m Wide, Cr 28 - 56 μ m
decreasing lengths < 400 μ m

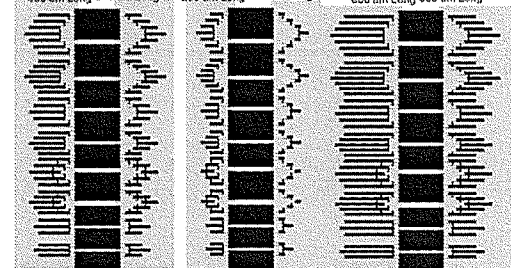
Al 28 μ m Wide, Cr 56 - 100 μ m
decreasing lengths < 400 μ m



Al 35 μ m Wide, Cr 50 μ m long
400 μ m Long 240 μ m Long

Al 35 μ m Wide, Cr 50 μ m long
200 μ m Long 120 μ m Long

Al 35 μ m Wide, Cr 50 μ m long
600 μ m Long 360 μ m Long



Al 35 μ m Wide, Cr 28 - 42 μ m
400 μ m Long 240 μ m Long

Al 35 μ m Wide, Cr 28 - 56 μ m
400 μ m Long 240 μ m Long

Al 35 μ m Wide, Cr 56 - 100 μ m
400 μ m Long 240 μ m Long



Al 35 μ m Wide, Cr 28 - 42 μ m
decreasing lengths < 400 μ m

Al 35 μ m Wide, Cr 28 - 56 μ m
decreasing lengths < 400 μ m

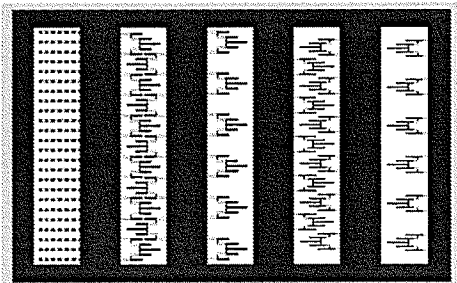
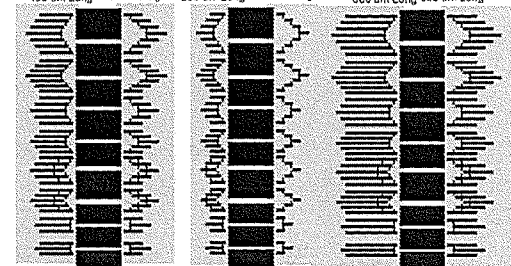
Al 35 μ m Wide, Cr 56 - 100 μ m
decreasing lengths < 400 μ m



Al 35 μ m Wide, Cr 25 μ m long
400 μ m Long 240 μ m Long

Al 35 μ m Wide, Cr 25 μ m long
200 μ m Long 120 μ m Long

Al 35 μ m Wide, Cr 25 μ m long
600 μ m Long 360 μ m Long



Align

Appendix B: Finite Element Modeling Details

This appendix was meant to be both a detailed guide to future work as well as a detailed record of the simulations performed in this work. Below is a quick step-by-step guide to setting up the simulations in COMSOL Multiphysics 3.2.0.300 – MEMS Module using Solid, Stress-Strain physics, followed by complete model reports of the basic Lorentz U actuator and the double arm structure.

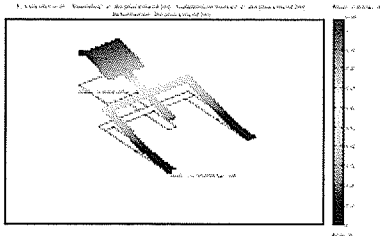
1. Start a new 3-D COMSOL Multiphysics simulation under the MEMS Module using Solid, Stress-Strain non-linear static analysis.
2. Set the current working plane to an arbitrary point in the z -axis so that the model can be drawn in 2-D in the xy -plane.
3. In the 2-D geometry mode, draw a 2-D model of the desired geometry.
4. Select all geometry blocks which to extrude into the 3-D structure. Select “Draw-Extrude...” from the drop down menu, and extrude for the thickness of the selected geometry.
5. Repeat steps 2 – 4 for all layers, one layer at a time. Make sure the current working plane was set appropriately each time.
6. Once the 3-D structure is completely drawn, we can move onto indicating the materials of all the blocks. Do this under the subdomain settings in the Physics drop-down menu.
7. To include residue stress in the materials, check the “include initial stress” box and type in a desired value. If stress is to be treated as a parameter in the

simulation, type in a user defined variable name and make sure you define that name under the “Options -> Constants” menu.

8. After material properties are set, move onto boundary condition settings under the “Physics -> boundary settings” menu. Select all boundaries which will remain “anchored” relative to the rest of the structure, and then check off the x, y, and z position constraint boxes, and make sure they are all set to 0.
9. Mesh the structure by clicking “Mesh -> Initialize”. Note that mesh element count directly affects solving time and accuracy. Adjust as required. A good adjustment is to scale in the z-direction by a factor of 1.5.
10. Finally we move onto setting up the solver. Make sure the large-deflection option under the “Physics -> Properties” menu is selected. If a parametric simulation is desired, select “parametric non-linear” in the solver box. Note that a parametric simulation requires that the user indicate the list parameter values to be used under the “Solve -> Solve Parameters”. Usually this list of values needs to be ramped up gradually for the model to converge properly.
11. Click “solve” to start the simulation.
12. When the simulation completes, post processing can be performed as desired.



Appendix B1: COMSOL Model Report – Basic Lorentz U Actuator



1. Table of Contents

- Title - COMSOL Model Report
- Table of Contents
- Model Properties
- Constants
- Geometry
- Geom1
- Geom2
- Materials/Coefficients Library
- Solver Settings
- Postprocessing

2. Model Properties

| Property | Value |
|----------------|---------------------------------|
| Model name | D7_A2 |
| Author | Kwan-yu Lai |
| Company | University of Manitoba |
| Department | Electrical/Computer Engineering |
| Reference | |
| URL | |
| Saved date | Dec 1, 2005 9:12:00 AM |
| Creation date | Nov 7, 2005 2:05:12 PM |
| COMSOL version | COMSOL 3.2.0.300 |

File name: /Users/student/Desktop/D7_A2-new 0-190Nm2.mph

Application modes and modules used in this model:

- Geom1 (3D)
 - Solid, Stress-Strain (MEMS Module)
- Geom2 (2D)

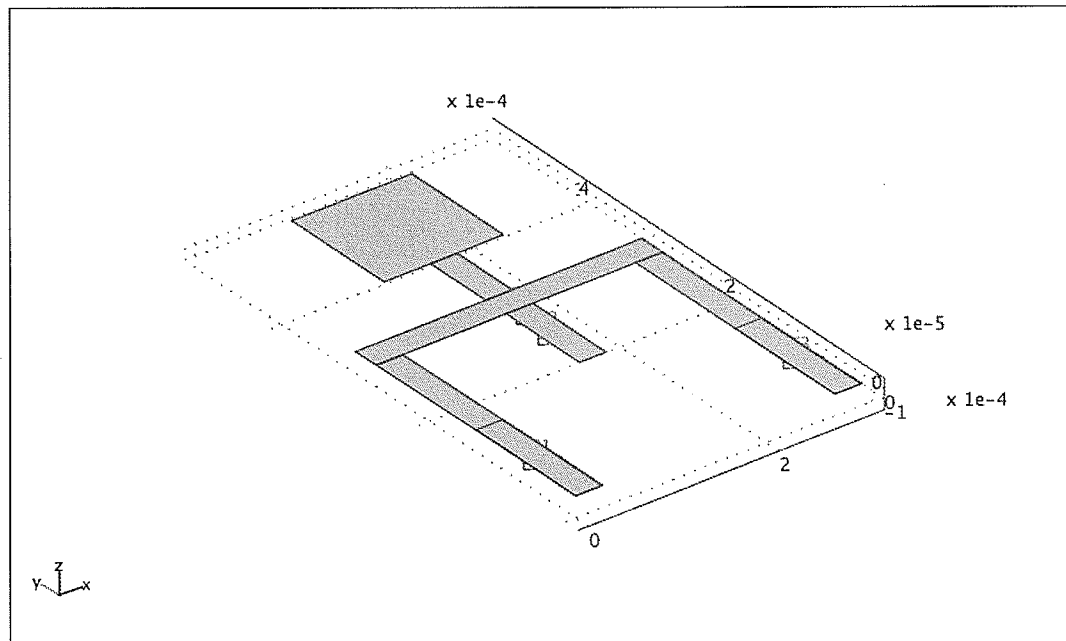
3. Constants

| Name | Expression | Value | Description |
|-----------|------------|-------|-------------|
| Stress | 4.5e8 | 4.5e8 | |
| F_Lorentz | 0 | 0 | |

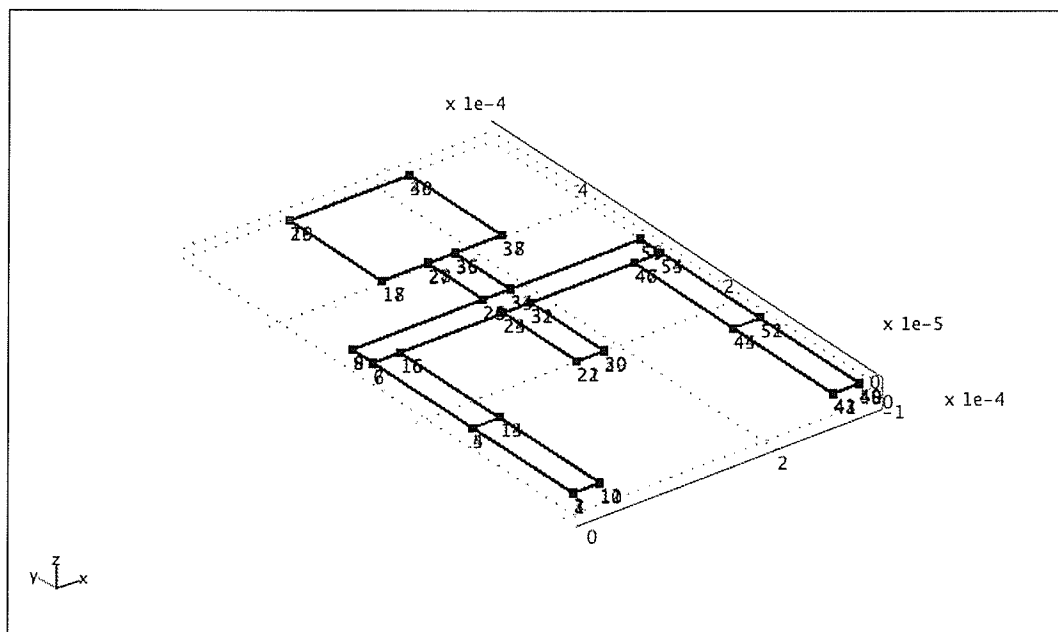
4. Geometry

Number of geometries: 2

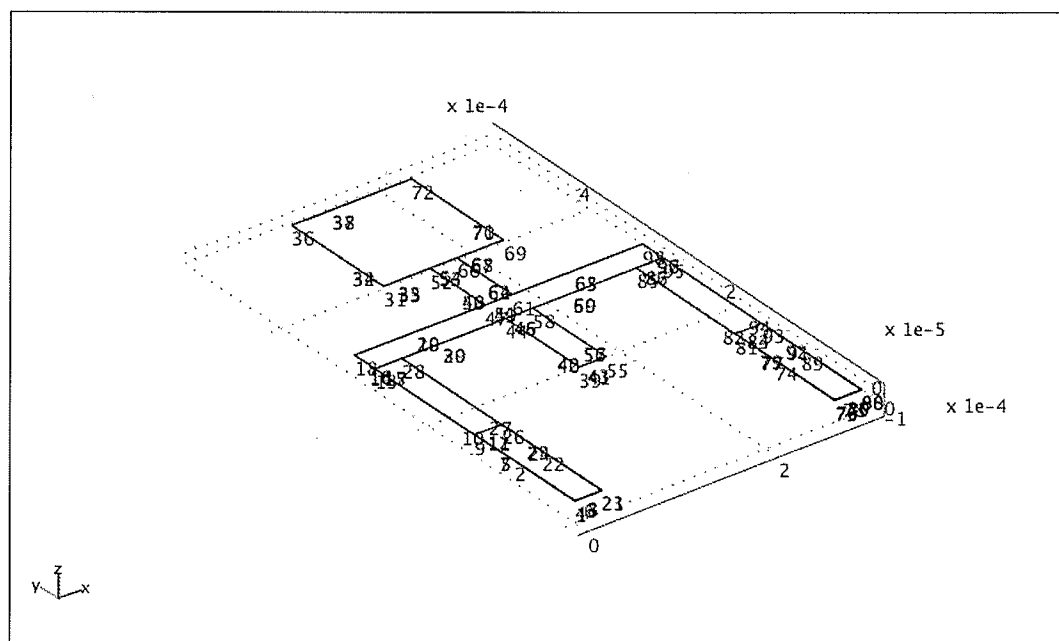
4.1. Geom1



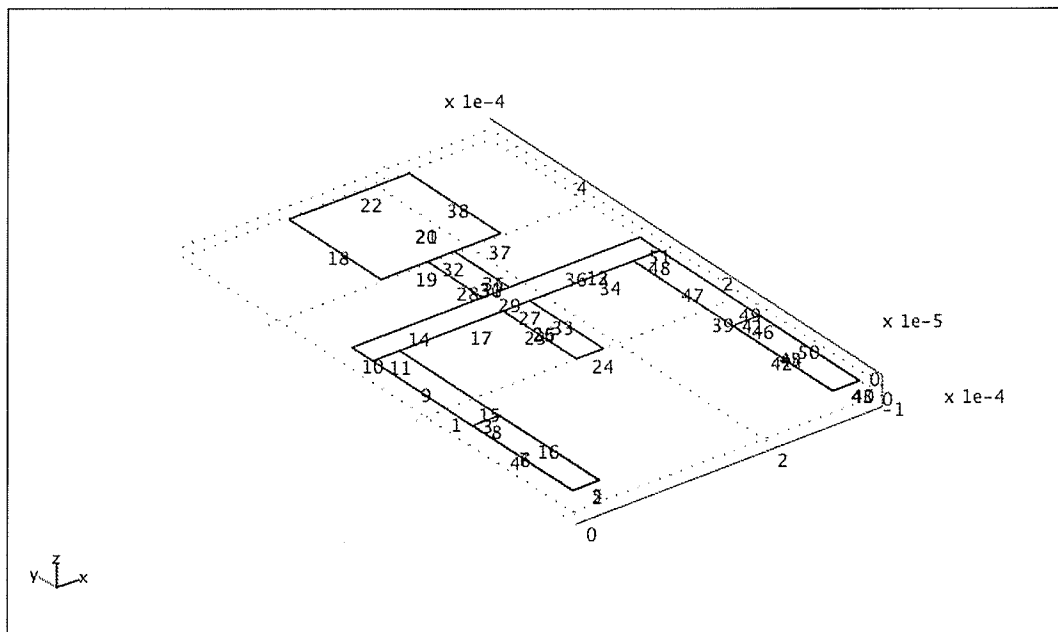
4.1.1. Point mode



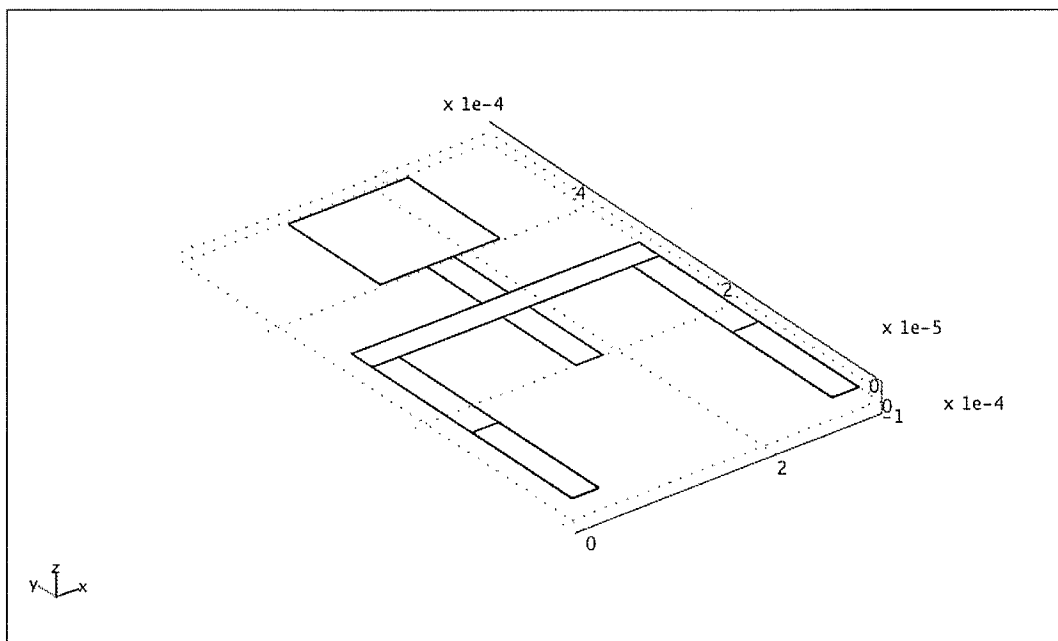
4.1.2. Edge mode



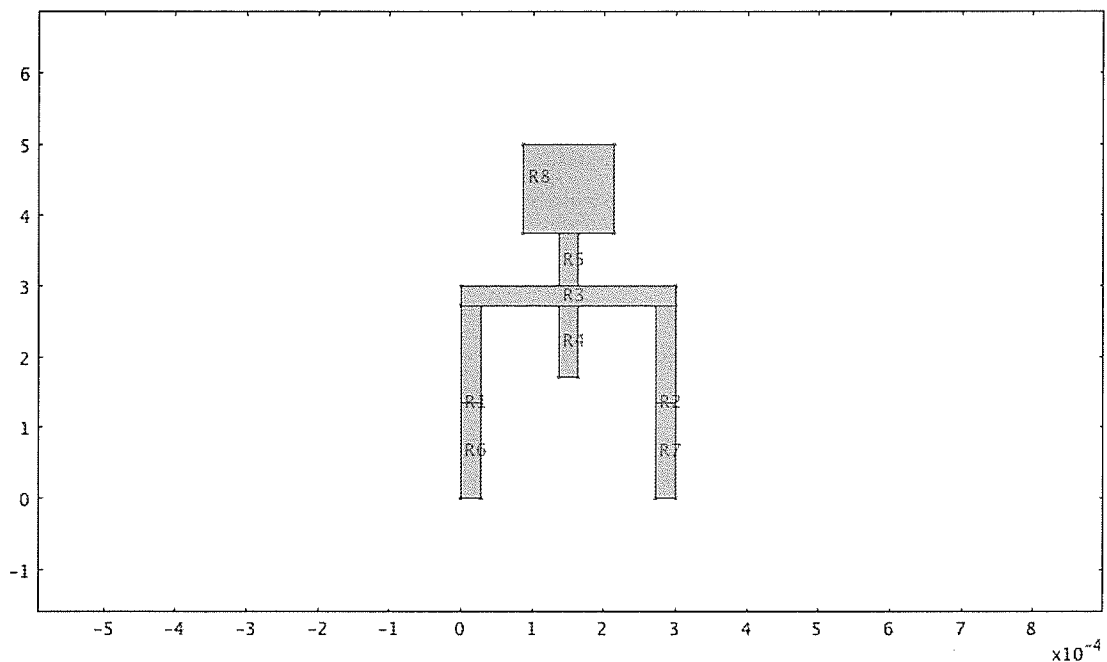
4.1.3. Boundary mode



4.1.4. Subdomain mode



4.2. Geom2



5. Geom1

Space dimensions: 3D

Independent variables: x, y, z

5.1. Mesh

5.1.1. Mesh Parameters

| Parameter | Value |
|-------------------------------------|-----------|
| Maximum element size | |
| Maximum element size scaling factor | 5 |
| Mesh curvature factor | 1 |
| Element growth rate | 2 |
| Mesh curvature cut off | 0.07 |
| Resolution of narrow regions | 0.1 |
| Resolution of geometry | 20 |
| x-direction scale factor | 1.0 |
| y-direction scale factor | 1.0 |
| z-direction scale factor | 2 |
| Optimize quality | On |
| Mesh geometry to level | Subdomain |
| Subdomain | 1-8 |

5.2. Application Mode: Solid, Stress-Strain (smsld)

Application mode type: Solid, Stress-Strain (MEMS Module)

Application mode name: smsld

5.2.1. Application Mode Properties

| Property | Value |
|---------------------------|---------------------------|
| Default element type | Lagrange - Quadratic |
| Analysis type | Parametric |
| Large deformation | On |
| Implementation | Principle of virtual work |
| Specify eigenvalues using | Eigenfrequency |
| Frame | Frame (xyz) |
| Weak constraints | Off |

5.2.2. Variables

Dependent variables: u, v, w, p

Shape functions: shlag(2,'u'), shlag(2,'v'), shlag(2,'w')

Interior boundaries not active

5.2.3. Boundary Settings

| | | | |
|------------------------------------|------------------|--|----------------|
| Boundary | | 1, 3-5, 7-10, 12, 14-26, 28, 30-31, 33-39, 41-43, 45-47, 49-51 | 13 |
| Face load (force/area) z-dir. (Fz) | N/m ² | 0 | - F_Lorentz |
| Hx | 1 | 0 | 0 |
| Hy | 1 | 0 | 0 |
| Hz | 1 | 0 | 0 |
| Boundary | | 2, 40 | |
| Face load (force/area) z-dir. (Fz) | | 0 | |
| Hx | | 1 | |
| Hy | | 1 | |
| Hz | | 1 | |

5.2.4. Subdomain Settings

| | | | |
|----------------------------------|-------------------|------------------------------------|---------------------|
| Subdomain | | 1, 3-4 | 2, 8 |
| Young's modulus (E) | Pa | 69e9 (Aluminum 3003-H18) | 279e9 (Cr) |
| Density (rho) | kg/m ³ | 2730 (Aluminum 3003-H18) | 7150 (Cr) |
| ini_stress | Pa | 0 | 1 |
| Thermal expansion coeff. (alpha) | 1/K | 23.2e-6 (Aluminum 3003-H18) | 4.90e-6 (Cr) |
| Poisson's ratio (nu) | 1 | 0.33 (Aluminum 3003-H18) | 0.21 (Cr) |
| Initial normal stress sx (sxi) | Pa | 0 | +Stress |
| Initial normal stress sy (syi) | Pa | 0 | +Stress |
| Subdomain | | 5-7 | |
| Young's modulus (E) | | 69e9 (Aluminum 3003-H18) | |
| Density (rho) | | 2730 (Aluminum 3003-H18) | |
| ini_stress | | 0 | |
| Thermal expansion coeff. (alpha) | | 23.2e-6 (Aluminum 3003-H18) | |
| Poisson's ratio (nu) | | 0.33 (Aluminum 3003-H18) | |
| Initial normal stress sx (sxi) | | 1e3 | |
| Initial normal stress sy (syi) | | 1e3 | |

6. Geom2

Space dimensions: 2D

Independent variables: x, y, z

7. Materials/Coefficients Library

7.1. Aluminum 3003-H18

| Parameter | Value |
|---|---------|
| Heat capacity (C) | 893 |
| Young's modulus (E) | 69e9 |
| Thermal expansion coeff. (alpha) | 23.2e-6 |
| Relative permittivity (epsilon _r) | 1 |
| Thermal conductivity (k) | 155 |
| Relative permeability (mu _r) | 1 |
| Poisson's ratio (nu) | 0.33 |
| Density (rho) | 2730 |
| Electrical conductivity (sigma) | 2.326e7 |

7.2. Cr

| Parameter | Value |
|----------------------------------|---------|
| Heat capacity (C) | 45 |
| Young's modulus (E) | 279e9 |
| Thermal expansion coeff. (alpha) | 4.90e-6 |
| Thermal conductivity (k) | 93.7 |
| Poisson's ratio (nu) | 0.21 |
| Density (rho) | 7150 |
| Electrical conductivity (sigma) | 7.9e6 |

8. Solver Settings

Solve using a script: off

| | |
|--------------------|----------------------|
| Analysis type | Parametric |
| Auto select solver | On |
| Solver | Parametric nonlinear |
| Solution form | Automatic |
| Symmetric | On |
| Adaption | Off |

8.1. Direct (SPOOLES)

Solver type: Linear system solver

| Parameter | Value |
|-----------------------|----------------|
| Pivot threshold | 0.1 |
| Preordering algorithm | Minimum degree |

8.2. Nonlinear

| Parameter | Value |
|-------------------------------------|--------|
| Relative tolerance | 1.0E-6 |
| Maximum number of iterations | 25 |
| Manual tuning of damping parameters | Off |
| Highly nonlinear problem | Off |
| Initial damping factor | 1.0 |
| Minimum damping factor | 1.0E-4 |
| Restriction for step size update | 10.0 |

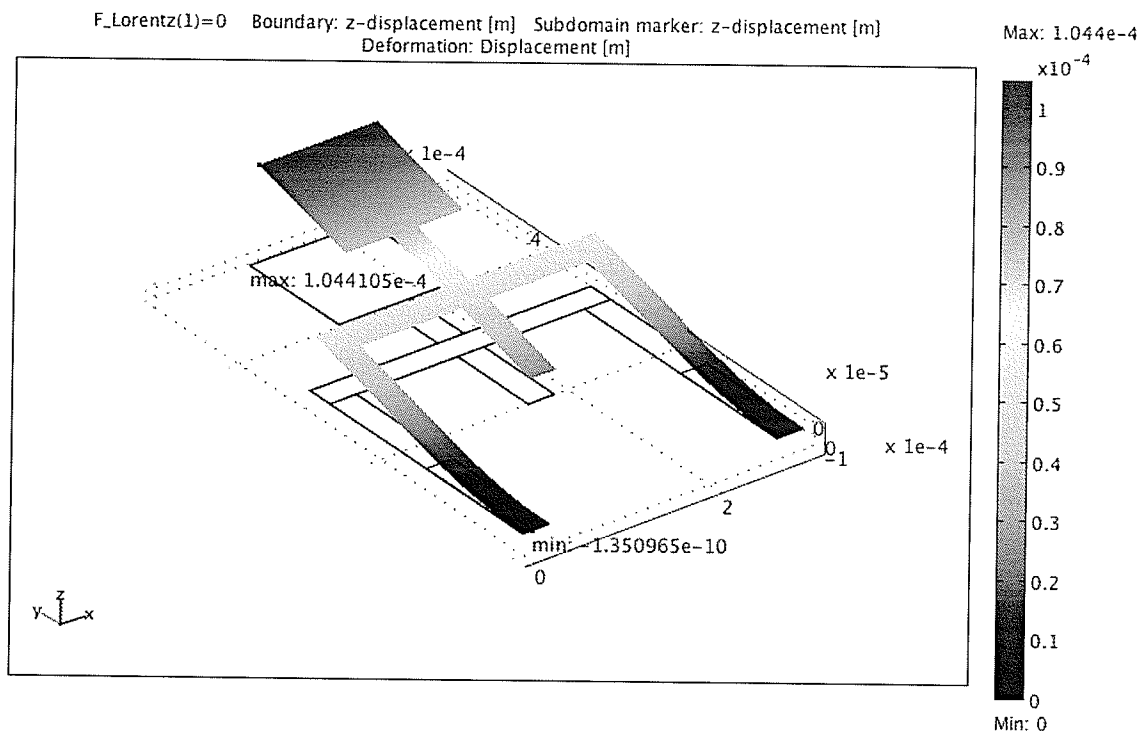
8.3. Parametric

| Parameter | Value |
|--------------------------------------|-----------|
| Name of parameter | F_Lorentz |
| List of parameter values | 0:5:190 |
| Predictor | Linear |
| Manual tuning of parameter step size | Off |
| Initial step size | 0.0 |
| Minimum step size | 0.0 |
| Maximum step size | 0.0 |

8.4. Advanced

| Parameter | Value |
|--|-------------|
| Constraint handling method | Elimination |
| Null-space function | Automatic |
| Assembly block size | 5000 |
| Use Hermitian transpose of constraint matrix | Off |
| Use complex functions with real input | Off |
| Stop if error due to undefined operation | On |
| Type of scaling | Automatic |
| Manual scaling | |
| Row equilibration | On |
| Manual control of reassembly | Off |
| Load constant | On |
| Constraint constant | On |
| Mass constant | On |
| Damping (mass) constant | On |
| Jacobian constant | On |
| Constraint Jacobian constant | On |

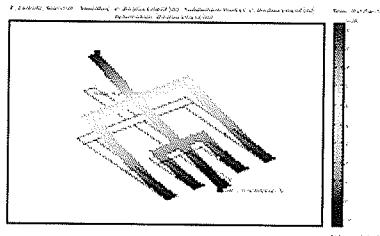
9. Postprocessing



This post processing snapshot shows the device at rest (no actuation applied) with 0.45 GPa of residue stress in the tensile Cr. The color legend shows the height of the device, with a maximum height of 104 μm at the tip.



Appendix B2: COMSOL Model Report – Rotationally Corrected Design



1. Table of Contents

- Title - COMSOL Model Report
- Table of Contents
- Model Properties
- Constants
- Geometry
- Geom1
- Geom2
- Materials/Coefficients Library
- Solver Settings
- Postprocessing
- Variables

2. Model Properties

| Property | Value |
|----------------|---------------------------------|
| Model name | D7_B2 |
| Author | Kwan-yu Lai |
| Company | University of Manitoba |
| Department | Electrical/Computer Engineering |
| Reference | |
| URL | |
| Saved date | Dec 9, 2005 9:43:42 AM |
| Creation date | Dec 1, 2005 10:02:04 AM |
| COMSOL version | COMSOL 3.2.0.300 |

File name: /Users/student/Desktop/D7_B2 0-90Nm2.mph

Application modes and modules used in this model:

- Geom1 (3D)
 - Solid, Stress-Strain (MEMS Module)
- Geom2 (2D)

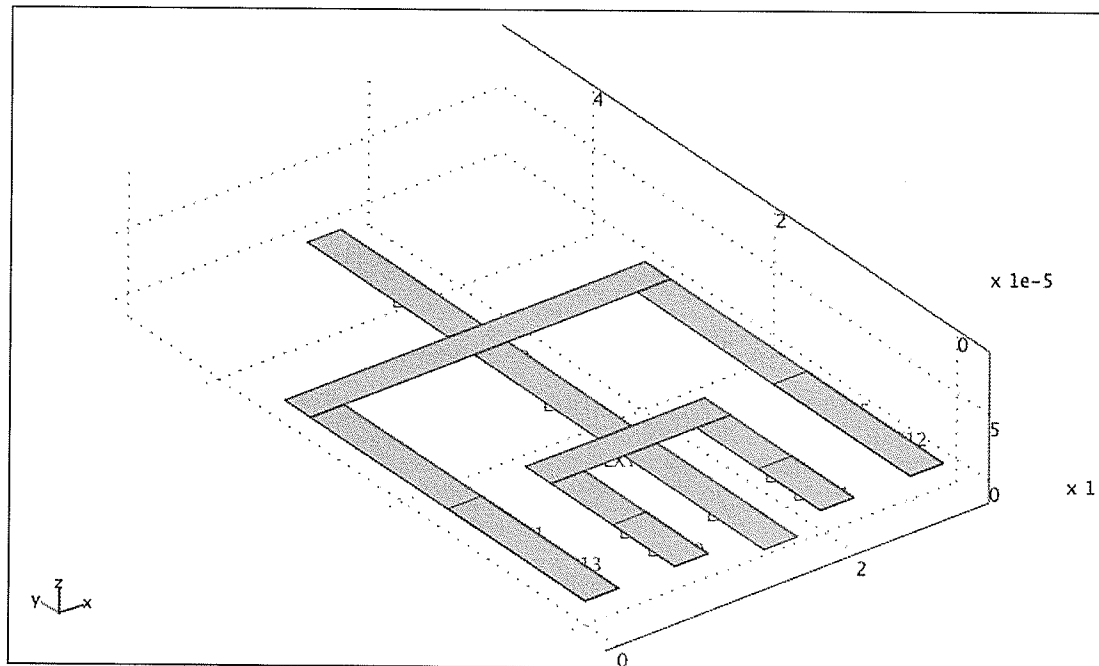
3. Constants

| Name | Expression | Value | Description |
|---------------|------------|-------|-------------|
| Stress | 4.5e8 | 4.5e8 | |
| F_Lorentz_top | 0 | 0 | |
| F_Lorentz_bot | 0 | 0 | |

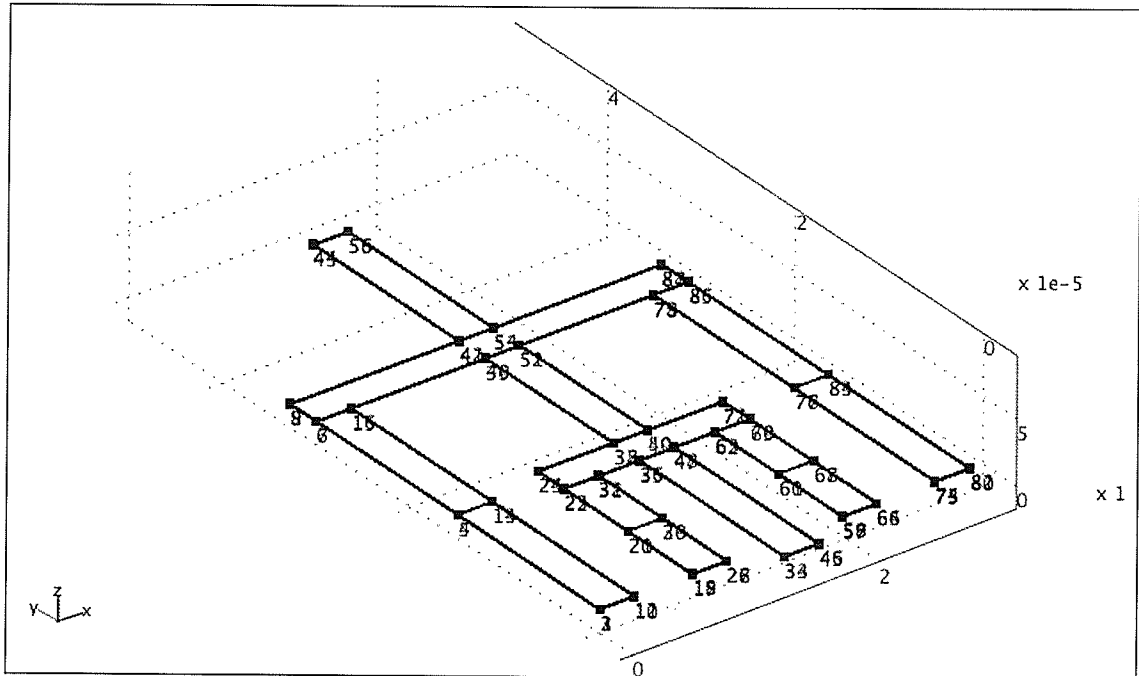
4. Geometry

Number of geometries: 2

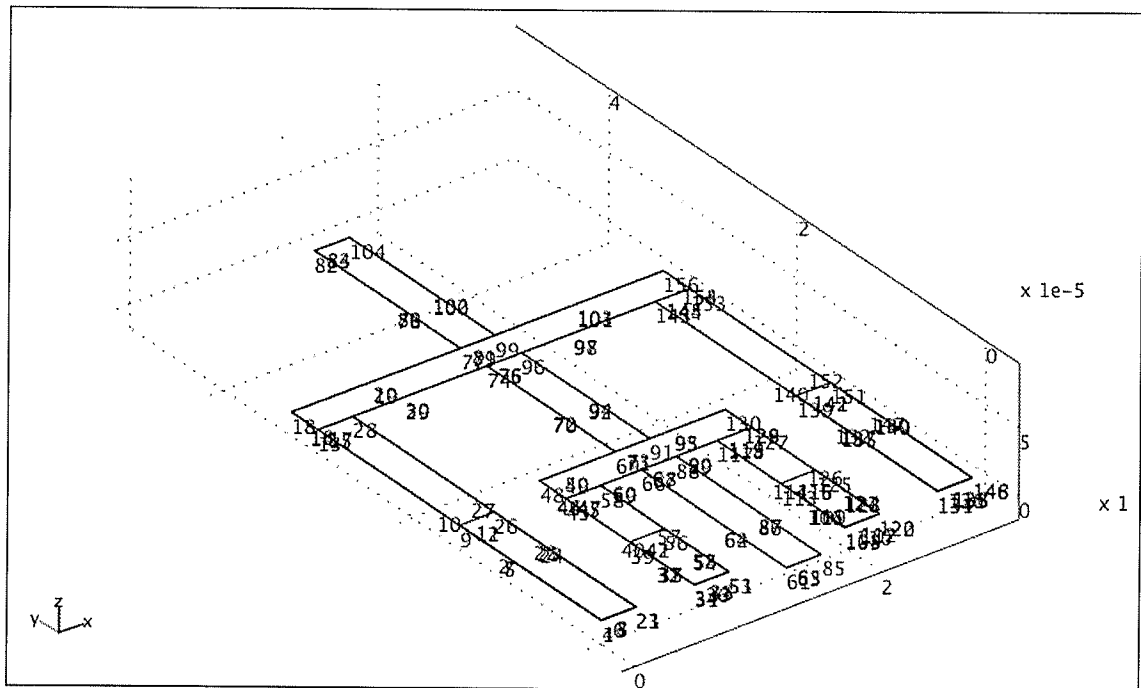
4.1. Geom1



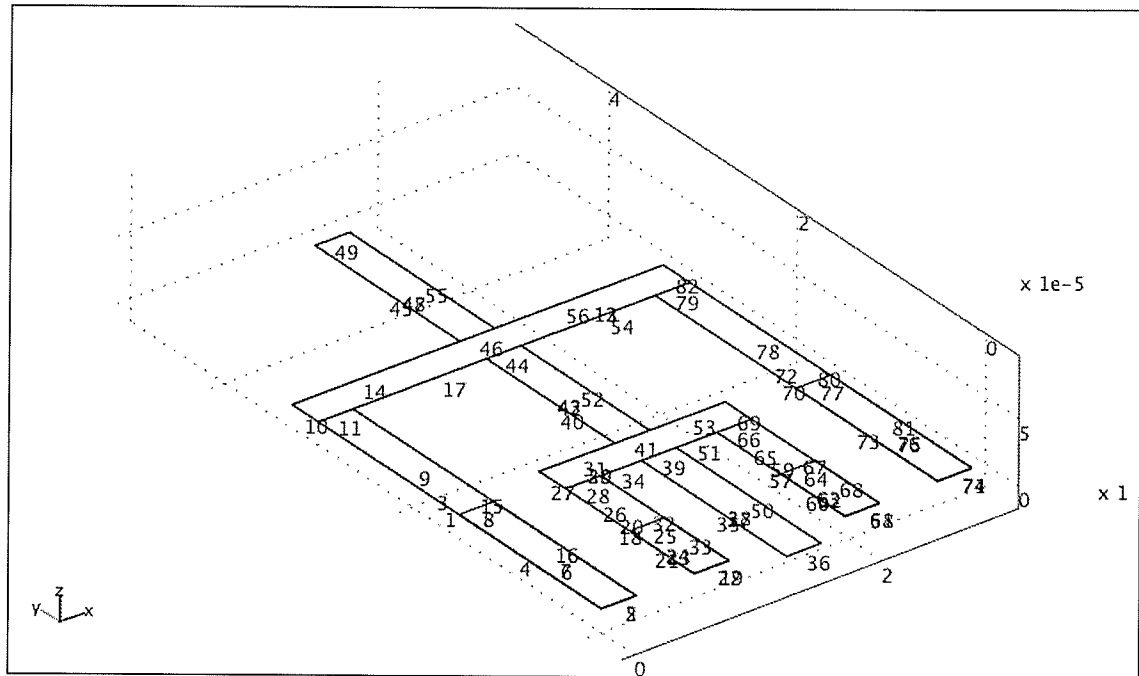
4.1.1. Point mode



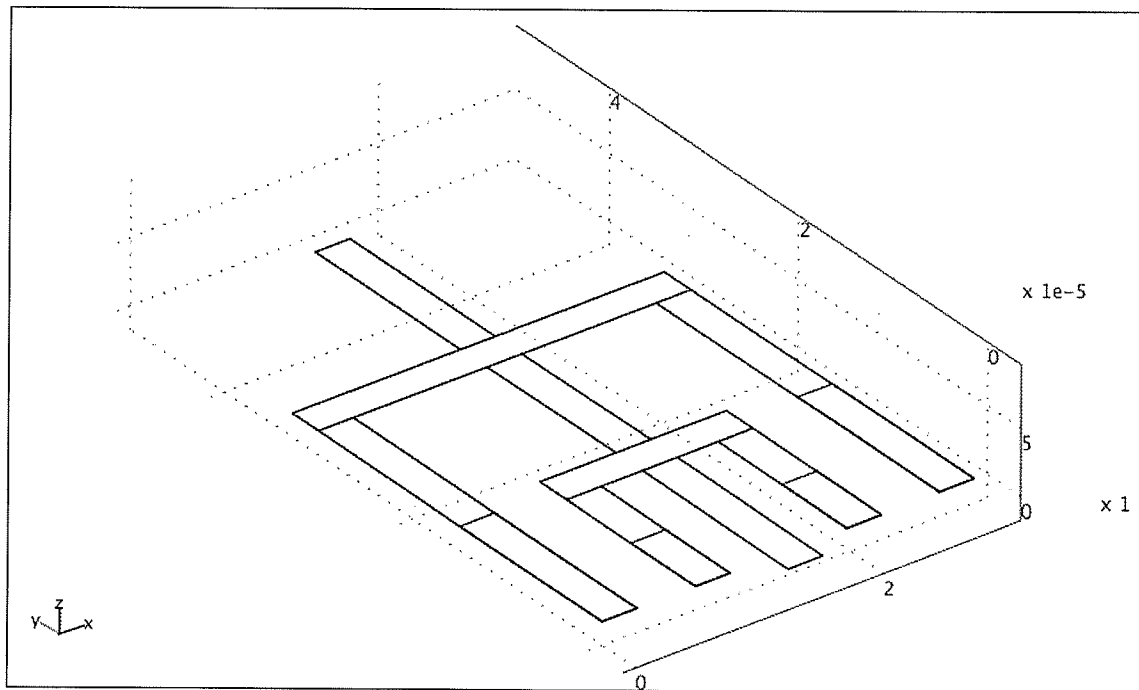
4.1.2. Edge mode



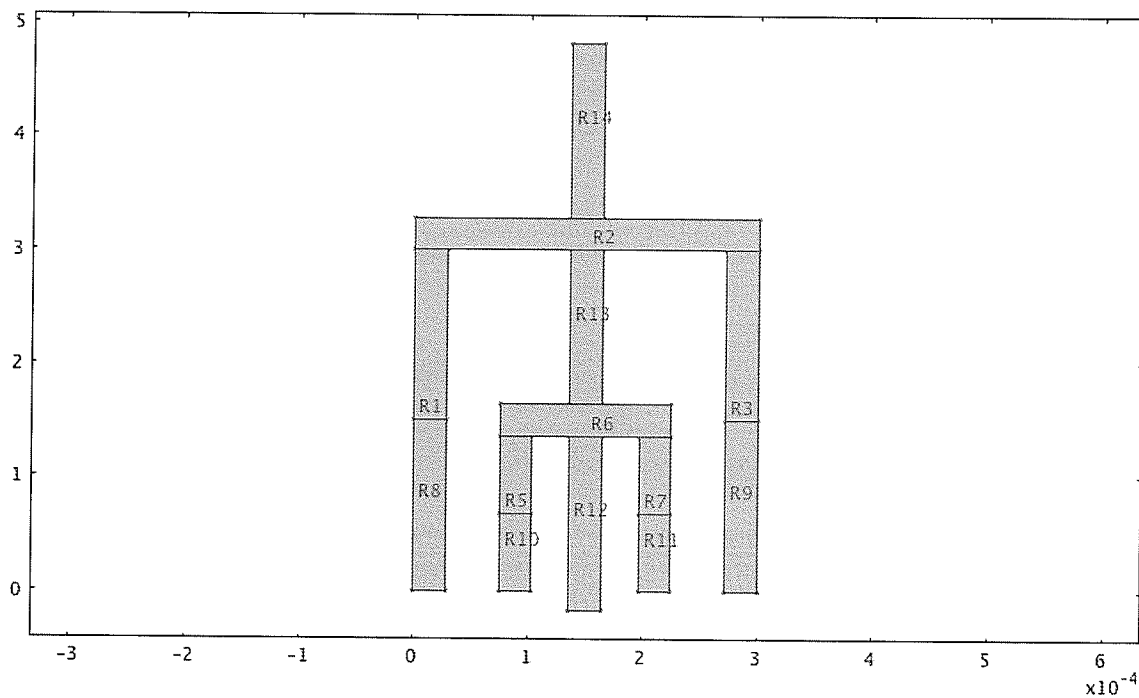
4.1.3. Boundary mode



4.1.4. Subdomain mode



4.2. Geom2



5. Geom1

Space dimensions: 3D

Independent variables: x, y, z

5.1. Mesh

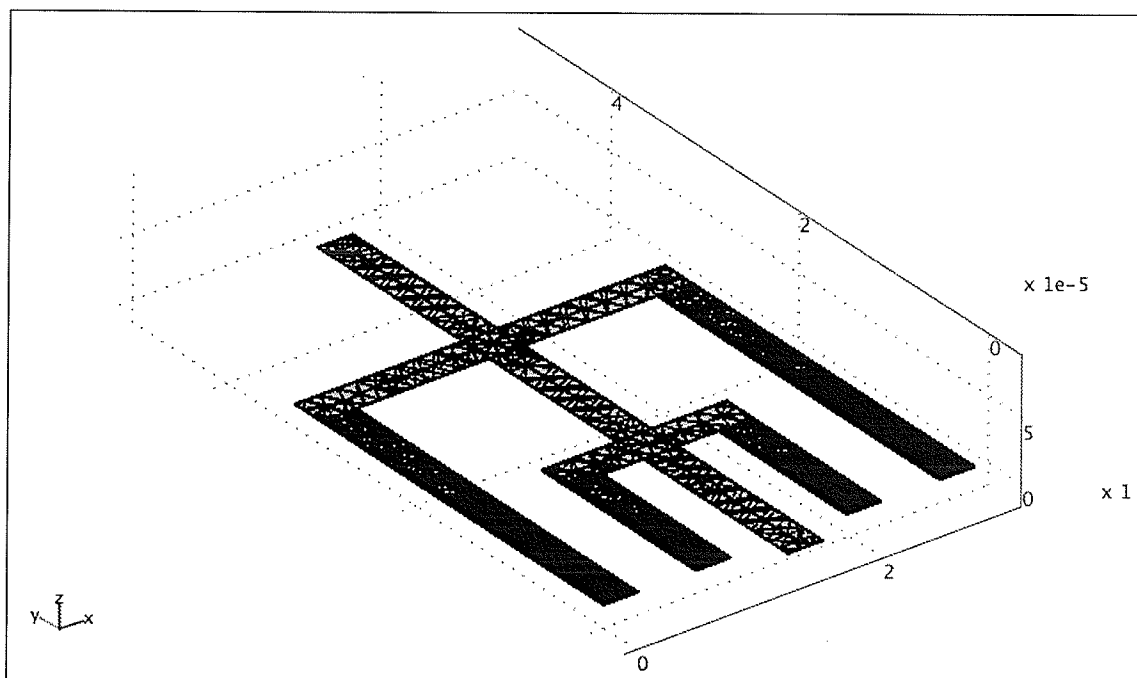
5.1.1. Mesh Parameters

| Parameter | Value |
|-------------------------------------|-----------|
| Maximum element size | |
| Maximum element size scaling factor | 5 |
| Mesh curvature factor | 1 |
| Element growth rate | 2 |
| Mesh curvature cut off | 0.07 |
| Resolution of narrow regions | 0.1 |
| Resolution of geometry | 20 |
| x-direction scale factor | 1.0 |
| y-direction scale factor | 1.0 |
| z-direction scale factor | 2.0 |
| Optimize quality | On |
| Mesh geometry to level | Subdomain |

| | |
|------------------------|-------|
| Subdomain | 1-13 |
| Maximum element size | |
| Element growth rate | |
| Boundary | 1-82 |
| Maximum element size | |
| Element growth rate | |
| Mesh curvature factor | |
| Mesh curvature cut off | |
| Edge | 1-156 |
| Maximum element size | |
| Element growth rate | |
| Mesh curvature factor | |
| Mesh curvature cut off | |
| Point | 1-88 |
| Maximum element size | |
| Element growth rate | |

5.1.2. Mesh Statistics

| | |
|------------------------------|--------|
| Number of degrees of freedom | 156861 |
| Number of edge elements | 1804 |
| Number of boundary elements | 16729 |
| Number of elements | 30379 |
| Minimum element quality | 0.0316 |



5.2. Application Mode: Solid, Stress-Strain (smsld)

Application mode type: Solid, Stress-Strain (MEMS Module)

Application mode name: smsld

5.2.1. Application Mode Properties

| Property | Value |
|---------------------------|---------------------------|
| Default element type | Lagrange - Quadratic |
| Analysis type | Parametric |
| Large deformation | On |
| Implementation | Principle of virtual work |
| Specify eigenvalues using | Eigenfrequency |
| Frame | Frame (xyz) |
| Weak constraints | Off |

5.2.2. Variables

Dependent variables: u, v, w, p

Shape functions: shlag(2,'u'), shlag(2,'v'), shlag(2,'w')

Interior boundaries not active

5.2.3. Boundary Settings

| | | | |
|------------------------------------|------------------|--|-----------------------|
| Boundary | | 1, 3-5, 7-10, 12, 14-18, 20-22, 24-27, 29, 31-38, 40, 42-43, 45, 47-57, 59-61, 63-65, 67-70, 72-74, 76-78, 80-82 | 2, 19, 58, 71 |
| Face load (force/area) z-dir. (Fz) | N/m ² | 0 | 0 |
| Hx | 1 | 0 | 1 |
| Hy | 1 | 0 | 1 |
| Hz | 1 | 0 | 1 |
| Boundary | | 13 | 30 |
| Face load (force/area) z-dir. (Fz) | | -F_Lorentz_top | -F_Lorentz_bot |
| Hx | | 0 | 0 |
| Hy | | 0 | 0 |
| Hz | | 0 | 0 |

5.2.4. Subdomain Settings

| | | | |
|----------------------------------|-------------------|------------------------------------|---------------------|
| Subdomain | | 1, 3-4, 6-10, 12 | 2, 5, 11, 13 |
| Young's modulus (E) | Pa | 69e9 (Aluminum 3003-H18) | 279e9 (Cr) |
| Density (rho) | kg/m ³ | 2730 (Aluminum 3003-H18) | 7150 (Cr) |
| ini_stress | Pa | 0 | 1 |
| Thermal expansion coeff. (alpha) | 1/K | 23.2e-6 (Aluminum 3003-H18) | 4.90e-6 (Cr) |
| Poisson's ratio (nu) | 1 | 0.33 (Aluminum 3003-H18) | 0.21 (Cr) |
| Initial normal stress sx (sxi) | Pa | 0 | +Stress |
| Initial normal stress sy (syi) | Pa | 0 | +Stress |

6. Geom2

Space dimensions: 2D

Independent variables: x, y, z

7. Materials/Coefficients Library

7.1. Cr

| Parameter | Value |
|-------------------|-------|
| Heat capacity (C) | 45 |

| | |
|----------------------------------|---------|
| Young's modulus (E) | 279e9 |
| Thermal expansion coeff. (alpha) | 4.90e-6 |
| Thermal conductivity (k) | 93.7 |
| Poisson's ratio (nu) | 0.21 |
| Density (rho) | 7150 |
| Electrical conductivity (sigma) | 7.9e6 |

7.2. Aluminum 3003-H18

| Parameter | Value |
|---|---------|
| Heat capacity (C) | 893 |
| Young's modulus (E) | 69e9 |
| Thermal expansion coeff. (alpha) | 23.2e-6 |
| Relative permittivity (epsilon _r) | 1 |
| Thermal conductivity (k) | 155 |
| Relative permeability (mu _r) | 1 |
| Poisson's ratio (nu) | 0.33 |
| Density (rho) | 2730 |
| Electrical conductivity (sigma) | 2.326e7 |

8. Solver Settings

Solve using a script: off

| | |
|--------------------|----------------------|
| Analysis type | Parametric |
| Auto select solver | On |
| Solver | Parametric nonlinear |
| Solution form | Automatic |
| Symmetric | On |
| Adaption | Off |

8.1. Direct (SPOOLES)

Solver type: Linear system solver

| Parameter | Value |
|-----------------------|----------------|
| Pivot threshold | 0.1 |
| Preordering algorithm | Minimum degree |

8.2. Nonlinear

| Parameter | Value |
|-------------------------------------|--------|
| Relative tolerance | 1.0E-6 |
| Maximum number of iterations | 25 |
| Manual tuning of damping parameters | Off |
| Highly nonlinear problem | Off |
| Initial damping factor | 1.0 |
| Minimum damping factor | 1.0E-4 |
| Restriction for step size update | 10.0 |

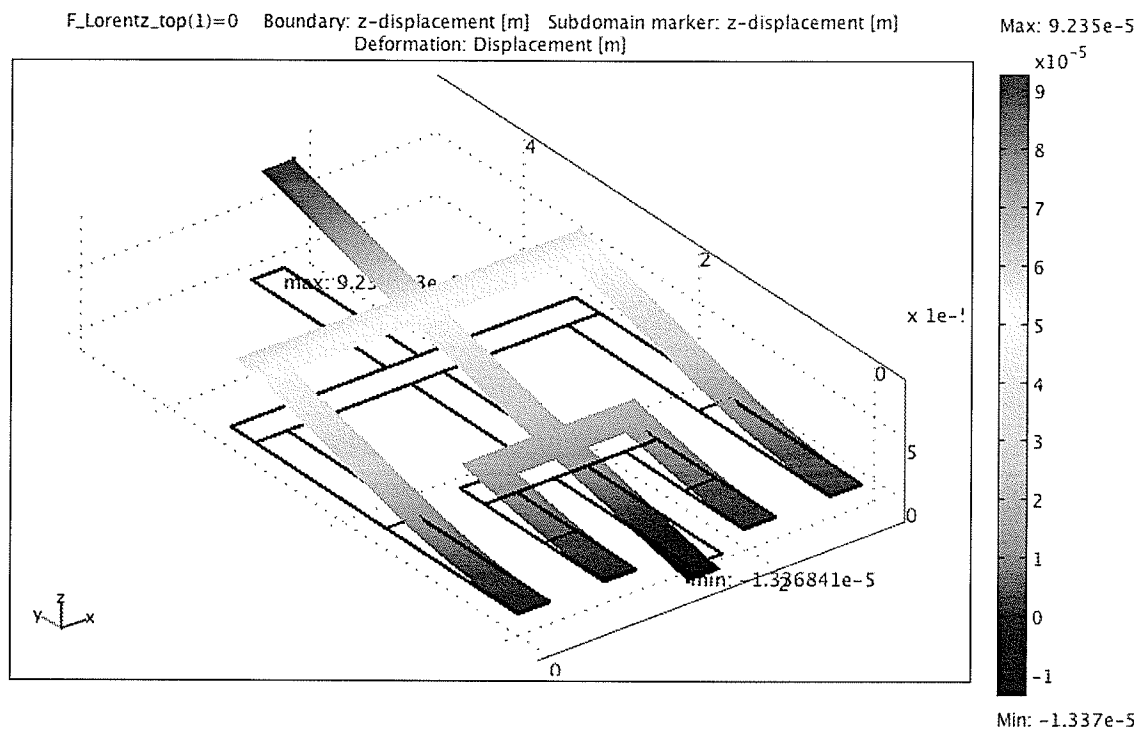
8.3. Parametric

| Parameter | Value |
|--------------------------------------|---------------|
| Name of parameter | F_Lorentz_top |
| List of parameter values | 90:5:300 |
| Predictor | Linear |
| Manual tuning of parameter step size | Off |
| Initial step size | 0.0 |
| Minimum step size | 0.0 |
| Maximum step size | 0.0 |

8.4. Advanced

| Parameter | Value |
|--|-------------|
| Constraint handling method | Elimination |
| Null-space function | Automatic |
| Assembly block size | 5000 |
| Use Hermitian transpose of constraint matrix | Off |
| Use complex functions with real input | Off |
| Stop if error due to undefined operation | On |
| Type of scaling | Automatic |
| Manual scaling | |
| Row equilibration | On |
| Manual control of reassembly | Off |
| Load constant | On |
| Constraint constant | On |
| Mass constant | On |
| Damping (mass) constant | On |
| Jacobian constant | On |
| Constraint Jacobian constant | On |

9. Postprocessing



Appendix C: Matlab Code for Radius of Curvature Calculation in a Bimorph Cantilever

```

%-----
% Kwan-yu Lai 6743856
% Graduate Student
% Department of Electrical and Computer Engineering
% University of Manitoba
%-----
% Program which calculates the radius of curvature expected
% on a Al-Cr cantilever
% Factors considered include thicknesses, residual stress
% 2 papers referred: Judy et al and Yasuda et al
%-----

close all
clear all

E_cr = 279e9; % chrome Young's Modulus 289 GPa, from a cornell univ
site
E_al = 69e9; % aluminum Young's Modulus 69 GPa, from a cornell univ
site

t_cr = 100e-9; % 100 nm chrome thickness
t_al = 0.7e-6; % 0.7 um aluminum thickness

%RSF = 4e9; % a residue stress factor in the films that is assumed to
be 0.3 GPa by yasuda et al.
% a value of 3e9 fits D6W1 data -> bad fabrication
% a value of 3e8~4.5e8 fits D7W1 data -> measured R =
7.5e-4 m

sigma_cr = -4.5e8; % residue film stress of Cr
sigma_al = 0; % residue film stress of Al

% ----- single point calculations and verification -----

m = E_cr / E_al;
n = t_cr / t_al;
f = (1 + 7*m*n + 12*m*n^2 + 7*m*n^3 + m^2*n^4) / (n*(1+n));
RSF = -m*sigma_al - sigma_cr;
radius = E_al * t_al * f / (6 * RSF)

m_judy = 1/m;
n_judy = 1/n;
K = 1 + 4*m_judy*n_judy + 6*m_judy*n_judy^2 + 4*m_judy*n_judy^3 +
m_judy^2*n_judy^4;

radius_judy = -(t_cr+t_al)*E_cr*(3*m_judy +
K/(n_judy*(1+n_judy)^2))/(6*(m_judy*sigma_cr + sigma_al))

% -----
% calculating a plot

```

```
t_crArray = 1e-9:1e-9:200e-9;
%t_crArray = ones(1, 200) * t_cr;
%t_alArray = 40e-9:40e-9:8e-6;

nArray = t_crArray./t_al;
% nArray = 1e-3:1e-3:0.4;
% t_alArray = t_cr./nArray;
%
fArray = (1 + 7*m*nArray + 12*m*nArray.^2 + 7*m*nArray.^3 +
m^2*nArray.^4) ./ (nArray.*(1.+nArray));
radiusArray = E_al * t_al .* fArray ./ (6 * RSF);

figure
plot(nArray, radiusArray)
%axis([ 0 0.4 0 2e-3])
title('Radius of Curvature vs Cr/Al Thickness Ratio')
xlabel('ratio Cr/Al')
ylabel('radius (m)')
```

Appendix D: Heat Analysis of the Basic Actuators

The heat generated by the basic actuators via joule heating effects is the limiting factor for the maximum allowed current through the device. Thus it is an interesting study to show the effects of heat generated by the device during actuation. This study was done using the same COMSOL Multiphysics FEM software under the Conductive Media DC (emdc) and Heat Transfer by Conduction (ht) physic packages. The geometry and material setup for the model is identical to that of Chapter 4.

The model was first solved under the emdc physics mode. The boundary conditions for this mode are such that the base of one of the arms is exerting an even inward current flow of 20mA (the amount required for full actuation), and the other base of the arm is electrically grounded. The boundary condition everywhere else is electrical insulation. The main results of this simulation are the electrical potential and the joule heating generated by the actuation, and are plotted in the following figure. These figures show that the electrical voltage distribution is properly behaved, and that the joule heating is evenly distributed throughout the structure except at the joints. Note that the joule heating is given in W/m^3 .

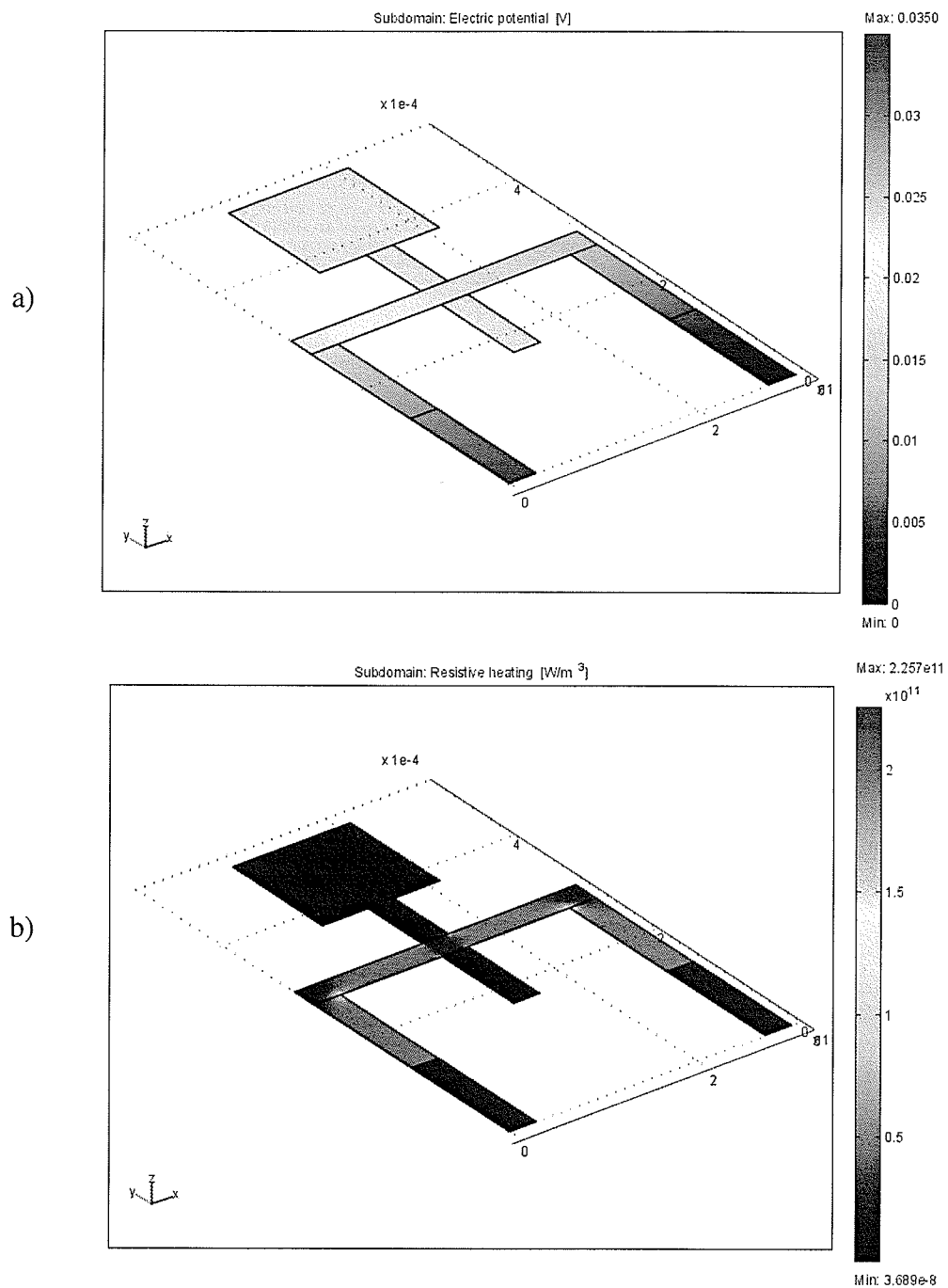


Figure 1: a) Electrical potential as a result of applying 20mA through the device in Volts. b) Joule heating generated by the current in W/m³.

Using the joule heating data in the above model, the conductive heat transfer model can calculate the actual temperature throughout the device given temperature boundary conditions. The boundary conditions are setup such that the base of the arms in contact with the substrate are fixed at 300°K, and the rest of the device is surrounded by air (heat transfer coefficient = 5) also at 300°K. From this result, it shows that the device temperature at 20mA actuation is about 322°K at the middle of the crossbar, which is well below the melting point of any of the materials.

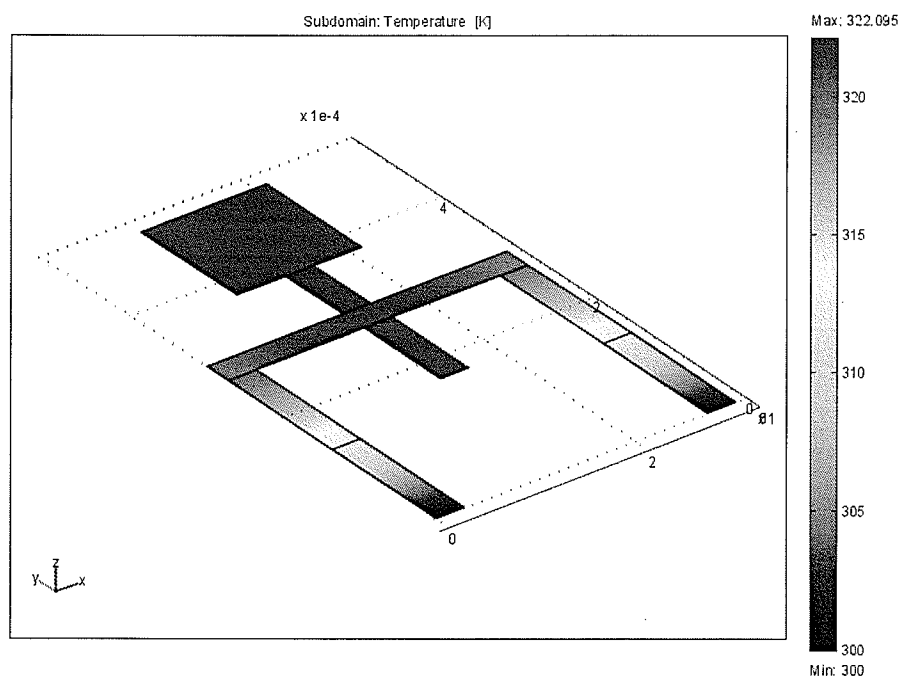


Figure 2: Temperature of the basic actuator under 20mA actuation.

An informative extension to the above study is to find the maximum temperature for a given drive current. This is summarized in the following table and figure. Note that the maximum temperature for current = 110mA has exceeded the melting temperature of aluminum and implies that the device would break down at such electrical stresses.

Table I: Maximum temperature in the device vs actuation current

| Actuation Current (mA) | Maximum Temperature (°K) |
|------------------------|--------------------------|
| 20 | 322 |
| 50 | 438 |
| 80 | 653 |
| 110 | 968 |

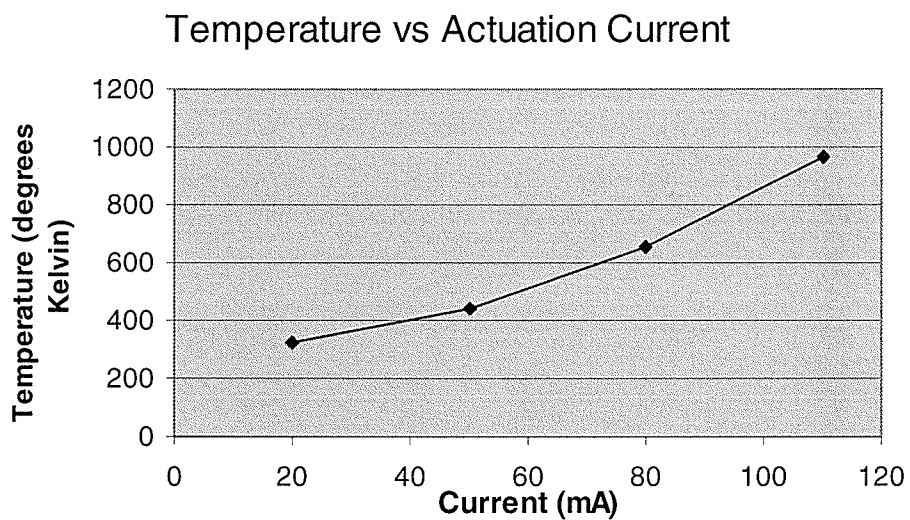


Figure 3: Plot of maximum temperature in the device vs actuation current